

Dissertation
submitted to the
Combined Faculties for the Natural Sciences and for Mathematics
of the Ruperto-Carola University of Heidelberg, Germany
for the degree of
Doctor of Natural Sciences

Put forward by
Diplom-Physiker Jens Stefan Buchner
Born in Backnang
Oral examination: 23.11.2012

Constructive Inversion of Vadose Zone GPR Observations

Referees:

Prof. Dr. Kurt Roth

Prof. Dr. Peter Bastian

Konstruktive Inversion von GPR Beobachtungen der vadosen Zone Um die Dynamik des Erdsystems vorherzusagen, sind Beobachtungen von Struktur und Wassergehalt der vadosen Zone von großem Interesse. Ein dafür geeignetes Messinstrument ist Ground Penetrating Radar (GPR). In dieser Dissertation wird die konstruktive Inversion von Oberflächen-GPR-Daten vorgestellt. Sie basiert auf einem parametrisierten Modell von Struktur und Verteilung der dielektrischen Permittivität des Untergrunds. Unter Verwendung des Modells werden GPR-Messungen durch die numerische Lösung der Maxwell-Gleichungen simuliert. Nach der Detektion von Signalen in den gemessenen und simulierten Daten, wird das Residuum der Signallaufzeit und -amplitude iterativ minimiert, um die Parameter des Untergrundmodells zu schätzen. Anschließend wird der Wassergehalt aus der dielektrischen Permittivität berechnet. Die Methode wurde auf Messungen eines Testvolumens mit bekannter Struktur und Wassergehalt angewendet. Ein Vergleich mit den Schätzungen zeigte eine Übereinstimmung der Struktur von innerhalb ± 5 cm und für den Wassergehalt eine Abweichung von weniger als 2 % vol. Die weitere Auswertung von Felddaten zeigte die Anwendbarkeit der Methode, wenn die Struktur und die Permittivität durch Splines dargestellt werden. Weiterhin wurde eine Zeitreihe unter der Annahme einer konstanten Struktur ausgewertet, was eine Interpretation der Wasserdynamik ermöglichte. Neben der Bereitstellung genauer Informationen über die Wassergehaltsverteilung und Struktur des Untergrunds, gestattet die Methode den zukünftigen Versuch der Schätzung von hydraulischen Parametern.

Constructive Inversion of Vadose Zone GPR Observations To predict the of Earth system dynamics, observations of the vadose zone structure and water content are of vital interest. A suited measurement technique is ground penetrating radar (GPR). In this dissertation, the constructive inversion of surface GPR data is introduced. It relies on a parameterized model of the subsurface structure and distribution of dielectric permittivity. With it, GPR measurements are simulated by numerically solving Maxwell's equations. After detecting signals in the measured and simulated data, the residuals of the signals' traveltime and amplitude is iteratively minimized to estimate the subsurface parameters. Then, water content is computed from dielectric permittivity. The method was applied to measurements obtained on a testbed, providing ground-truth data. A comparison with the estimation results showed an agreement for the structure within ± 5 cm and for the water content, a difference less than 2 % vol. A further evaluation of field data demonstrated the method's applicability, when representing structure and permittivity by spline functions. Additionally a time-series was evaluated with assuming a constant structure, which enabled to interpret water dynamics. Besides providing accurate information on water content distribution and subsurface structure, the method allows the future attempt to estimate hydraulic properties.

Contents

1	Introduction	13
2	Environmental Context	17
2.1	The Earth System	17
2.2	Soil Moisture in the Hydrosphere	18
2.3	Water Dynamics in the Vadose Zone	20
3	Electrodynamics	27
3.1	Maxwell's Equations	27
3.2	Electromagnetic Parameters	28
3.2.1	Microscopic Phenomena	28
3.2.2	Signal Velocity, Attenuation, and Dispersion	30
3.3	Solutions to Maxwell's Equations	32
3.3.1	Analytical Solutions	32
3.3.2	Traveltime and Amplitude Calculation	33
3.3.3	Numerical Solutions	34
3.3.3.1	The Finite-Difference Time-Domain method	35
3.4	Antenna Theory	37
3.4.1	Near and Far-Field	39
3.4.2	Ground Coupling	41
3.4.3	Radiation at a Dielectric Interface	42
3.4.4	2D and 3D solutions	44
3.5	Reflections	47
3.6	Petrophysical Relationships	48
4	Ground Penetrating Radar	51
4.1	Modes of Operation	51
4.2	Measurement Setups	52
4.3	Scope of Application and Limitations	55
4.4	Evaluation Techniques	57
4.4.1	Traveltime and Amplitude Calculation	57
4.4.2	Migration	58
4.4.3	Multichannel Evaluation	60
4.4.4	Full-Waveform Inversion	60
5	Constructive Inversion	63
5.1	Measurement and Initialization	64
5.1.1	Measurements	64

5.1.2	Initial Guess	64
5.1.3	Subsurface Model Design	64
5.2	Forward Model	65
5.2.1	Measurement Simulation	65
5.2.2	2D to 3D Conversion – Frequency Correction	67
5.3	Feature Detection	67
5.3.1	Gaussian Filter Determination	68
5.3.2	Convolution	68
5.3.3	Signal Detection	71
5.3.4	2D to 3D Conversion – Amplitude Correction	72
5.4	Parameter Estimation	72
5.4.1	Pairwise Association	73
5.4.2	Objective Function	74
5.4.3	Termination Criterion	76
6	Results and Discussion	77
6.1	Performance Test and Accuracy Analysis	77
6.1.1	The ASSESS-GPR Testbed	77
6.1.2	GPR data acquisition	79
6.1.3	Synthetic Test	79
6.1.4	Real Dataset	81
6.2	Field Measurements at Hirschacker	89
6.3	The Daheigang Time-Series	98
7	Summary and Conclusions	111
A	Appendix	115
A.1	Additional Figures and Tables	115
A.2	The Ricker Source Current Density Function	116
A.3	Computational Aspects	117
	Bibliography	119

Symbols and Abbreviations

This list contains the most important symbols and notations used. Where possible, a reference (equation and page number) is given and the units (SI) are provided in brackets.

Lowercase Latin Symbols

a	antenna separation [m]	
c_0	vacuum speed of light [m s^{-1}]	
\vec{f}	forward model data vector [depends]	5.12 74
h_m	matric head [m]	2.1 20
i	imaginary unit [-]	
i	index 'i' [-]	
\vec{j}	source current density [A/m^2]	3.3 27
\vec{j}_w	volume flux of water [m s^{-1}]	2.2 21
k	circular wavenumber [m^{-1}]	
l	time-sample index [-]	
m	trace index [-]	
n	section index [-]	
p_i	pressure in phase 'i' [N/m^2]	2.1 20
\vec{p}	parameter vector [depends]	5.10 74
q	maxima index [-]	5.6 71
\vec{s}	poynting vector [$\text{J/m}^2\text{s}$]	3.24 38
t	time [s]	
\vec{x}	spatial coordinate vector [m]	2.1 20
\vec{y}	data vector [depends]	5.12 74

Uppercase Latin Symbols

A	normalized amplitude [-]	5.6 71
\vec{B}	magnetic flux density [T]	3.2 27
C	Courant stability factor [-]	3.23 36

\vec{D}	electric displacement field [As/m ²]	3.1 27
\vec{E}	electric field [V m ⁻¹]	3.3 27
\vec{F}	vector potential [T m]	3.27 44
G_l	gaussian filter [-]	5.2 68
\vec{H}	magnetic field [A m ⁻¹]	3.3 27
J	jacobian matrix [-]	5.17 75
K	hydraulic conductivity [m s ⁻¹]	2.2 21
K_0	saturated hydraulic conductivity [m s ⁻¹]	2.6 21
L	number of time samples per trace [-]	
M	number of traces per section [-]	
N	number of sections [-]	
P	number of parameters [-]	
Q	number of maxima per trace [-]	
\vec{R}	weighted residuum [-]	5.11 74
S	sensitivity matrix [-]	5.11 74
V	signal measured by GPR devices [V]	

Lowercase Greek Symbols

δ	Dirac delta distribution [m ⁻¹]	3.29 45
ε_0	vacuum permittivity [F m ⁻¹]	3.1 27
ε_r	relative dielectric permittivity [-]	3.5 27
$\varepsilon'_r, \varepsilon''_r$	real and complex part of ε_r [-]	3.1 27
ζ	smoothing width [m]	3.39 47
θ	volumetric water content [-]	2.4 21
λ	wavelength [m]	5.11 74
μ_0	vacuum permeability [H m ⁻¹]	3.3 27
μ_r	relative magnetic permeability [-]	3.3 27
ρ	charge density [Cm ⁻³]	3.1 27
ρ_w	density of water [kgm ⁻³]	
σ	electric conductivity [S m ⁻¹]	3.3 27
σ_{dc}	direct current electric conductivity [S m ⁻¹]	3.9 29
σ_\diamond	standard deviation of \diamond [depends]	
ϕ	porosity [-]	
ψ_l	discrete wavelet function [-]	
ω	angular frequency [Hz]	

Uppercase Greek Symbols

Λ	Levenberg-Marquardt damping factor [-]	5.11 74
Ω	objective function	5.10 74

Gothic Symbols

\mathfrak{M}	set of detected events
\mathfrak{P}	set of parameters

Mathematical Notation

\diamond	the quantity \diamond after convolution
$\hat{\diamond}$	the quantity \diamond after Fourier transform
$\vec{\diamond}$	vector quantity
\diamond	a generic argument

Abbreviations and Acronyms

CMP	common midpoint
CO	common offset
FDTD	finite difference time domain
FFT	fast Fourier transform
GPR	ground penetrating radar
MEEP	MIT electromagnetic equation propagation
WARR	wide angle reflection and refraction

1 Introduction

The essential role of water for the Earth system dynamics becomes evident by considering the amount of the total solar radiation power, which is consumed by the change of water from solid and liquid to the gaseous phase (23 %, [[Kiehl and Trenberth, 1997](#)]). Parts of this phase-change occurs by evapotranspiration from the vadose zone, the unsaturated part of soils above the groundwater. Soil moisture, in turn, controls the energy and water flux from the vadose zone to the atmosphere and is a key variable for net primary production. Hence, natural changes of soil moisture as well as its manipulation by agricultural practice, impacts the Earth system dynamics in various ways with differing significance (section [2.2](#)).

The attempt to predict the resulting implications relies on the understanding of the soil moisture dynamics. Since the associated processes are highly nonlinear and heterogeneous at multiple scales, they currently cannot be sufficiently described for many circumstances. This raises the need for measurement techniques, which provide quantitative information on soil moisture at different scales. Small scale descriptions of the soil moisture dynamics, in terms of water content, are readily available, e.g., in form of the Richards equation ([2.4](#)). On that basis, it can be claimed (section [2.3](#)) that a proper prediction of the water dynamics by Richards equation, relies at least on (i) knowledge on the spatial distribution of water content at several points in time, (ii) accurate water content information, (iii) the spatial distribution of materials, i.e., in a first order description the subsurface stratification, (iv) quantitative information on the boundary conditions, and (v) characterizations describing the hydraulic properties of different materials. Although the relative importance of these aspects is depending on the actual question to answer, each of them has to be addressed for most applications; at least at the scale of interest or, in some cases, below.

A variety of techniques exist to observe soil moisture. These range from centimeter scale systems, like time-domain reflectometry (TDR) probes [[Robinson et al., 2003](#)], to remote sensing techniques, such as the soil moisture and ocean salinity (SMOS) satellite [[Kerr et al., 2001](#)], which has a spatial resolution of several tens of kilometers. To answer some hydrological questions, however, the intermediate-scale is relevant, which is not satisfyingly covered by current measurement and evaluation methods [[Robinson et al., 2008a](#)].

Hydrogeophysical measurement techniques [[Rubin and Hubbard, 2005](#)], such as ground-penetrating radar (GPR), electromagnetic induction, and electrical resistivity tomography, have the capability to cover the intermediate-scale, at least with respect to their range of application. However, there is still the need for effective evaluation techniques, which fulfill the five requirements stated before, and give an optimal trade-off between detailed and accurate subsurface information, measurement effort, and computational costs.

GPR employs electromagnetic waves which are emitted by a transmitter antenna, propagate in the subsurface, and recorded by a receiver antenna. The electromagnetic properties of the subsurface modify the signals in terms of their propagation velocity, amplitude, phase, and travelpath (section 3.2.2). For instance, spatial changes of the electromagnetic properties can cause the reflection of a signal. By evaluating the traveltime, amplitude, and phase of the received signals, information on the subsurface' electromagnetic properties can be determined. Given that information, the water content can be calculated by employing a petrophysical relationship (section 3.6).

There are two basically different measurement setups, which are commonly used for GPR: (i) The application in boreholes which provides detailed information at one location and (ii) surface GPR which is favorable to answer hydrological questions at the intermediate scale, by being non-invasive, moveable with walking speed, and thus applicable on areas up to several 1000 m². More importantly, it provides an “image” of the subsurface structure from reflections at layer interface. This image is distorted, however, since the reflections' traveltimes are modified by the water contained in the layers. Several evaluation techniques are available (section 4.4) which exploit this combined information by inversely determining the subsurface structure and electromagnetic properties. Major restrictions to these methods are that (i) simplifying assumptions on the subsurface and the measurement process have to be made or (ii) a high data density is necessary to drop the simplifications and thus an increased measurement effort is involved.

In this thesis, the constructive inversion approach (section 5), being employed by *Buchner et al.* [2012], is applied to multi common-offset surface GPR measurements. The method relies on the construction of a parameterized model representing the subsurface geometry and dielectric permittivity. Employing this model, the GPR measurements are simulated by numerically solving Maxwell's equations (3.1)-(3.4) in two dimensions. With a feature detection procedure, measured and simulated signals are identified as events and their traveltime and optionally amplitude information is retrieved. The measured and modeled events are pairwise associated with each other by a heuristic approach. Then, an objective function is formulated, as the summed squared difference of the events traveltimes and amplitudes. By minimizing this objective function, an estimation problem for the parameters of the subsurface model is defined. It is solved using a Levenberg–Marquardt routine, which was modified to handle variations in the number of terms of the objective function, originating in the event association.

By design, the constructive inversion allows to focus on the data of interest and to introduce a scale of interest. Both are properties which enable to constrain the parameter estimation problem and to enhance the robustness of its solution. The construction of the subsurface model also gives the possibility to include external knowledge or assumptions on the properties of the subsurface structure and water content distribution.

The inversion method is tested for its performance and accuracy by evaluation a synthetic and real dataset (section 6.1). Both were obtained on the ASSESS-GPR testbed, which provides ground-truth information on geometry and water content. In section 6.2, the applicability to real field data is demonstrated in combination with representing the water content variability and subsurface structure by cubic spline functions. With the same approach, a time-series of measurements is evaluated (section 6.3), assuming the

layer structure to be temporally constant.

This thesis is structured as follows: A short introduction to the larger environmental context and the relevance of soil moisture measurements is given in section 2. The following section 3 provides a theoretical excursion to electrodynamic theory and phenomena, which are relevant for GPR. The latter itself, is described in section 4, including its basic principles as well as some evaluation techniques. A detailed explanation of the constructive inversion approach is comprised in section 5 and is followed by several applications of the method (section 6). Finally, the results are summarized and some conclusion are drawn in section 7, while the appendix provides some less relevant details.

2 Environmental Context

The objective of this thesis is the demonstration of a methodology which provides quantitative access to subsurface water and structure. Both are investigated as parts of the Earth system and it is the purpose of this section to discuss their relevance in this system. In addition, the factors controlling subsurface water dynamics are demonstrated and the implied requirements on measurement techniques are discussed.

2.1 The Earth System

Earth system analysis (e.g. *Schellnhuber and Wenzel* [1998], *Ehlers and Krafft* [2001]) has evolved to a scientific discipline, which permits to address questions being relevant for humankind at a global scale. Some of these questions are (i) “what are the dominant processes influencing the dynamics of the Earth system with respect to the existence of individual persons and human societies?”, and (ii) “do human societies significantly impact the Earth system and what are the implications?” Although it is not the aim of this study to address these questions to full extent, the following paragraphs might give a glimpse of how subsurface water relates to them.

One description of the Earth system is its partition into various spheres. Figure 2.1 provides one option to do that when focussing at the Earth’s surface. While the geosphere includes the components which can be associated with the physical environment, the biosphere is usually treated separately. Although, when contrasting these two spheres to the role of humans – represented by the anthroposphere – both are combined to the natural Earth or the biogeosphere (e.g. *Kabat et al.* [2004]). In general, all these spheres cannot be treated as isolated systems, since they are interdependent and overlap. The separation has its origin rather in the characteristics of the elementary units, quantities, and processes of the different spheres.

The necessary condition for maintaining the Earth system dynamics is the energy input, which is governed by solar radiation. The dynamics of subcomponents, for instance the water cycle, depends on various factors stemming from physical, chemical, and biological processes. For instance, 23 % [*Kiehl and Trenberth*, 1997] of the incoming

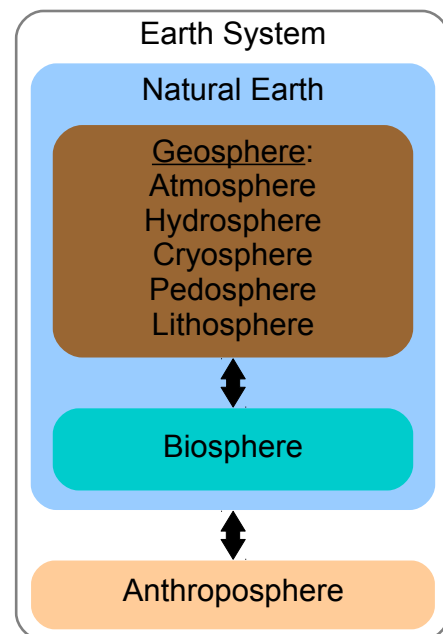


Figure 2.1: Partition of the Earth system into spheres.

solar radiation power is consumed by the phase change of solid or liquid water to the gaseous phase by the combination of evaporation and transpiration of plants. In addition, however, the anthroposphere also has a significant impact which can be illustrated by two examples: (i) about 26 % of the total terrestrial evapotranspiration and 54 % of run-off, which is geographically and temporally accessible, is used by humanity [Postel *et al.*, 1996]. (ii) 40 % of net production of organic compounds by the biosphere, which is in turn depending on soil moisture, is manipulated by human activity [Wright, 1990].

This clearly shows the relevance of water in the context of the second question raised above.

2.2 Soil Moisture in the Hydrosphere

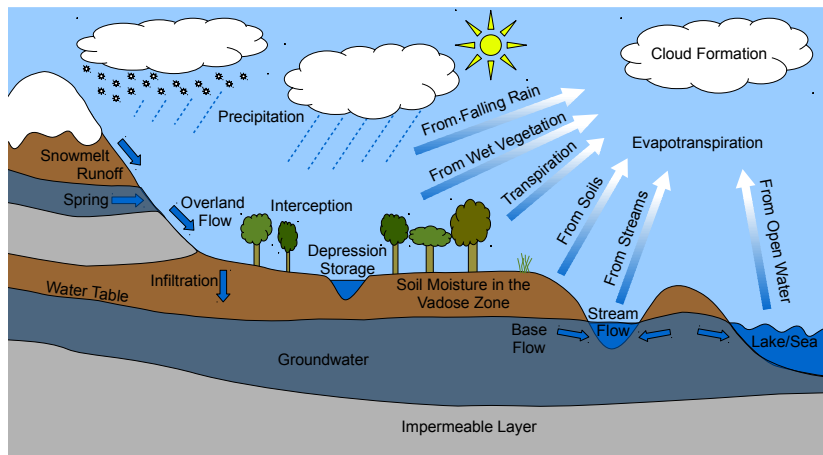


Figure 2.2: Components and processes contributing to the land part of the hydrological cycle (after Brutsaert [2005]).

A combining aspect of all spheres in the Earth system is the cycling of different materials. As such, Schaub and Turek [2011] name water, carbon, oxygen, nitrogen, sulfur, phosphorus, and chlorine. As human life and the production of agricultural goods relies crucially on the availability of water, its importance to answer the first of the above questions is evident. The hydrosphere represents the combined mass of water in the Earth system and hence the water or hydrological cycle is mainly associated with it. To identify the role of soil moisture in it, this cycle is investigated in more detail further on.

The hydrological cycle describes the exchange of water between different Earth compartments. More precisely, it describes the movement of water on, above, and below the Earth's surface. In fact, the hydrological cycle comprises several sub-cycles, e.g., the ones transporting water between the oceans and the atmosphere, the continents and the atmosphere, or between all three compartments. All these cycles can be split into sub-cycles as well, to focus on individual processes or to describe the water movement in specific regions (e.g. [Bettenay *et al.*, 1964]). Figure 2.2 gives an overview

of the different processes making up the so-called land part of the water movement. Evapotranspiration, induced by the consumption of solar radiation power, can be considered as the starting mechanism. The condensation of water leads to cloud formation which is followed by precipitation. When the latter occurs over land, the water is either temporarily stored, directly reaches open water bodies, or contributes again to evapotranspiration in various ways.

Soil moisture is only one of several storages of water (figure 2.2). In fact, the overall quantity of soil moisture in the hydrological cycle is only about 0.05 % [Robinson *et al.*, 2008a]. Nevertheless, soil moisture significantly contributes to a variety of processes:

- Since the albedo of the soil surface depends on soil moisture, the latter changes the fractioning between backscattered and absorbed solar radiation. This effect can directly be observed on a sandy beach, where the decreasing brightness of the sand is caused by the gradual increase of water content towards the sea.
- Soil moisture is relevant for the partitioning of precipitation into evapotranspiration, surface run-off, infiltration, and accordingly base flow.
- Soil moisture influences the resulting energy flux to the atmosphere and its partitioning between latent and sensible heat, via evapotranspiration and energy absorption at the soil surface.
- Almost every plant process is affected directly or indirectly by the supply of sub-surface water, since water is a plant constituent, reactant, and solvent [Kramer and Boyer, 1995]. It has, for instance, been shown that (i) soil moisture is the control variable on dryland ecosystem structure, function, and diversity [Rodríguez-Iturbe and Porporato, 2004] and (ii) water availability limits the net primary production of plants in 52 % over land areas [Churkina and Running, 1998]. The latter is of special interest for the agricultural use of soils and is one reason for the need of irrigation.
- Frozen soil water seasonally covers a significant amount – 35 % [Kabat *et al.*, 2004] – of the Earth’s surface and is stored partly in permafrost soils. This percentage is influenced by degradation of permafrost soils in response to changes in local and global climatic conditions. In case of the Qinghai-Tibet Plateau, permafrost degradation causes, among other factors, a drop of the groundwater table at the source region of the Yangtze River and Yellow River [Cheng and Wu, 2007] – two important water supplies of Eastern China. Christensen *et al.* [2004] also report that permafrost degradation can lead to an increase of methane emissions, which is an effective greenhouse gas [Lashof and Ahuja, 1990].

The above findings show that the vadose zone and the water contained in it are not only relevant as an interface between atmosphere and groundwater, but also in the coupling between the different spheres of the Earth system. This makes soil moisture a crucial quantity for precipitation forecasts [Beljaars *et al.*, 1996] and for modeling the behavior of hydrological systems [Bronstert and Plate, 1997, Vereecken *et al.*, 2008]. While this raises the need for detailed knowledge on the spatial distribution and temporal evolution

of vadose zone water content, it also demands for the understanding of the processes controlling this distribution, its dynamics, and spatial variability.

2.3 Water Dynamics in the Vadose Zone

To provide a proper terminology it is instructive to divide the subsurface, which is in general a porous medium, into two regions (i) the groundwater, where water flows freely in the pores and (ii) the vadose zone, which envelops soil and where water is bound in pores due to capillary forces. Since the latter is also characterized by the presence of water and air, it is also denoted as the unsaturated zone. The interface between the two zones is the capillary fringe.

A variety of processes take place in the vadose zone. Examples include the movement of solutes, transport of heat, mechanical stress, biomass activity, deformations as well as restructuring, caused, for instance, by agricultural activity or erosion. One process, however, which all the previous ones depend on, is the dynamics of soil water. Hence, it is studied in more detail below, following [Roth \[2011\]](#).

The liquid volumetric water content θ of a porous medium, is defined at the continuum scale as the volumetric fraction of water obtained at every point in space by averaging over a surrounding representative elementary volume. This definition, however, does not exclude θ to be a discontinuous function of space. Hence, it is more convenient to relate the water content to a quantity which is continuous in space and to describe the water dynamics in terms of this quantity. A suited one is, e.g., the matric head

$$h_m := \frac{p_w - p_a}{\rho_w g}, \quad (2.1)$$

where ρ_w is the density of water, g the acceleration by gravity, and “matric” relates to the rigid matrix of the porous medium. The pressure in the water and air phase is denoted by p_w and p_a , respectively. While both quantities are defined at the continuum scale, the relation to θ can be understood at the pore scale: The soil matrix is filled with water and air which are separated by an interface. In an equilibrium state of the microscopic forces, the curvature of this interface is linked to the pore geometry as well as to the pressure difference at the interface. The actual position of the interface, however, is not uniquely determined by the pressure difference and depends on the history of the water distribution. Hence, the relation $\theta(h_m)$ is in general also not unique and shows a hysteric behavior. In the following, however, this shall be neglected, which makes $\theta(h_m)$ only material specific. It is also noteworthy that h_m is a negative quantity in the unsaturated case, which means by definition (2.1) that $p_w < p_a$. That is, the water-air interface is cambered into the water phase, as, for instance, in a single capillary.

With the definition of h_m and the assumption of a continuous air phase, the volume flux of water is given by

$$\vec{j}_w = -K(h_m)[\nabla h_m - \vec{e}_g]. \quad (2.2)$$

Here, \vec{e}_g is the direction of the gravitational force and K is the hydraulic conductivity. The latter is depending on the cross-section of the water phase and the friction at the soil matrix. Hence, it depends on the pore geometry as well as on θ and with that on h_m . Inserting 2.2 into the mass conservation equation

$$\frac{\partial \theta}{\partial t} + \nabla \cdot \vec{j}_w = 0, \quad (2.3)$$

one obtains, after rearranging $\frac{\partial \theta}{\partial t} = \frac{\partial \theta}{\partial h_m} \frac{\partial h_m}{\partial t}$, the Richards equation:

$$\frac{\partial \theta(h_m)}{\partial h_m} \frac{\partial h_m}{\partial t} - \nabla \cdot [K(h_m)[\nabla h_m - \vec{e}_g]] = 0. \quad (2.4)$$

The solution of this non-linear partial differential equation demands for functional expressions of $\theta(h_m)$ and $K(h_m)$. One option – which is specifically suited for numerical solutions to (2.4) – to describe the so-called soil water characteristic $\theta(h_m)$ is the simplified *van Genuchten* [1980] parameterization, which is given with neglecting hysteresis by

$$\theta(h_m) = \theta_r + (\theta_s - \theta_r) \left[1 + [\alpha h_m]^n \right]^{-1+1/n}. \quad (2.5)$$

Here $\alpha < 0$ and $n > 1$ are fitting parameters, while θ_s and θ_r denote the saturated and residual water content. On the basis of (2.5) and employing the findings of *Mualem* [1976] one gets

$$K(h_m) = K_0 \left[1 + [\alpha h_m]^n \right]^{-a(1-1/n)} \left[1 - [\alpha h_m]^{n-1} [1 + [\alpha h_m]^n]^{-1+1/n} \right]^2. \quad (2.6)$$

In this equation, K_0 denotes the saturated hydraulic conductivity and 'a' is a parameter which is associated with the tortuosity of the pore geometry.

The two relationships (2.5) and (2.6) are models which express the material characteristics of a porous medium with respect to water flow. Altogether, six parameters (e.g. table 2.1) have to be determined for any material. Figure 2.3 provides examples of $\theta(h_m)$ and $K(h_m)$ for two soil textures. Both curves reveal that the quantities entering equation (2.4) can vary over orders of magnitude and differ significantly for the two soil types. Consequently, the solution of Richards equation will show different behavior, depending on the actual hydraulic properties and their spatial distribution. While the former follows from the presence of $\theta(h_m)$ and $K(h_m)$ in equation (2.4), the latter can be studied by the following two examples.

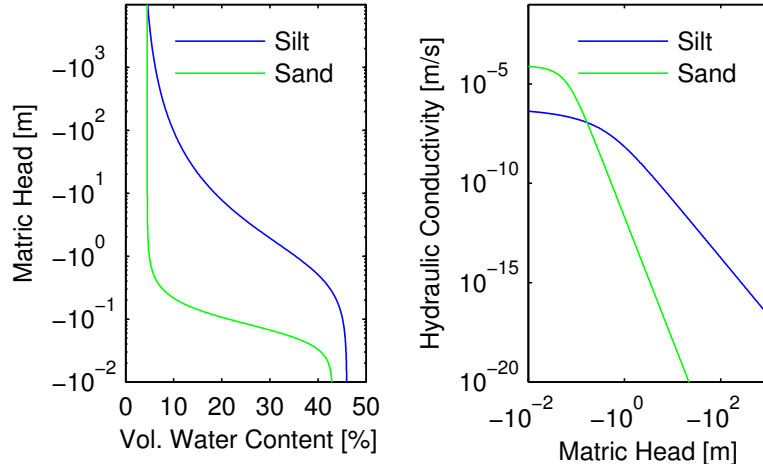


Figure 2.3: Left: soil water characteristic retrieved from (2.5). Right: $K(h_m)$ given by (2.6). The curves are calculated with the parameters provided in table 2.1.

Table 2.1: Hydraulic parameters of silt and sand [*Carsel and Parrish, 1988*].

	θ_r [%]	θ_s [%]	α [m^{-1}]	n [-]	K_0 [m s^{-1}]	a [-]
Silt	3.4	46	-1.6	1.37	$6.94 \cdot 10^{-7}$	0.5
Sand	4.5	43	-14.5	2.68	$8.25 \cdot 10^{-5}$	0.5

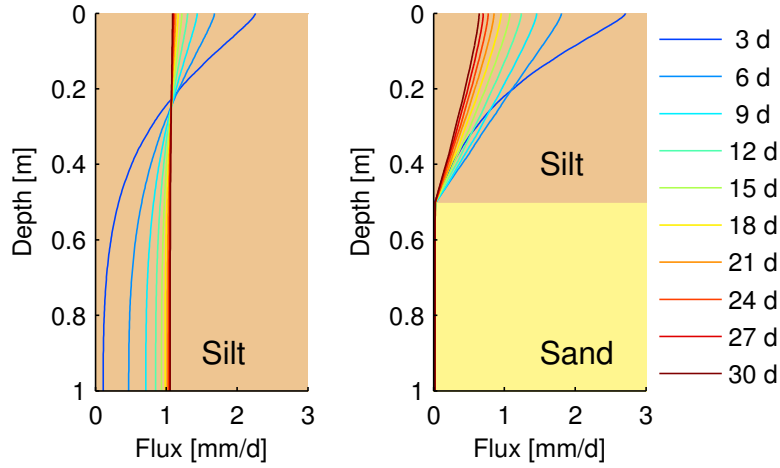


Figure 2.4: Temporal evolution of the water flux resulting from surface evaporation from a homogeneous and a two layer soil.

Evaporation A horizontal soil of 1 m thickness is considered, which consists in one case of silt and in the other case of a silt and a sand layer (figure 2.4). In both cases, the initial condition of the system is given by hydrostatic equilibrium. Over time, a constant value of $h_m = -10$ m is assumed at the surface. This, for example, represents the presence of dry air causing an evaporation flux. The water table is kept fix at 1 m depth, i.e., the water table is not lowered by the water flux induced by evaporation (the necessary recharge could be, for instance, sustained by a lake or river in the close vicinity). Richards equation is numerically solved in one dimension, using the HYDRUS-1D software package [Šimůnek et al., 2009] with the material parameters given in table 2.1. Figure 2.4 shows the resulting \vec{j}_w , which is obtained over a time span of 30 d. In the homogenous case, a temporally and spatially constant flux is approached over time. In contrast, in the two layer case, the flux mainly occurs in the silt layer, causing a reduction of water content in it and hence a permanent decrease in flux. The reason between the contrasting behavior in silt and sand is the difference in K below a value of $h_m = -0.17$ m: At the material interface $h_m = -0.5$ m at day 0 and decreases over time. Thus, the contrast in K increases (figure 2.3) which has to be compensated by $|\nabla h_m|$ to establish a flux (equation 2.2) at the interface, which is in the same order of magnitude as at the surface.

In summary, this example shows that the actual material properties and the initial state of the system control the magnitude and temporal evolution of the surface evaporation flux.

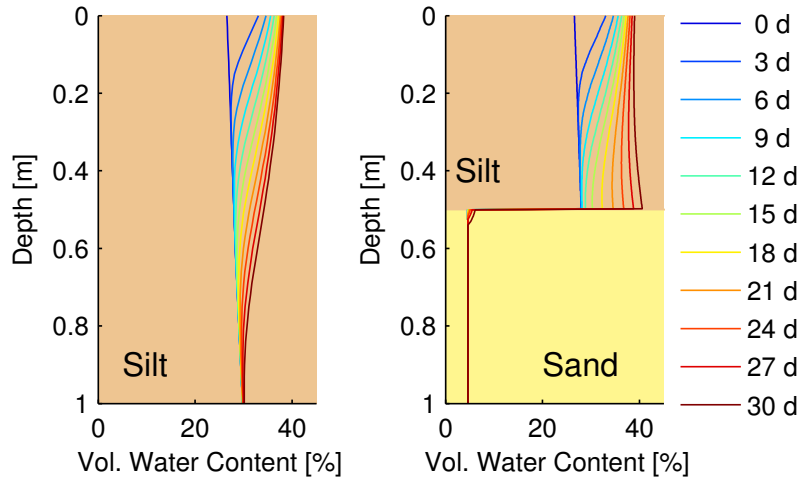


Figure 2.5: Temporal evolution of the water content distribution resulting from surface infiltration into a homogeneous and a two layer soil.

Infiltration This example is almost analogue to the evaporation example, except for two differences: (i) the domain is extended to set the water table to a fixed depth of 3 m and (ii) the upper boundary condition is an infiltration flux of 2 mm d^{-1} . Again, Richards equation is numerically solved in one dimension using the HYDRUS-1D software package [Šimůnek et al., 2009] with the material parameters given in table 2.1. The resulting water content evolution is depicted in figure 2.5. As a consequence of

the soil-water characteristic, θ is larger than 26 % at the start for the homogenous case. Afterwards, an infiltration front moves into the soil which is getting broadened over time. The two layer example shows a significantly different behavior. First of all, at the beginning $\theta \approx \theta_r$ for the sand. Second, the water infiltrates the soil similarly to the homogenous example, but at day 12 it reaches the layer interface. Afterwards, only small amounts of water enter the sand, while the rest ponds upon the interface. Again, the explanation is given by the difference in K for the two soils: The water can only infiltrate the sand if $|\nabla h_m|$ becomes large enough by ponding to compensate the difference in K . If, however, less water can infiltrate the sand than is entered by the surface flux, the silt layer will get saturated and run-off will occur at the surface.

The infiltration example demonstrates that the appearance of ponding as well as resulting surface run-off is determined by the material properties, the layers' extents, and the boundary conditions.

Although the above examples are somewhat artificial by choosing constant boundary conditions, the magnitudes do correspond to realistic conditions averaged over a time span of 30 days. These examples show that evaporation and infiltration from and into soils depend on the subsurface materials and their spatial distribution. Hence, detailed knowledge on both is necessary for any attempt to predict the water dynamics and the system's behavior at the surface.

So far, only horizontal layers of different materials and vertical water flux were considered. Under natural conditions, however, anisotropic vertical and horizontal variability of material properties is to be expected. In addition, the influence of biological activity needs to be considered and macro-pore flow has to be represented eventually. For the three-dimensional dynamics of θ , topography changes and the implied changes of the upper boundary conditions are relevant as well. These factors do, however, still not weaken the following conclusions.

The above findings illustrate that an accurate description and prediction of the subsurface water dynamics, demands for detailed information on:

1. The spatial distribution and temporal evolution of θ .
2. Highly accurate measurements of θ , because of the sensitivity of K on $h_m(\theta)$.
3. The spatial distribution of materials, i.e., most importantly the subsurface layer structure.
4. Knowledge on the boundary conditions.
5. Material characterizations which provide $\theta(h_m)$ and $K(h_m)$.

Information of the boundary conditions may be retrieved by meteorological and ground-water observations. The other requirements, however, raise the need for appropriate measurement techniques at the scale of interest. For studies on solute transport, this scale is on the order of several meters and single-point measurement techniques like time-domain reflectometry (TDR) are well suited in combination with outcrop investigations (e.g. [Roth et al. \[1991\]](#)). Concerning hydrological questions, however, the scale

of interest is several 10 m and far above [Robinson *et al.*, 2008b]. Remote sensing techniques are covering this scale at the far end, although with a lack of penetration depth. Hence, there is the need for measurement techniques, which are able to close this intermediate scale gap [Robinson *et al.*, 2008a]. Geophysical measurement techniques like surface GPR have the potential to achieve this by efficient and non-invasive operation of measurements. More importantly, GPR also provides information which depends on the subsurface stratification and dielectric permittivity distribution, the latter being directly linked to θ (section 3.6).

It is the purpose of this study to demonstrate a novel GPR evaluation technique – the constructive inversion of multi common-offset surface GPR measurements – which addresses the three of the above requirements.

3 Electrodynamics

In this section the theoretical background for the description of the GPR measurement process is summarized. Thus, Maxwell's equations are introduced and the implications of material properties on electromagnetic waves are investigated in detail. Various approaches for the solution to Maxwell's equations are compared including different numerical methods. After a short introduction to antennas, relevant electrodynamic phenomena in this context are discussed. Finally, reflections at sharp interfaces and smooth boundaries are compared and petrophysical relationships are introduced.

3.1 Maxwell's Equations

The GPR measurement process is based on the emission of electromagnetic signals which propagate in the subsurface. These signals are described by the electromagnetic fields, which are composed of the electric field \vec{E} , the electric displacement field \vec{D} , the magnetic flux density \vec{B} , and the magnetic field \vec{H} . Maxwell's equations provide a quantitative description of the dynamics of these fields and for isotropic matter, the macroscopic equations may be written as:

$$\nabla \cdot \vec{D} = \rho \quad (3.1)$$

$$\nabla \cdot \vec{B} = 0 \quad (3.2)$$

$$\nabla \times \vec{H} - \frac{\partial \vec{D}}{\partial t} = \sigma \vec{E} + \vec{j} \quad (3.3)$$

$$\nabla \times \vec{E} + \frac{\partial \vec{B}}{\partial t} = 0. \quad (3.4)$$

Here, \vec{j} represents the internal and source current density, while ρ denotes the internal volume charge density – which is assumed in the following to be zero away from any source current in the absence of a time-dependent electromagnetic field (neutral medium). Magnetic effects are neglected in the following and then $\vec{H} = \vec{B}/\mu_0$ is valid, with μ_0 being the vacuum magnetic permeability. For linear, isotropic, dispersive, heterogeneous media the relation between \vec{D} and \vec{E} is given by using their frequency-domain counterparts (denoted by $\hat{\diamond}$) as

$$\hat{\vec{D}} = \hat{\varepsilon} \hat{\vec{E}}. \quad (3.5)$$

Here, $\varepsilon = \varepsilon_0 \varepsilon_r$ is the dielectric permittivity of the subsurface, which is in general a frequency dependent and a complex quantity. If the latter is relevant in following, this is expressed by explicitly using ε'_r and ε''_r , which are the real and the imaginary part of ε_r , respectively. To solve Maxwell's equations in the time-domain, the inverse Fourier

transform of (3.5) has to be employed, which introduces an integral expression. This can only be simplified for monochromatic waves – the time-harmonic solution – or for non-dispersive materials, for which the frequency dependency of ε vanishes. For some solutions, the electromagnetic fields are given as complex quantities. To compare them to measured values or to investigate the solution, however, the corresponding real parts are used instead.

3.2 Electromagnetic Parameters

For a quantitative analysis of GPR signals, in terms of their traveltime and their amplitude evolution when propagating through a medium, a detailed understanding of the quantities ε and σ is essential. The above formulation of equations (3.1)-(3.4) would allow a generalized formulation of ε which includes σ . However, since these quantities are usually treated separately in numerical methods and in geophysical applications, a combined formulation is only employed if necessary.

3.2.1 Microscopic Phenomena

Regarding the materials observed for of this study, three relevant microscopic processes are influencing ε and σ in their magnitude as well as their frequency dependency. Which process significantly contributes at the frequency range of GPR depends on the observed materials and needs to be determined empirically.

Temporary Molecular Polarization From a classical perspective, atomic-bound electrons encounter a force in the presence of an external electric field. Since they are bound they also encounter, in addition to friction, a counteractive force. This stems from atomic forces which depend linearly on the electrons' displacement. Thus in the presence of a time-dependent harmonic external field, their kinetic behavior can be described by a damped harmonic oscillator. The spatial displacement of the electrons induces a dipole moment, which in turn contributes to the macroscopic polarization of the material and with that to ε_r . This may be described by Drude's formula (e.g. [Jackson \[2006\]](#)) as

$$\varepsilon_r = 1 + \frac{Xe^2}{\varepsilon_0 m_e} \sum_j z_j \frac{1}{\omega_j^2 - \omega^2 - i\omega\gamma_j}. \quad (3.6)$$

Here, X is the number of molecules in the observed volume, e and m_e the electron charge and mass, while z_j denotes the number of electrons with the same resonance frequency ω_j and damping constant γ_j . This description also holds from a quantum-mechanical perspective with proper definitions of z_j , ω_j , and γ_j .

Unbound Charges Unbound charges can be given by electrons or, as more likely in the subsurface, by ions. Both can be equivalently treated with respect to their impact on ε_r , if the different masses and damping constants are considered. Since more instructive, electrons are treated in the following.

The resonance frequency of bound electrons defines the magnitude of the counteractive force the electrons encounter. In contrast, the fraction z_o of unbound electrons does not encounter this force, which is equivalent to $\omega_0 = 0$. This gives their contribution to ε_r from equation (3.6), with separating the terms of the bound electrons $\varepsilon_{r,b}$, as

$$\varepsilon_r = \varepsilon_{r,b} + i \frac{X e^2 z_o}{\varepsilon_0 m_e \omega (\gamma_o - i\omega)}. \quad (3.7)$$

The conductivity σ was introduced by Ohm's law ($\vec{j}_{\text{Ohm}} = \sigma \vec{E}$) and thus describes the charge current density of unbound electrons in the material. Hence is associated with the result of (3.7) by

$$\sigma = \frac{X e^2 z_o}{m_e (\gamma_o - i\omega)} = \frac{\sigma_{dc}}{1 - i\omega/\gamma_o}, \quad (3.8)$$

with the direct current conductivity for $\omega = 0$ being

$$\sigma_{dc} := \frac{X e^2 z_o}{m_e \gamma_o}. \quad (3.9)$$

That is, conductivity contributes to dielectric permittivity with a real and imaginary part, although the latter can be neglected for small frequencies if $\omega \ll \gamma_o$, which is the case for many materials [Jackson, 2006]. This simplification also makes σ approximately independent of frequency, which leads to the typical representation, given only by σ_{dc} . However, the contribution to permittivity is still frequency dependent and thus a potential reason for dispersive effects.

Dipole Relaxation The molecules of some substances, e.g., water and various alcohols, have permanent dipole moments which are not coherently aligned in general; i.e., the medium is not polarized at the macro-scale. If the dipole moments are exposed to an external time-dependent electromagnetic field, however, they encounter an angular momentum which aligns them parallel to the external field. Thus, the medium gets macroscopically polarized and its dielectric permittivity is affected. However, the alignment is not instantaneous and thus not necessarily synchronous with the exciting external field. The phenomenon of dielectric or dipole relaxation is commonly associated with the time-lag between the response of the dipoles to the external field [Crossley, 1971]. Since the dipole alignment is influenced by intermolecular forces as well as the thermal motion of the molecules, one expects the relaxation process to depend on the frequency of the external field as well as the temperature and viscosity of the observed medium. The frequency dependency of ε_r for one relaxation process is macroscopically described by the Debye model

$$\varepsilon_r = \varepsilon_{r,\omega=\infty} + \frac{\varepsilon_{r,\omega=0} - \varepsilon_{r,\omega=\infty}}{1 + i\omega\tau}, \quad (3.10)$$

where τ is the process' relaxation time. However, already Crossley [1971] reports that this model is not appropriate for all substances because several relaxation processes are relevant. Thus, models are preferred which describe several independent relaxation processes or assume a distribution of relaxation times.

The subsurface materials which were observed for this thesis, are soils consisting of a mixture of the soil-matrix, air, and water. In the GPR frequency range, the real part of dielectric permittivity of water ($\varepsilon'_{r,w}$) at 20°C is high (80.2, [Kaatze \[1989\]](#)), compared to that of air ($\varepsilon'_{r,a} = 1$), and that of the soil matrix ($\varepsilon'_{r,s} = 3.75$ for quartz at 1 MHz [[Weast, 1973](#)]). Since ε''_r of the other quantities is negligible, water dominates the composed dielectric permittivity ($\varepsilon_{r,c}$, section 3.6) of the mixture. Hence, the general trend of the frequency dependency of $\varepsilon_{r,w}$ (as observed by [Kaatze \[1989\]](#), [Buchner et al. \[1999\]](#), [Nussberger \[2005\]](#)), which is dominated by dipole relaxation, applies also for $\varepsilon_{r,c}$. For coarse materials, as sand, $\varepsilon''_{r,c}$ is often neglected and $\varepsilon'_{r,c}$ considered to be frequency independent in the GPR frequency range. However, with decreasing pore size, more and more water is in close proximity of the soil matrix and interfacial forces hinder a larger fraction of dipole moments to get aligned in response to the external field. This results in a downward shift of the relaxation frequency $\omega_{\text{rel}} = 1/\tau$ and reduces ε'_r for smaller frequencies [[Hoekstra and Delaney, 1974](#), [Or and Wraith, 1999](#)]. Hence, for certain soils as clay, the frequency dependency of ε'_r might have to be considered and ε''_r increases what can lead to a significant attenuation of electromagnetic signals.

The dipole relaxation process also shows a strong temperature dependency, which effects ε_r in the GPR frequency range. Nevertheless, this effect can be corrected if necessary, e.g., with the findings of [Kaatze \[1989\]](#).

3.2.2 Signal Velocity, Attenuation, and Dispersion

How ε_r and σ effect an electromagnetic signal can most effectively be understood by investigating a plane monochromatic wave propagating in a charge free ($\rho = 0$) homogeneous medium in which $\sigma = \sigma_{dc}$. Since the wave is monochromatic, (3.5) also holds in the time-domain for this single frequency. Then, by taking the time-derivative of (3.3) and interchanging the derivate with the rotation operator, (3.4) can be inserted into (3.3). After employing the equality $\nabla \times \nabla \times \vec{E} = \nabla(\nabla \cdot \vec{E}) - \nabla^2 \vec{E}$ and (3.1) one obtains the telegrapher equations

$$\nabla^2 \vec{E} = \varepsilon \mu_0 \frac{\partial^2 \vec{E}}{\partial t^2} + \sigma_{dc} \mu_0 \frac{\partial \vec{E}}{\partial t} + \mu_0 \frac{\partial \vec{j}}{\partial t}. \quad (3.11)$$

Assuming $\vec{j} = 0$, this equation can be solved with the ansatz

$$\vec{E} = \vec{E}_0 e^{i(\beta x_1 - \omega t)} e^{-\frac{\alpha}{2} x} \quad (3.12)$$

which describes a plane monochromatic wave with the frequency ω propagating in direction \vec{e}_1 with a velocity of $v = \frac{\omega}{\beta}$, while it is damped with the damping constant $\alpha/2$. By inserting the ansatz into (3.11) one finds the dispersion relation

$$\beta^2 - \frac{\alpha^2}{4} + i\beta\alpha = \mu_0 \varepsilon_0 \omega^2 \underbrace{\left(\varepsilon_r + i \frac{\sigma_{dc}}{\varepsilon_0 \omega} \right)}_{\varepsilon_{r,g} := \varepsilon'_{r,g} + i\varepsilon''_{r,g}}, \quad (3.13)$$

where the generalized relative dielectric permittivity $\varepsilon_{r,g}$ was introduced for convenience. The question how α and β depend on $\varepsilon'_{r,g}$ and $\varepsilon''_{r,g}$ is answered by comparing

the real and imaginary parts on both sides of (3.13). After some calculations one obtains

$$\alpha = \frac{\sqrt{2}\omega}{c_0} \left(\sqrt{\varepsilon_{r,g}'^2 + \varepsilon_{r,g}''^2} - \varepsilon_{r,g}' \right)^{1/2} \quad (3.14)$$

$$\beta = \frac{\omega}{\sqrt{2}c_0} \left(\sqrt{\varepsilon_{r,g}'^2 + \varepsilon_{r,g}''^2} + \varepsilon_{r,g}' \right)^{1/2}. \quad (3.15)$$

These two relations express the commonly known fact that if $\varepsilon_{r,g}'' = 0$, no attenuation is present and the signal velocity is given by $c_0/\sqrt{\varepsilon_{r,g}'}$. However, if this is not the case one has to consider that both $\varepsilon_{r,g}'$ and $\varepsilon_{r,g}''$ influence velocity as well as attenuation, for instance if $\sigma_{dc} \neq 0$. Additionally, $\varepsilon_{r,g}$ is in general frequency dependent and with that also α and β , i.e., the wave propagation velocity and signal attenuation depends on ω as well. Thus, dispersive effects occur and signals which are composed of different frequencies will change their shape with time and distance. This effect also occurs if $\varepsilon_{r,g}''$ is determined by σ_{dc} only and σ_{dc} is large: Assuming $\vec{j} = 0$ and ε to be real valued, the right hand side of equation (3.11) can be expressed as

$$\mu_0(\varepsilon' + \frac{\sigma_{dc}}{\omega})\omega^2 \vec{E}, \quad (3.16)$$

by replacing the time derivative by a characteristic time scale of the system (e.g. $1/\omega$). If $\sigma_{dc}/\omega \gg \varepsilon'$, the term with σ_{dc} in (3.11) becomes dominant and the equation is effectively a diffusion equation. This is the case for pure water with $\varepsilon_r' = 80.2$ at 20 °C [Kaatze, 1989] for a frequency of 200 MHz if $\sigma_{dc} \gg 1 \text{ S m}^{-1}$.

Equations (3.14) and (3.15), allow to estimate if dispersive effects have to be considered in pure water as well as for high conductivities and how strong signal are attenuated at the same time. However, for this analysis it is convenient to simplify the two equations by replacing the square root terms with their second order taylor expansion, i.e., $\sqrt{\varepsilon_{r,g}'^2 + \varepsilon_{r,g}''^2} \approx \varepsilon_{r,g}' + \frac{\varepsilon_{r,g}''^2}{2\varepsilon_{r,g}'}$. With that, one can estimate the impact of the $\varepsilon_{r,g}''$ on the signal velocity $v = \omega/\beta$ when comparing to v_0 , which is found for $\varepsilon_{r,g}'' = 0$. The relation of both velocities is given by

$$\frac{v - v_0}{v_0} = \frac{1}{\sqrt{1 + \frac{\varepsilon_{r,g}''^2}{2\varepsilon_{r,g}'^2}}} - 1. \quad (3.17)$$

Now, assuming that $\varepsilon_{r,g}''$ is only determined from direct current conductivity, one finds: If the impact on velocity should be smaller than 1 % for a 200 MHz signal propagating in water with $\varepsilon_r' = 80.2$ at 20 °C, σ_{dc} needs to be smaller than 0.18 S m^{-1} ; and this limit increases linearly with frequency. On the other hand, the signal is also attenuated by a factor $e^{-\frac{\alpha}{2}x}$ if $\sigma_{dc} \neq 0$. For the above values, this causes a signal attenuation of 98 % on 1 m, which would make a GPR survey in saturated soils operationally problematic. Thus under normal conditions, when the signal strength is sufficient, dispersive effects induced by direct current conductivity can be neglected.

Similar effects as caused by σ_{dc} can be induced by ε_r'' . The magnitude of this quantity for water and soils in dependency on frequency and temperature is object of various

studies (e.g. *Hoekstra and Delaney* [1974], *Kaatze* [1989], *Buchner et al.* [1999], *Nussberger* [2005], *Jackson* [2006]). However, the results for water are diverse in the GPR frequency range and the frequency dependency of ε_r'' as well as the attenuation depends on the soil type and its volumetric water content. Thus, the question if the resulting attenuation has a significant impact – considering the precision of amplitude information employed in this study – cannot uniquely be answered. Additionally, the employed numerical solver (section 3.3.3) of Maxwell's equations does only provide an indirect representation of ε_r'' via σ_{dc} which is strictly only valid for a small frequency band. Hence, either this option is taken or, if plausible on the basis of the data and considering precision of amplitude information, ε_r'' is neglected.

3.3 Solutions to Maxwell's Equations

To solve equations (3.1) - (3.4) is in general a non-trivial problem, because of the coupling of the equations and the spatial dependency of the electromagnetic properties. Thus analytical solutions, simplified phase-velocity approaches, as well as numerical simulations are options. The optimal choice depends on the particular research question and the possible system simplifications.

3.3.1 Analytical Solutions

If the electromagnetic properties can be assumed to be independent of the electromagnetic field, equations (3.1) - (3.4) are a system of linear partial differential equations. In this case, the superposition principle applies. It states that two solutions to the equations can be linearly combined to obtain one common solution. This can easily be verified by inserting the sum of two solutions into equations (3.1) - (3.4) and by exploiting the linearity of the differential operators. In addition, this also allows to give any solution to the equations by its representation in an appropriate function space. By choosing plane waves ($e^{i(\vec{k}\vec{x}-\omega t)}$) as the basis functions of the Fourier space, this representation can be retrieved for any solution by expressing all the quantities $\vec{E}, \vec{D}, \vec{B}, \vec{H}, \vec{j}$, and ρ with $\diamond(\vec{x}, t) = \int_{-\infty}^{\infty} \hat{\diamond}(\vec{k}, t) e^{i(\vec{k}\vec{x}-\omega t)} d\vec{k} d\omega$ where $\hat{\diamond}(\vec{k}, t) = \int_{-\infty}^{\infty} \diamond(\vec{x}, \omega) e^{-i(\vec{k}\vec{x}-\omega t)} d\vec{x} d\omega$. Assuming homogeneous electromagnetic properties, inserting the integral representations into (3.1) - (3.4) and interchanging the differential operators with the integration leads to the equations

$$\int_{-\infty}^{\infty} [i\vec{k} \cdot \hat{\vec{D}} - \hat{\rho}] e^{i(\vec{k}\vec{x}-\omega t)} d\vec{k} d\omega = 0 \quad (3.18)$$

$$\int_{-\infty}^{\infty} [i\vec{k} \cdot \hat{\vec{B}}] e^{i(\vec{k}\vec{x}-\omega t)} d\vec{k} d\omega = 0 \quad (3.19)$$

$$\int_{-\infty}^{\infty} [i\vec{k} \times \hat{\vec{H}} + i\omega \hat{\vec{D}} - \sigma \hat{\vec{E}} - \hat{\vec{j}}] e^{i(\vec{k}\vec{x}-\omega t)} d\vec{k} d\omega = 0 \quad (3.20)$$

$$\int_{-\infty}^{\infty} [i\vec{k} \times \hat{\vec{E}} - i\omega\hat{\vec{B}}] e^{i(\vec{k}\vec{x} - \omega t)} d\vec{k} d\omega = 0. \quad (3.21)$$

The left hand sided of the above equations are, by definition, the inverse Fourier transform of the terms in brackets. Since this is also holds for the right hand sides, a set of algebraic equations is found – the Fourier transformed Maxwells equations. By linking ω and $|\vec{k}|$ via the electromagnetic properties, these equations show that their solutions differ only by constants for different frequencies. Hence, it often suffices to determine the solution to Maxwell's equations in the frequency-wavenumber domain, or in other words for a plane wave, and perform the inverse Fourier-transformation if necessary. As two among many alternatives, the solution can also be obtained in the frequency domain and by assuming a spherical wave (e.g. [Sommerfeld \[1909\]](#)) or in the time-domain by employing the retarded vector potential, given in (3.28).

Although analytic closed-form solutions are very effective by being generic, they often involve complex calculations and negligence of higher order terms when series expansion are employed. Hence, they are also approximative to some degree and higher order effects can be overlooked by their application (as discussed by [Ott \[1942\]](#)). Additionally, for many approaches strong simplifications of the spatial distribution of electromagnetic properties are necessary (e.g. [Sommerfeld \[1909\]](#), [Weyl \[1919\]](#), [Dai and Young \[1997\]](#)). This also holds when this type of solutions are applied in the context of GPR. For instance, for methods based on a Green's function description of the subsurface, the distribution of electromagnetic properties is assumed to have rotational symmetry (e.g. [Lambot et al. \[2004a\]](#), [van der Kruk et al. \[2006\]](#), [Busch et al. \[2011\]](#)).

3.3.2 Traveltime and Amplitude Calculation

For an electromagnetic wave, which propagates through a medium, the “traveltime” of the wave is given by the time which points of common phase need to cover a certain distance. For some specific cases and by formulating a dispersion relation, which links ω and k via the electromagnetic properties, the computation of this traveltime is equivalent to solving Maxwell's equations, also for arbitrary distributions of the electromagnetic properties. In general, however, this is only a first order solution which delivers the shortest traveltime and higher order effects, e.g. like refracted or reflected waves, are only provided by special methods or have to be treated explicitly.

The calculation of traveltimes and amplitude decays for electromagnetic and seismic waves is formally analog; thus the methods which are developed for the latter can also be employed in case of GPR. In the last decades many methods arose which are summarized in the following. The most straight forward one is a ray-tracing method where a homogeneous distribution of material properties and flat reflection interfaces are assumed. This allows to directly calculate the waves's travelpaths and traveltimes (e.g. [Gerhards et al. \[2008\]](#)). More sophisticated ray-tracing methods can also be applied to heterogeneously distributed material properties. For instance, the shooting method [[Julian and Gubbins, 1977](#)] iteratively determines the direction in which a wave starts to propagate, when traveling along the fastest path to the point of observation. However, this can be more efficiently achieved by the bending method [[Julian and Gubbins, 1977](#)]

where an initially guessed ray-path is perturbed to obtain the fastest one. Alternatively, the fastest path can also be determined on a network of nodes [*Nakanishi and Yamaguchi, 1986*]. Other approaches are based on wavefront propagation, which has the advantage that multiple arrivals are intrinsically captured. The wavefront propagation can either be computed by tracking the wavefronts using finite-difference extrapolation [*Vidale, 1988*] or by iteratively constructing them with local ray-tracing [*Vinje et al., 1993*]. Optionally, the propagation of wavefronts is retrieved from solving the eikonal equation by propagating a level-set function, using the fast marching method [*Sethian, 1996*]. The latter method has been shown to be unconditionally stable, computationally efficient, and able to handle velocity heterogeneities which cover more than an order of magnitude [*Rawlinson and Sambridge, 2004*].

Since direct waves are of primary interest in traveltime and amplitude tomography with borehole radar, the above methods are especially suited to efficiently solve the involved inversion problem (e.g. applied by *Troncke et al. [2004]*, *Giroux et al. [2007]*, *Göktürkler and Çağlayan Balkaya [2010]*). The various methods have in common that they demand a significantly lower computation effort compared to numerical solutions to Maxwell's equations (section 3.3.3). However, they have the disadvantage that some effects like head waves [*Vidale, 1988*] are not covered by all methods or reflections from interfaces have to be explicitly treated (e.g. *Rawlinson and Sambridge [2004]*). In addition the inclusion of amplitudes requires to represent damping, geometrical spreading, and the radiation pattern (section 3.4) of the transmitting and receiving antenna [*Vinje et al., 1993*, *Zhou and Fullagar, 2001*]. The latter, however, has been shown by *Holliger et al. [2001]* to be problematic in case of water-filled boreholes. This is caused by the non-linearity of the problem, induced by the dependency of the radiation pattern on the electromagnetic parameters which are to be determined by the inversion. In addition, the representation of special electromagnetic effects such as wavelet shape changes (section 3.4.3) and reflections from smooth changes of the permittivity profile (section 3.5) have to be treated separately.

3.3.3 Numerical Solutions

Numerical solutions allow to solve Maxwell's equations for very general problems in terms of the spatial distribution of ρ and \vec{j} . This also holds for the electromagnetic properties, which can even be included if being dispersive or non-linear. However, the utilization of any numerical method involves, besides the computational effort, the drawback of accessing only specific and approximate solutions on a limited spatial and temporal domain.

To solve electromagnetic problems, various numerical methods are available. Among the ones operating in the time-domain on unstructured grids are the finite-element method [*Jin, 2002*], the finite-volume method [*Piperno et al., 2002*], and the discontinuous Galerkin method [*Fezoui et al., 2005*]. The advantage of all these is their ability to deal with complex geometries. However, changes of the geometry – which are inherent in the inversion method presented here (section 5) – require a new mesh generation. More importantly, the computational effort of the above methods can be large, compared to the one of the finite-difference time-domain (FDTD), depending on the actual

setup. For instance, a comparison of the COMSOL Multiphysics finite-element package with the FDTD simulation software package MEEP (section 3.3.3.1) showed a computation time gain of two orders of magnitude for the latter; when considering a simple layer geometry, a point source, and a comparable grid size. Hence, the FDTD method is employed in the course of this study. In the next section, some aspects which are relevant for its application will be discussed briefly.

3.3.3.1 The Finite-Difference Time-Domain method

The FDTD method, based on the algorithm of Yee [1966], is a standard method [Taflave and Hagness, 2000] for the solution of electromagnetic problems, also in the context of GPR (e.g. Taflave and Hagness [2000], Lampe et al. [2003], Giannopoulos [2005]). The solution to Maxwell's equations is achieved by first defining a structured and in most cases rectangular or even cubic grid with the spatial resolution $\Delta x = \Delta y = \Delta z$. Assuming non-dispersive media and ε to be real valued, one obtains $\vec{D} = \varepsilon \vec{E}$ from (3.5). Then, equations (3.3) and (3.4) – the other two are intrinsically incorporated by the algorithm – are discretized by assuming spatially constant values of all quantities on each grid cell and by approximating the spatial and temporal derivatives by Taylor expansions. By neglecting all terms higher or equal to quadratic order, linear approximations of the derivatives are obtained; for instance as central differences. Yee [1966] showed that using individual grids for \vec{E} and \vec{B} which are shifted by $\Delta x/2$ increases the robustness of the method. Similar, the temporal update of the electromagnetic fields is obtained in a leap-frog manner, i.e., \vec{E} and \vec{B} are computed with a fixed temporal discretization Δt , but shifted to each other by $\Delta t/2$.

One important benefit of the FDTD method is that it is fully explicit in computation. Thus, no matrix inversion is necessary, which is the main reason for the gain in computation time mentioned above. The FDTD method requires the user to define constant values of the electromagnetic properties on each grid cell, which makes a special treatment of discontinuous materials necessary (as described below and in section 5.2). A disadvantage of the method is the necessity of a homogeneous and temporally constant spatial and temporal discretization. Hence, no spatial and temporal adaptivity is possible.

Because the computational effort decreases by a factor as high as the number of grid cells in one-direction, the solutions are preferably obtained, as in this study, in two-dimensions rather than in three-dimensions. For this, all quantities occurring in equations (3.3) and (3.4) are assumed to be invariant in z-direction, which cancels all spatial derivatives in this direction. With that, two independent systems of equations are obtained for $\vec{E}_z, \vec{B}_x, \vec{B}_y$ and $\vec{E}_x, \vec{E}_y, \vec{B}_z$, while their solutions are identified with the TE_z and TM_z mode, respectively. In the following only the TE_z mode will be considered.

Besides the domain definition, the spatial and temporal discretization have to be chosen appropriately to achieve a sufficiently accurate solution to the actual electromagnetic problem with an acceptable computational effort. While an upper limit to grid resolution is defined by the available computational resources, there are two criteria which need to be fulfilled to address the following issues.

Numerical Dispersion Due to the discretization of Maxwell's equations and the representation of the differential operators by finite differences, numerical dispersion is incorporated inherently. This expresses in a two-dimensional dispersion relation [Tafløve and Hagness, 2000] linking the frequency ω and wavenumber k of a plane monochromatic wave propagating with the speed $c = c_0/\sqrt{\varepsilon_r}$, to the temporal and spatial discretization:

$$\left[\frac{1}{c\Delta t} \sin\left(\frac{\omega\Delta t}{2}\right) \right]^2 = \left[\frac{1}{\Delta x} \sin\left(\frac{k_x\Delta x}{2}\right) \right]^2 + \left[\frac{1}{\Delta y} \sin\left(\frac{k_y\Delta y}{2}\right) \right]^2 \quad (3.22)$$

By employing the Taylor expansion to first order terms of the 'sin' function, one can find that (3.22) converges to the analytical dispersion relation $\omega/c = |\vec{k}|$ for $\Delta t \rightarrow 0$ and $\Delta x \rightarrow 0$. However, this limit will not be reached in application, thus some details of equation (3.22) are relevant: (i) The numerical phase velocity $v = \omega/k$ only coincides with c in the previous limit. Figure 3.1 reveals a significant change of phase velocity with the number of grid points per wavelength. Additionally, the results are found to depend on the direction of propagation $\vec{k}/|\vec{k}|$; a fact which results from the presence of k_x and k_y in (3.22). (ii) Figure 3.1 also shows an increase in phase velocity if the number of grid points per wavelength is smaller than two. (iii) Tafløve and Hagness [2000] show that the application of arcsin to obtain v from (3.22) can cause k to become complex. Besides the necessarily induced damping of the wave (section 3.2.2), this can cause $v/c_0 > 1$, as well.

For practical applications the number of grid points per wavelength should be about 10 for all frequencies significantly contributing to the computed signal.

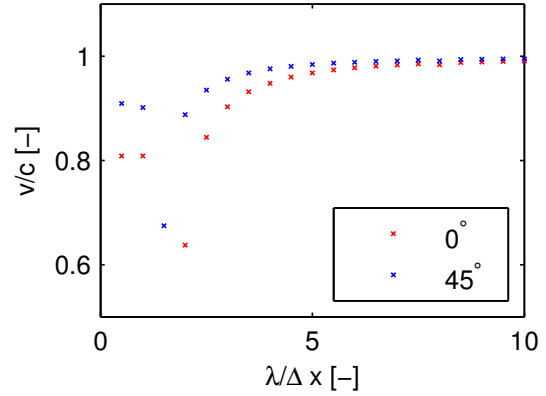


Figure 3.1: Phase velocity of a circular monochromatic wave, depending on the number of grid cells per wavelength. The data were obtained parallel (0°) and diagonal (45°) to the grid axis by automatically detecting extrema of \vec{E}_z at different positions.

Stability To prevent unstable solutions for a given spatial resolution, the following criterion has to be fulfilled for the Courant stability factor

$$C := c\Delta t \sqrt{\frac{1}{\Delta x^2} + \frac{1}{\Delta y^2}} < 1. \quad (3.23)$$

Here $c = c_0/\sqrt{\varepsilon_r}$ and thus the largest value for c in the spatial domain, which is c_0 in most cases, limits Δt . The criterion (3.23) can be intuitively understood for the

one-dimensional case for which the second summand in the root can be dropped: The time $\Delta x/c$ is necessary for a wave to propagate between two grid cells. If Δt is chosen larger than this time, the algorithm attempts to propagate the wave over more than one grid cell per time-step. However, the given discretization of the differential operators implicates that information can only be transported between neighboring grid-cells. Hence, the attempt cannot succeed and possibly results in an unphysical exponential growth of the electromagnetic field with time [Taflove and Hagness, 2000]. For the calculations performed later on, C is always set to 0.5.

The numerical solutions to Maxwell's equations presented in this study are all obtained with MEEP [Oskooi et al., 2010], which is a FDTD simulation software package, to which an interface for GPR modeling has been added by the author. The implementation employs central differences for the finite-difference calculation and is second order accurate. This accuracy is achieved for output variables which are requested at arbitrary positions, by bilinear interpolation of the variables' values at neighboring grid-cells. The reverse procedure, named restriction as the transpose of interpolation, is employed by MEEP to enable the definition of point source-current densities at arbitrary positions. To maintain second order accuracy at discontinuities in the distribution of electromagnetic properties a subpixel-smoothing routine, based on perturbation theory, is implemented in MEEP. Farjadpour et al. [2006] demonstrate that this procedure improves the accuracy of the FDTD solution when modeling discontinuous dielectric materials. The resulting convergence properties of MEEP are studied in detail by Oskooi et al. [2009] and Oskooi et al. [2010] and the authors show that the second order accuracy is achieved, indeed.

All calculations for this study are obtained on a structured squared grid. As boundary conditions, the perfectly matched layers implemented in MEEP are employed and all fields and current densities are set to zero as initial conditions.

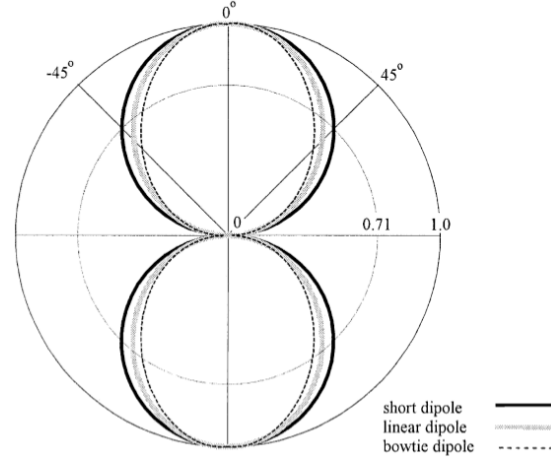
3.4 Antenna Theory

At the core of the GPR measurement technique is the GPR antenna system, which radiates a transient electromagnetic field into the subsurface and receives the modified response of that field. Hence, understanding of the antenna as a part of the electro-dynamical setting and the implications of its operation at the air-subsurface interface is crucial.

The question “what is an antenna from an electro-dynamical perspective?” is answered basically as it follows: An antenna is a conducting material at which a time-dependent source current density \vec{j} is present. The necessity of a time-dependent \vec{j} becomes obvious from (3.11). Solving the equation as an initial value problem assuming $\vec{E}|_{t=0} = 0$, the solution only becomes non-trivial if $\frac{\partial \vec{j}}{\partial t} \neq 0$. The very general definition given above explains the huge variety of antennas (wire, loop, array, dipole, horn, etc.) which has evolved since electrical engineering became operationally possible. This also means, that the different antenna designs have significant implication on the antennas' characteristics which are quantified by several properties, of which the most relevant ones are introduced:

Charge Current Distribution and Time Dependency If an excitation voltage is applied at the so-called feed point, the antenna's design causes a specific distribution of the source current density \vec{j} . In addition, the amplitude and time-dependency of the excitation voltage determine the amplitude and time-dependency of $\vec{j}(\vec{x}, t)$. The resulting electromagnetic field can then be computed by solving equations (3.1) - (3.4) with the function $\vec{j}(\vec{x}, t)$ and by representing the antenna itself as a conducting body. This computation, however, is only feasible analytically in special cases, e.g. for an infinitesimal dipole [Jackson, 2006], else numerical simulations have to be consulted [Lampe et al., 2003]. By determining the electromagnetic field, the actual geometry and the resistance at the antenna body directly influence the following properties.

Figure 3.2: \vec{E} -plane field patterns of three different antenna types radiating in air [Millard et al., 2002]: (i) A short dipole which is small compared to the wavelength, (ii) a bow-tie antenna, and (iii) a dipole having the same length as the largest extent of the bow-tie. The given angle corresponds to the angle between \vec{E} and the antenna's long axis. The crossing point between the dipole results and the straight line, which extends from the circle's center and to its borders, gives the normalized field strength.



Radiation Pattern The antenna's field or power pattern is defined as the dependency of \vec{E} , \vec{B} , or the Poynting vector

$$\vec{s} = \frac{1}{\mu_0} (\vec{E} \times \vec{B}) \quad (3.24)$$

on spherical coordinates. Since these quantities are in general complex, the real counterparts are often considered instead. The usage of a real valued power pattern also has the advantages that (i) its temporal mean can be investigated as well and (ii) the sphere surface integral provides, by definition, the totally radiated power. To provide intuitive access, radiation patterns are often visualized (e.g. figure 3.2) in the \vec{E} - and \vec{B} -plane, which are defined as the planes containing the respective field vector and the poynting vector.

Bandwidth and Frequency Spectrum The frequency composition of the emitted electric field is modified compared to that of the excitation voltage by (i) the antenna geometry, (ii) by the time-derivative of $\vec{j}(\vec{x}, t)$ in equation (3.11), and (iii) the electromagnetic properties in the close surrounding of the antenna (section 3.4.2). The resulting antenna-specific spectrum determines the bandwidth at which the antenna operates.

Polarization The electromagnetic field which is radiated by an antenna is polarized and the polarization is in general depending on the distance to the antenna (e.g. in the near-field region) and on the angle of observation. Some antennas (e.g. dipole or bow-tie antennas) have an effective linear polarization in the far-field, which is parallel to the antennas' main axis. This is an advantage for the detection of objects, which have a dominant spatial extent (e.g. pipes or cables), by their reflection signal.

An useful property of an antenna is inherently determined by the reciprocity theorem (e.g. [Balanis \[1997\]](#)). This theorem states that for two identical antennas, which are used as transmitter and receiver, the received signal is identical if the roles and positions of the antennas are interchanged. Additionally, it follows from the theorem that the transmitting pattern of an antenna is equal to its the receiving pattern.

3.4.1 Near and Far-Field

The space around an antenna is subdivided in three zones, as indicated in figure 3.4. This distinction can be understood by assuming an electrical dipole, which is excited with a time-harmonic charge current density with the frequency ω resulting in the dipole moment $\vec{\Psi}$. Solving Maxwell's equations using a first order approximation, [Jackson \[2006\]](#) finds the resulting electromagnetic fields for the dipole centered at the origin and surrounded by a homogeneous medium with $\mu = \mu_0$ and $c = c_0/\sqrt{\epsilon_r}$ as

$$\vec{B}(\vec{x}) = \frac{\mu_0 \omega^2}{4\pi c} (\vec{n} \times \vec{\Psi}) e^{irk} \left(\frac{1}{r} + \frac{i}{kr^2} \right) \quad (3.25)$$

and

$$\vec{E}(\vec{x}) = \frac{1}{4\pi\epsilon} \left[k^2 (\vec{n} \times \vec{\Psi}) \times \vec{n} \frac{e^{irk}}{r} + 3[3\vec{n}(\vec{n}\vec{\Psi}) - \vec{\Psi}] \left(\frac{1}{r^3} - \frac{ik}{r^2} \right) e^{irk} \right] \quad (3.26)$$

with $r = |\vec{x}|$ and $\vec{n} = \vec{x}/|\vec{x}|$.

Reactive Near-Field This region can be defined as the area where $kr \ll 1$, what makes the terms $\vec{B} \propto 1/r^2$ and $\vec{E} \propto 1/r^3$ dominate in (3.25) and (3.26), respectively. For most antennas with a maximal extent D , [Balanis \[1997\]](#) estimates the reactive near-field zone to be given for $r < 0.62\sqrt{D^3/\lambda}$. For a dipole with $D \ll \lambda$, the author finds $r < \lambda/2\pi$. In this case, the power density in the reactive near-field zone can be computed and is a complex quantity. The imaginary part of that power density is termed

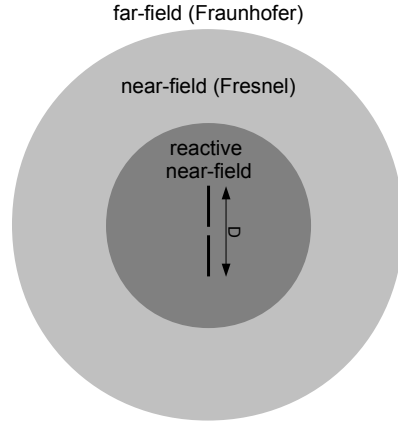
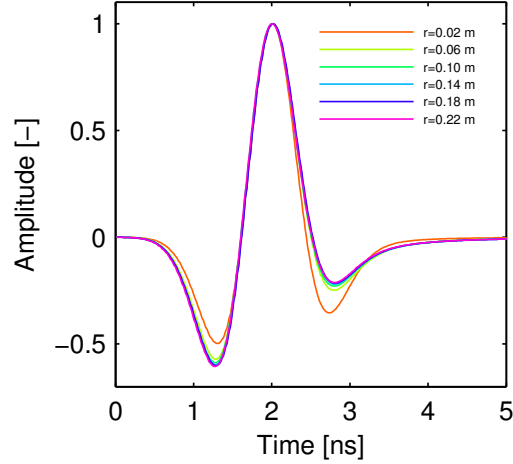


Figure 3.3: Field zones around an exemplary dipole antenna (black line).

the reactive power density. In general, however, the prediction of the electromagnetic field in the reactive near-field can be infeasible and the relation between \vec{E} and \vec{B} is complicated. Observations (section 3.4.2) suggest that the presence of spatially variable electromagnetic properties in the reactive near field zone can have a significant impact on the resulting electromagnetic field.

Figure 3.4: \vec{E}_z parallel to the emitting dipole, for different distances ' r '. The infinitely long dipole is embedded in a homogeneous medium with $\varepsilon_r = 5$ and emits a Ricker wavelet (section A.2) with a nominal frequency of 400 MHz. The signals are normalized and temporally referenced to their maximum amplitude. The results were obtained with 2D FDTD computations.



Near-Field The region between the reactive near-field and the far-field is defined as the near-field or Fresnel zone. In this zone $kr > 1$ shall hold and the terms $\vec{B} \propto 1/r$ and $\vec{E} \propto 1/r^2$ dominate in (3.25) and (3.26), although the other terms are significant either. Hence, the angular field distribution is dependent on r , a finding which is used for alternative definitions of the near-field zone. As depicted in figure 3.4, however, also the shape of an emitted signal is dependent on r . As an upper limit of the near field region, *Balanis* [1997] gives $r \approx 2D^2/\lambda$. If other antennas are placed in the near-field region, they can act as subsequent emitters as well as relevant energy sinks. The electromagnetic near-field can be calculated (e.g. *Sendur and Challener* [2003], *Streich and van der Kruk* [2007], *Warren and Giannopoulos* [2012]), is measurable [*Yaghjian*, 1986], and the far-field can be calculated on that basis, which is the purpose of near-field radiation pattern measurements.

Far-Field This zone (also called the Fraunhofer-zone) is defined as the region where the angular field distribution is independent of r and where the radiative terms ($\propto 1/r$) in (3.25) and (3.26) are large compared to the other terms. Inserting this into (3.24) one finds that the radiated power density decays $\propto 1/r^2$. This is also dictated by energy conservation since the totally radiated energy, obtained by integrating over a spherical surface which increases $\propto r^2$, must not change with r . The electromagnetic far-field can be computed for many systems and the complete antenna system together with the distribution of electromagnetic parameters can be represented by transmission-line models (e.g. *Lambot et al.* [2004b]), i.e., by Greens' functions. Antenna coupling effects can be neglected in the far-field zone and with that other antennas can be used to measure the antenna's radiation pattern independently.

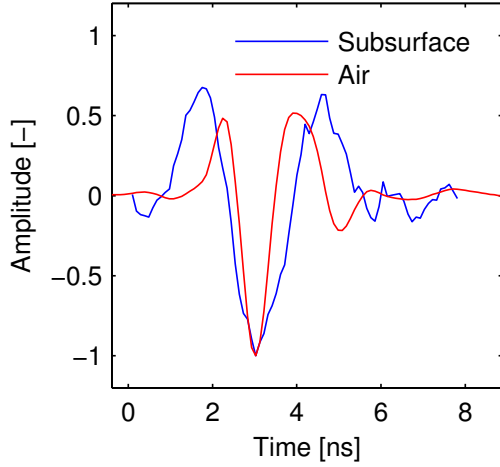


Figure 3.5: Signals recorded between two shielded bistatic GPR antenna pairs (Ingegneria dei Sistemi S.p.A.) with a nominal frequency of 400 MHz and a transmitter-receiver separation of 1.67 m, operated in transverse electric mode. The air signal was obtained while tilting the antenna boxes by 90° around their long axis. The subsurface signal was recorded with the antennas mounted on-ground and stems from a reflecting layer interface at ca. 0.86 m depth in an unsaturated sandy soil at about 22 % volumetric water content.

3.4.2 Ground Coupling

Surface- and borehole-GPR antennas are deployed directly at the ground surface or in boreholes. That is, in both cases the electromagnetic properties in the reactive near-field region of the antenna possibly change with varying positions. The involved implications have been studied by various authors, leading to the following results for surface GPR systems:

- If an antenna is placed at the interface between vacuum and a half space with the dielectric permittivity ε_r , its radiation pattern gets more narrow with increasing ε_r [Millard et al., 2002, Diamanti et al., 2012].
- Numerical simulations show that the radiation pattern is also depending on the distance at which an antenna is placed above a lossless dielectric half-space [Diamanti et al., 2012, Warren and Giannopoulos, 2012]. The authors find a decrease of the energy radiated into the half-space with the antenna height. This finding is relevant, since the antennas in real GPR system are also not placed directly at the ground surface, but with a small distance. This distance is caused by the embedding dielectric medium (figure 4.1), the antenna box, and possibly by air gaps in case of an uneven surface.
- Millard et al. [2002] report a down-shift of the center frequency from nominal 900 MHz and 1 GHz antennas to 500 MHz and 666 MHz, respectively, when the corresponding antennas were deployed on concrete. A similar result is also found for the signal shown in figure 3.5 where the center frequencies are found to be 500 MHz and 320 MHz for the air and subsurface signal, respectively. This is also expressed in the change of the wavelets' shapes, where the dominant period of the subsurface signal is significantly larger than the one of the air signal.
- By the reciprocity theorem, both transmitter and receiver antenna are effected.

The above effects have the consequence that the ground-coupling or, more precise, the antenna efficiency, i.e., the ratio between the input energy and the radiated energy, might be insufficient for survey purposes. Manufacturers address this problem by (i) shielding the antenna (figure 4.1) towards air to increase the power radiated into the subsurface (as demonstrated for instance by [Diamanti et al. \[2012\]](#)) and (ii) by embedding the antennas into a dielectric medium which matches the dielectric permittivity of the subsurface optimally. If the antenna system is operated off-ground (e.g. [Lambot et al. \[2004b\]](#)) with the subsurface located in the far-field zone of the antenna, the complete system can be described as a linear system. This is not feasible in case of borehole or surface GPR systems. Thus, different strategies have to be followed to simulate GPR measurements with still assuming a point dipole in the context of quantitative inversion of GPR signals: (i) the antenna is represented effectively by estimating a source-current function which includes all coupling effects [[Ernst et al., 2007a](#), [Busch et al., 2011](#)] or (ii) by referring to a reflection obtained from a point in the subsurface which can be assumed to be in the near- or far-field [[Buchner et al., 2012](#)].

3.4.3 Radiation at a Dielectric Interface

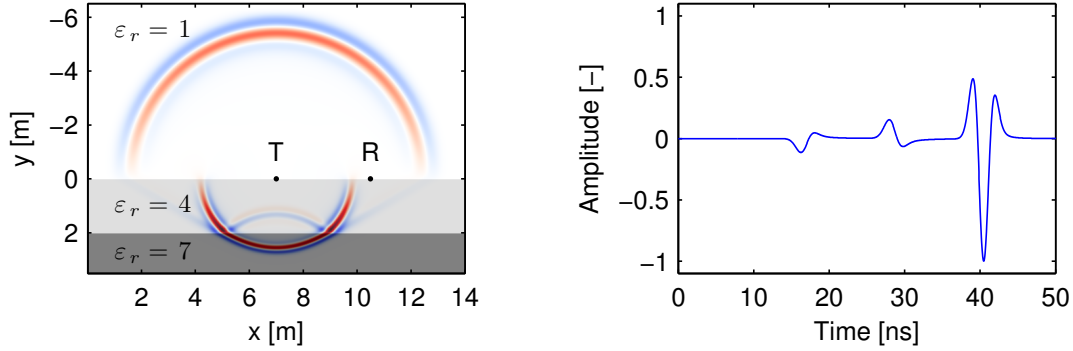
If an antenna radiates an electromagnetic field at the interface between two lossless media with different ε_r , the resulting electric field has characteristic features which were studied by various authors before (e.g. [Ott \[1942\]](#), [Annan \[1973\]](#), [Dai and Young \[1997\]](#)). These features have significant implications for the evaluation of GPR measurements.

Figure 3.6 shows the results for an electromagnetic pulse emitted by a dipole located at an interface between two media with different ε_r . The region above the interface represents air, while the region below shall represent the subsurface or ground. Although the results were obtained with a two-dimensional simulation, they do qualitatively also apply for the same situation in three dimensions.

In the field distribution in graph (a) three circular waves are present: (i) One traveling in air, which is called the direct airwave when it is observed at the air-ground interface. (ii) The signal propagating in the middle layer and its transmitted part entering the lower layer. (At the air-ground interface, the further is also denoted as the direct groundwave.) (iii) Its reflected part traveling upwards in the middle layer being phase-flipped because of the dielectric contrast at the lower interface.

In addition, two other wave phenomena are present. First, from the location where the circular wave in air reaches the air-ground interface towards the circular wave in the ground, the so-called head- or flank-wave is found [[Ott, 1942](#)]. It's appearance can be understood by Huygens' principle: The circular wave in air causes subsequent circular waves to be emitted at the air-ground interface, which constructively interfere to the head-wave. The constructive interference is only possible since the propagation speed in the middle layer is smaller than the one in air; with the phenomenological analogy to bow- or shock waves observed for surface- or sonic-waves, respectively.

The second phenomenon occurs where the circular wave propagating in the middle layer reaches the air-ground interface. Here, also subsequent circular waves are induced, but since their propagation speed in air is larger than the one in the middle layer, they do not constructively interfere. Hence the resulting electric field decays rapidly.



(a) \vec{E}_z after 23 ns stemming from a 400 MHz Ricker pulse (colored), which was emitted from an infinite dipole pointing in z -direction. It is located at position 'T' at the interface of media with different ε_r (grey).

(b) Normalized \vec{E}_z recorded at position 'R' in graph (a). The three different wavelets stem from the direct airwave (first), from the direct groundwave (second), and from the reflection at the lower interface (third).

Figure 3.6: Electric field distribution and time-dependency obtained from two-dimensional numerical simulations (FDTD). The time-evolution of the electromagnetic field distribution is provided by the movie [boundary_radiation.mp4](#).

Graph (b) in figure 3.6 shows the time evolution of the \vec{E}_z recorded at 'T' where three distinct wavelets can be found. The first two correspond to the direct air- and groundwave, while the third one stems from the reflection at lower interface. The shapes of the first two wavelets are noticeably different from the third. [Dai and Young \[1997\]](#) derived that the time-dependency of direct signals observed at the upper interface is proportional to the time-dependency of the charge current density. This is not the case if the dipole antenna is placed above the interface or in a completely homogenous medium (e.g. equation (3.33)). However, not only the shape of the two direct wave signals is different, also their amplitude is significantly lower compared to the third signal; although the latter is a reflected signal. This is explained by [Sommerfeld \[1909\]](#) and [Annan \[1973\]](#) who show that the fields directly at the interface decay $\propto 1/r^2$ in comparison to the circular waves which decay $\propto 1/r$ far from the interface; dictated by energy conservation. From graph (a) one can also observe that the circular waves decay towards the interface and the shape transition from three extrema to two extrema is continuous. [Ott \[1942\]](#) shows that this effect results from the superposition of an initial circular wave with the reflection of the same at the interface. If the dipole antenna is located directly at the interface, the two waves are in-phase everywhere and interfere with the given result. However, if the source is not located at the interface or the circular wave is for instance induced by a reflection (as can be found in the movie [boundary_radiation.mp4](#)), the same effect is present for large distance from the point of initial occurrence.

As a concluding remark, it should be mentioned that these effects are not predictable with geometrical optics only, but with the inclusion of second order effects [[Annan, 1973](#)].

The wavelet shape change is of importance for the determination of signal traveltimes by “picking” individual wavelet features (section 4.4.1); e.g., extrema or zero-crossings. Analyzing the data from figure 3.6 (b) one can estimate the dielectric permittivity of the middle layer. For this the so-called time-offset (section 4.4.1) has to be determined. This is done using the apparent traveltime of the reflection wavelet and the theoretical prediction from ray-tracing. The correct traveltime of the direct groundwave, can be determined by identifying the same wavelet feature and a following time-offset correction. Using this traveltime and assuming a direct travelpath, ε_r of the middle layer is retrieved. Following this procedure by picking the first maximum of the wavelets, leads to a deviation of about 8 % for the determined ε_r . In contrast, using the “center of intensity” method, proposed in this study (section 5.3), this deviation can be reduced to 2 % in the given case and theoretically to zero if the absolute values of the observed wavelets are symmetric to time reversal.

3.4.4 2D and 3D solutions

Although two-dimensional and three-dimensional solutions to Maxwell’s equations provide conceptually similar results under certain symmetry assumptions, there are significant quantitative differences in special cases. Since these are relevant when investigating an infinite dipole radiating in a homogenous medium, this setup is studied in the following.

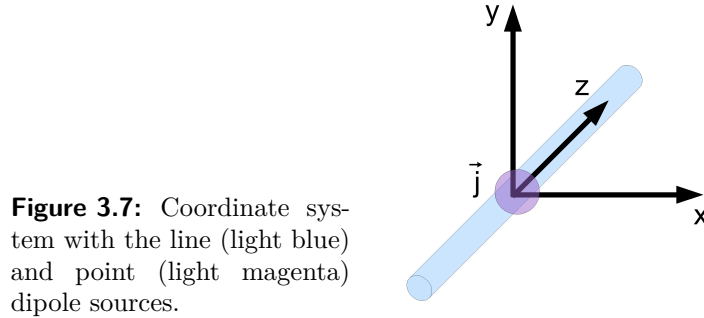


Figure 3.7: Coordinate system with the line (light blue) and point (light magenta) dipole sources.

The electromagnetic fields can be determined from the vector potential \vec{F} under the assumption $\rho = 0$ as

$$\vec{B} = \nabla \times \vec{F} \quad \wedge \quad \vec{E} = -\frac{\partial \vec{F}}{\partial t}. \quad (3.27)$$

The vector potential at location \vec{r} and time t is related to \vec{j} by [Jackson, 2006]

$$\vec{F}(\vec{r}, t) = \frac{\mu_0}{4\pi} \int dV' \frac{\vec{j}(\vec{r}', t - \frac{|\vec{r} - \vec{r}'|}{c})}{|\vec{r} - \vec{r}'|} \quad (3.28)$$

in a homogeneous medium with real ε_r and $c = c_0/\sqrt{\varepsilon_r}$. In the above equation the term $\frac{|\vec{r} - \vec{r}'|}{c}$ expresses the retardation, i.e., the time-shift dictated by causality. To derive a factor relating the solution of a 3D problem with the one of a 2D problem, two sources are assumed (figure 3.7): (i) a point dipole source of infinitesimal extent and (ii) a

line dipole source which extends infinitely in z-direction. Without loss of generality the dipoles are assumed to be centered at the origin and the source current density is given by

$$\vec{j}(\vec{r}, t) = j_0 \delta(x) \delta(y) s(t) f(z) \vec{e}_z \quad (3.29)$$

with $s(t)$ and $f(z)$ denoting general time and z-dependencies. Now, (3.28) translates to

$$\vec{F}(\vec{r}, t) = \frac{\mu_0}{4\pi} \int_{-\infty}^{\infty} dx' \int_{-\infty}^{\infty} dy' \int_{-\infty}^{\infty} dz' \frac{j_0 \delta(x') \delta(y') s(t - \frac{|\vec{r} - \vec{r}'|}{c}) f(z')}{|\vec{r} - \vec{r}'|} \vec{e}_z \quad (3.30)$$

$$= \frac{j_0 \mu_0}{4\pi} \int_{-\infty}^{\infty} dz' \frac{s(t - \sqrt{x^2 + y^2 + (z - z')^2}/c) f(z')}{\sqrt{x^2 + y^2 + (z - z')^2}} \vec{e}_z. \quad (3.31)$$

For the purpose of transforming a 2D to a 3D solution in section 5, it suffices to set $z = 0$. Additionally, without the loss of generality $y = 0$ can be assumed and one finds

$$\vec{F}(\vec{r}, t) = \frac{j_0 \mu_0}{4\pi} \int_{-\infty}^{\infty} dz' \frac{s(t - \sqrt{x^2 + z'^2}/c) f(z')}{\sqrt{x^2 + z'^2}} \vec{e}_z. \quad (3.32)$$

Inserting (3.32) into (3.27) it follows

$$\vec{E}(\vec{r}, t) = -\frac{j_0 \mu_0}{4\pi} \int_{-\infty}^{\infty} dz' \frac{\frac{\partial}{\partial t} s(t - \sqrt{x^2 + z'^2}/c) f(z')}{\sqrt{x^2 + z'^2}} \vec{e}_z. \quad (3.33)$$

In the case of the point source obviously $f(z) = \delta(z)$. Assuming additionally $s(t) = e^{i\omega t}$, equation (3.33) gives the expected monochromatic circular wave solution

$$\vec{E}(\vec{r}, t) = -\frac{i\omega j_0 \mu_0}{4\pi x} e^{i(\omega t - kx)} \vec{e}_z. \quad (3.34)$$

In contrast, for a line source with a homogenous source current density $f(z) = 1$, the following expression is found:

$$\vec{E}(\vec{r}, t) = -\frac{j_0 \mu_0}{4\pi} \int_{-\infty}^{\infty} dz' \frac{\frac{\partial}{\partial t} s(t - \sqrt{x^2 + z'^2}/c)}{\sqrt{x^2 + z'^2}} \vec{e}_z. \quad (3.35)$$

This expression corresponds to the intuitive understanding of circular waves which are emitted in-phase along the line source: at location \vec{r} these are summed up weighted with a factor which is proportional to the distance to the emission point and the location of interest, i.e., the amplitude decrease in (3.34). In addition, there is a time-shift for each contribution, which corresponds to the time the contribution takes to propagate to \vec{r} .

Inserting $s(t) = e^{i\omega t}$ and exploiting the symmetry in z-direction finally leads to the expression

$$\vec{E}(\vec{r}, t) = -\frac{2i\omega j_0 \mu_0}{4\pi} \int_0^{\infty} dz' \frac{e^{i\omega t - i\frac{\omega}{c}\sqrt{x^2 + z'^2}}}{\sqrt{x^2 + z'^2}} \vec{e}_z = -\frac{i\omega j_0 \mu_0 e^{i\omega t}}{2\pi} \int_0^{\infty} dz' \frac{e^{-i\frac{\omega}{c}\sqrt{x^2 + z'^2}}}{\sqrt{x^2 + z'^2}} \vec{e}_z. \quad (3.36)$$

This integral does not appear to be solvable with commonly available computer algebra system, but can still be analyzed to some degree. It is apparent, that the integral is frequency dependent in the sense that the argument of the exponential function is scaled with the wavelength. However, to derive an expression which is able to transform from two to three dimension this is inappropriate. Shifting the factor ω/c into the roots, substituting $b = \omega z/c$, and introducing $R = \omega x/c$ equation (3.36) changes to

$$\vec{E}(\vec{r}, t) = -\frac{i\omega j_0 \mu_0 e^{i\omega t}}{2\pi} \int_0^\infty db' \frac{e^{-i\sqrt{R^2+b'^2}}}{\sqrt{R^2+b'^2}} \vec{e}_z. \quad (3.37)$$

Now, the integral gives numerically equal results for all frequencies with the scaled length R , i.e., when the coordinates are measured as multiples of wavelengths. Three important facts can be derived for this integral. (i) Any physically meaningful solution will be finite, hence the expression must converge to a constant for the upper limit of the integration. Because of energy conservation this constant is necessarily zero. (ii) The exponential function will stay in that form also in the integrated expression and the evaluation at $b = 0$ leads to a factor e^{-iR} . (iii) Due to the cylindrical symmetry of the problem, the field must decay as $1/\sqrt{R}$ to fulfill energy conservation. Hence the resulting expression will be $\propto e^{-iR}/\sqrt{R} = e^{-i\omega x/c}/\sqrt{\omega x/c} = e^{-ikx}/\sqrt{\omega x/c}$. Inserting this into (3.37) and comparing to the 3D solution (3.34) leads to the result: For the 2D solution to be equal to the 3D solution it has to be multiplied with a factor, whose dominant term is $\sqrt{\frac{\omega\sqrt{\epsilon_r}}{c_0 x}}$. This is identical, except of some constant factors, to the conversion obtained by [Bleistein \[1986\]](#) for the far-field in the frequency-domain where

$$\hat{E}_{3D} = \hat{E}_{2D} \frac{e^{-\frac{i\pi}{4}\text{sign}(\omega)}}{\sqrt{2\pi}} \sqrt{\frac{|\omega|\sqrt{\epsilon_r}}{c_0 x}}. \quad (3.38)$$

In the frequency domain negative frequencies have to be considered and thus the absolute value and the signum function are employed. An example to the correct work of the transformation is illustrated in figure 3.8, where the slight differences between the 3D and 2D-3D curves are due to numerical errors.

The above derivation was performed for a homogenous medium without the presence of an interface at the source location. [Bleistein \[1986\]](#), however, drops these assumptions and derives that transformation (3.38) can be applied to reflections stemming from the subsurface. Additionally, one can show with a calculation similar to the one obtained for figure 3.8, that the transformation also holds for direct groundwave signals (defined in section 3.4.3).

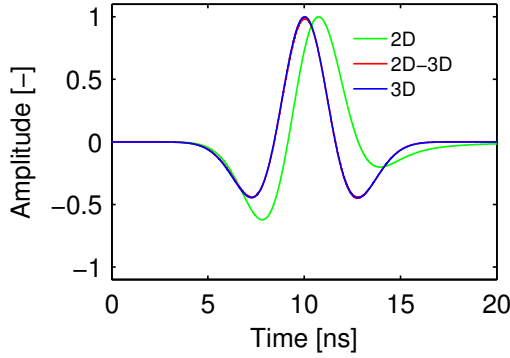


Figure 3.8: Comparison of normalized \vec{E}_z observed 6 m from a dipole source embedded in a homogeneous medium with $\varepsilon_r = 4$ excited with a Ricker source current charge density with a nominal frequency of 100 MHz. The 2D solution is obtained via FDTD, the 3D solution is computed via (3.33), and the 2D-3D curve is computed from the 2D solution employing the transformation (3.38).

3.5 Reflections

Maxwell's equations determine that reflections of electromagnetic waves occur at spatial changes of the electromagnetic properties. Hence, this is not only the case at interfaces but also for continuous changes of the properties. However, at an interface between two regions with homogenous dielectric properties, all frequency components of a signal are equally reflected. In contrast, the signal which is reflected from a continuous change has a different frequency spectrum than the incoming signal. The reason for this is the following: The incoming signal gets reflected at each position along the continuously changing material. Thus, the signal observed in direction of incoming signal is the superposition of all the corresponding retarded reflections. Whether the different frequency components interfere constructively or destructively depends on their phase-shift, which is determined by their time-shift measured in period-lengths. Hence, for a continuous change of the dielectric properties over a certain extent, frequency components with a period length, which is much longer than the maximal traveltime of a reflected signal, will constructively interfere. Consequently, the reflection response for this frequency component will be almost similar to the one from a clear interface. In contrast, for the frequency components with a period length, which is much smaller than the maximum traveltime, the situation is different: For a reflection stemming from one point, there will be most likely a reflection with a π phase shift from another position which interferes destructively. Hence, this frequency component contributes with smaller amplitude in the reflected signal.

An example to this effect is given in figure 3.9, where various signals are compared, which are reflected at different permittivity profiles. The signals are reflected from an interface located at x_0 between two homogeneous regions with $\varepsilon_{r,1}$ and $\varepsilon_{r,2}$. The permittivity distribution in the vicinity of the interface is smoothed with the function

$$f(x) := \begin{cases} \varepsilon_{r,1} & \text{if } x - x_0 < -\zeta \\ \varepsilon_{r,1} + \frac{\varepsilon_{r,2} - \varepsilon_{r,1}}{2} \left[\frac{x - x_0}{\zeta} + \frac{1}{\pi} \sin\left(\pi \frac{x - x_0}{\zeta}\right) + 1 \right] & \text{if } |x - x_0| \leq \zeta \\ \varepsilon_{r,2} & \text{if } x - x_0 > \zeta, \end{cases} \quad (3.39)$$

where ζ is the smoothing width. The results show a clear change in the shape of the re-

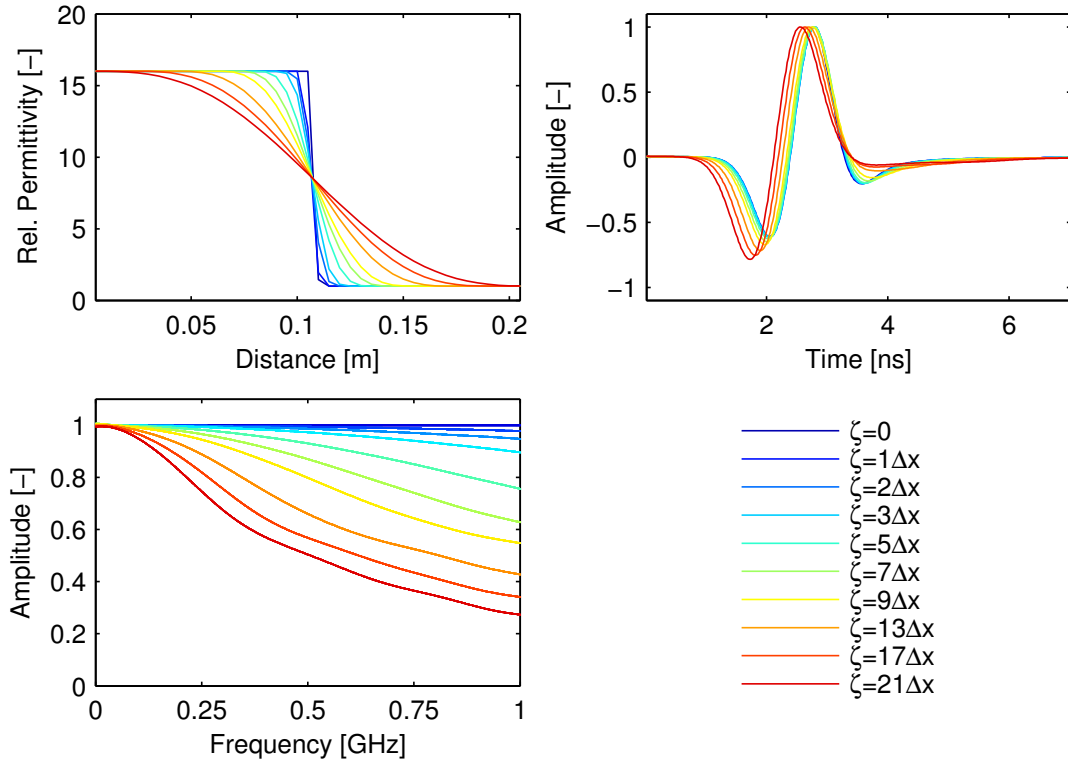


Figure 3.9: Permittivity profiles (upper left) of an interface at $x_0 = 0.1075$ m smoothed by function (3.39) with the width ζ . An infinite dipole is placed 2 m from x_0 and excited with a Ricker source current density with a nominal frequency of 400 MHz. Next to the dipole, the reflected \vec{E}_z (upper right) is observed. The results are obtained by FDTD simulations in 2D with a spatial resolution $\Delta x = 5$ mm. Thus, the discrete permittivity distribution is visible in the permittivity profiles. For $\zeta = 0$, the profile is also not exactly a step function due to the subpixel smoothing (section 3.3.3.1) employed by MEEP. The lower left graph shows the one sided amplitude spectrum of \vec{E}_z divided by the spectrum of \vec{E}_z obtained with $\zeta = 0$.

flected wavelets which is best understood in the frequency domain: In agreement with the above explanation, one finds a monotonic decrease of amplitude with increasing frequency. In addition, the amplitude depends on ζ . However, we only find a minimal impact when comparing the result for $\zeta = 0$ and $\zeta = 1\Delta x$, which is relevant in section 5.2.

Detailed investigations, on how a reflected wavelet is effected by the so-called capillary fringe and what can be determined from these reflections about the shape of the capillary fringe, were carried out by [Dagenbach \[2012\]](#).

3.6 Petrophysical Relationships

Many hydrogeophysical measurement methods which utilize electromagnetic signals to investigate the subsurface, do rather provide information on the electromagnetic para-

meters ε'_r and σ , than on hydrological quantities, such as porosity ϕ or the volumetric water content θ . Thus, petrophysical relationships linking the two classes of parameters are employed.

In an early work, [Archie \[1942\]](#) related the resistivity $1/\sigma$ with ϕ and θ to improve the evaluation of electric resistivity logs for reservoir characterization. However, for other measurement methods which provide ε'_r , the exploitation of the latter is of more interest. This brings up the question how the effective or composite permittivity $\varepsilon'_{r,c}$ of a mixture of phases is related to the permittivities of the individual phases. There are three different approaches to address this issue [[Brovelli and Cassiani, 2008](#)]: (i) Effective medium or mean-field theories, (ii) mixing rules (e.g. [Tinga et al. \[1973\]](#)), and (iii) empirical relationships (e.g. [Topp et al. \[1980\]](#)). While the last approach is in general restricted to a certain type of media and needs on-site calibration, the first is physically based but makes strong assumptions on the geometry of the individual phases. Hence, the second approach is favored since it is physically based and flexible. One type of dielectric mixing formula is given by the Lichtenecker-Rother [[Guéguen and Palciauskas, 1994](#)] equation as

$$\varepsilon'^{\alpha}_{r,c} = \sum_{j=1}^n \Phi_j \varepsilon'^{\alpha}_{r,j}. \quad (3.40)$$

Here, n is the number of phases, Φ_j is the volume fraction of phase 'j' and α is a fitting parameter. In fact, (3.40) also holds for the general dielectric permittivity $\varepsilon_{r,g}$ and electric conductivity can be included, but this is not common practice. The exponent α depends on the phase geometry and ranges from -1 to 1. For a mixture of soil matrix, air, and water, [Roth et al. \[1990\]](#) found $\alpha = 0.46$ to be valid for different volume fractions and soil types. For the same case but assuming $\alpha = 0.5$ equation (3.40) leads to the so-called complex refractive index model given by

$$\sqrt{\varepsilon'_{r,c}} = (1 - \phi) \sqrt{\varepsilon'_{r,s}} + \theta \sqrt{\varepsilon'_{r,w}} + (\phi - \theta) \sqrt{\varepsilon'_{r,a}}, \quad (3.41)$$

where $\varepsilon'_{r,s}$, $\varepsilon'_{r,w}$, and $\varepsilon'_{r,a}$ are the permittivity of the soil matrix, water, and air, respectively. Equation (3.41) refers to the most intuitive case of dielectric mixing, where the effective electromagnetic wave velocity is given as the average velocity of all phases weighted by their volume fractions.

[Brovelli and Cassiani \[2008\]](#) show that dielectric mixing models are restricted by a potential correlation of α with ϕ and $\varepsilon'_{r,s}$, which limits the determination of α by calibration measurements. However, [Brovelli and Cassiani \[2010\]](#) resolve this issue by introducing an additional parameter. This is possible by utilizing a generalized formulation which includes ε'_r and σ based on (3.40) and the findings of [Archie \[1942\]](#).

To summarize, depending on the demanded accuracy a material specific calibration is necessary. This is especially relevant if water content observed with different methods are compared. However, the water content values presented in this study are all obtained with electromagnetic methods and thus equation (3.41) is employed, since sufficient for this purpose. Please also note, that the above findings are in general frequency dependent, although this is treated as discussed in section (3.2.2).

4 Ground Penetrating Radar

A generic definition of GPR system is “a radar device which is applied to investigate the subsurface”. A radar device consists of a transmitter- and receiver antenna, which can be the same, and a control unit. Electromagnetic waves are emitted by the transmitter antenna, penetrate the ground, propagate in it, and are reflected. The resulting signal is recorded by the receiver antenna. The propagation and reflection of the waves are accompanied with a modification of the initial signal with respect to traveltime and amplitude. The modification is in general frequency dependent which implies also changes of the frequency composition of multi-chromatic signals in terms of phasing and relative amplitude. Reasons for the modifications are given by the spatial distribution of the electromagnetic parameters. These determine the phase traveltime and amplitude decay (section 3.2.2) on various travelpaths (section 3.4.3) and if reflections occur (section 3.5).

In all GPR applications, the signal modifications are employed to deduce information about the subsurface setting. For instance, engineering applications are aiming for the detection of mines, cracks in bentonite, or pipes. Additionally, GPR is also applied in forensic or archeological investigations to identify buried objects or bodies. The imaging of the geological setting of the shallow subsurface, i.e., its stratification and water content distribution are typical measurement purposes in the field of hydrogeophysics; which is also the context of the given study. In the following section, corresponding modes of operation and measurement setups are introduced. Afterwards, the technical and physical limitations and error sources are discussed. The discussion is followed by an overview of various evaluation techniques.

4.1 Modes of Operation

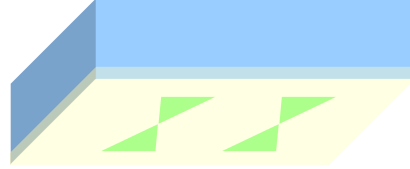
The majority of GPR applications operates in the time-domain by emitting a temporally limited electromagnetic pulse, described by a wavelet, into the subsurface. The time evolution of the signal which arrives at the receiver antenna is recorded with a constant temporal discretization and is commonly called a “trace”. Alternatively, stepped-frequency continuous-wave radar devices (e.g. [Lambot et al. \[2004a\]](#)) allow frequency-domain observations.

In addition to imaging, time-domain measurements, employing linear-dipole GPR antennas in one or more boreholes, offer the possibility to apply tomographic [[Slob et al., 2010](#)] and full waveform inversion techniques (e.g. [Ernst et al. \[2007a\]](#)). By this, the two-dimensional distribution of subsurface electromagnetic parameters can be retrieved with high resolution and to a depth which is mainly limited by drilling technology. However, the major drawbacks of borehole applications are (i) the high

financial effort which is involved, (ii) the limitation by localization, and (iii) that the method is invasive.

Surface GPR investigations can either be carried out on-ground or off-ground. While the latter has the advantage of being a far-field application, it is also accompanied by a reduction of radiation power in the subsurface. Different antenna designs are applicable, among these most prominently horn antennas and bow-tie antennas.

Figure 4.1: Sketch of a shielded (blue) bistatic GPR antenna with two bow-tie elements (green) which are embedded in a dielectric (yellow).



The antennas which were employed in this study are shielded bistatic antennas (figure 4.1). The two bow-tie elements, acting as transmitter and receiver, are embedded in a dielectric to improve ground-coupling (section 3.4.2) and are shielded to enhance the antenna's directivity. The given antenna system is applied with the lower side parallel to the surface. When a multichannel system, consisting of multiple bistatic antennas, is used the bow-tie elements can be orientated to each other in two fundamental modes: (i) The transverse electric (TE) mode: The bow-tie elements are aligned next to each other with parallel long axis. (ii) The transverse magnetic (TM) mode: Again the long axis of the bow-ties are parallel, but the elements are aligned behind each other in direction of the long axis.

4.2 Measurement Setups

Several standard measurement setups for surface GPR surveys exist, while the choice of the appropriate setup is a balancing of measurement effort and measurement purpose [Maurer et al., 2010]. The former is especially relevant in large scale surveys (e.g. Pan et al. [2012]), where a dynamical process is observed and thus limited time is available or a high spatial resolution is required. Since this problem can be addressed by parallelization of the measurement process, the limiting factor concerning the measurement effort is essentially a financial one.

Wide Angle Reflection and Refraction – WARR

The setup for this measurement is depicted in figure 4.2. Independent of the actual antenna types, a transmitter (T) is placed at a fixed position, while a receiver (R) is incrementally displaced 'n' times, typically by a fixed distance. Alternatively, an array of receivers can be employed. For each offset or transmitter-receiver separation 'a', a trace is recorded.

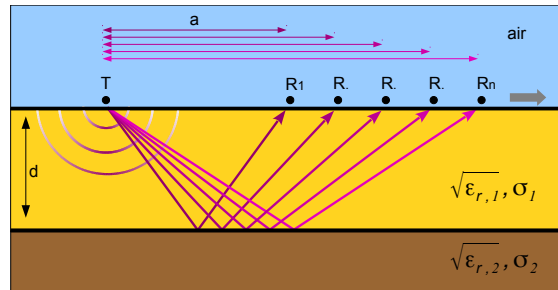


Figure 4.2: Conceptual sketch of WARR measurement.

This setup is especially suited for the observation of reflections from layer interfaces, indicated in the graph by the corresponding shortest raypaths. To relate the traveltime t with first order accuracy to $\varepsilon_{r,1}$ and depth d , one can assume that (i) the electromagnetic properties are locally homogenous, (ii) the approximation for electromagnetic wave velocity $c = c_0/\sqrt{\varepsilon_{r,1}}$ holds, and (iii) the observed interface is horizontal, and placed at depth d . Then t of the reflection signal is given by the hyperbola

$$t = \frac{2\sqrt{\varepsilon_{r,1}}}{c_0} \sqrt{\left(\frac{a}{2}\right)^2 + d^2}. \quad (4.1)$$

This offers the possibility to determine the two unknowns in equation (4.1) by fitting the hyperbola to the reflections' traveltime or by cross-correlation velocity analysis (e.g. described by [Yilmaz \[2001\]](#) for the analogue seismic case). In the more complicated case of a dipping but flat interface, (4.1) is extended by higher order terms. The equation also expresses that a simultaneous determination of subsurface dielectric permittivity and layer interface position, from traveltime of reflections, is only possible if independent information stemming from different travelpaths is available. Please note that due to the fact that actually a spherical wave is emitted from the transmitter antenna also other signal components, different from the reflected wave, are obtained (section 3.4.3). These can also be exploited to retrieve independent information.

Common Midpoint – CMP Figure 4.3 shows the CMP measurement setup, which is similar to the WARR setup (figure 4.2). The major difference is that also the transmitter antenna is incrementally displaced, such that a common midpoint (P) of all transmitter-receiver positions is given. Assuming the same simplifications as for the WARR measurement above, the traveltime of the reflected wave is also given by (4.1). The most significant advantage of the CMP setup is that for the equation to hold, the reflecting interface does not necessarily need to be horizontal over a larger region: The shortest-path reflection-point, the so-called common image point, has to coincide with the horizontal position of P and the interface only needs to be locally horizontal. If the latter is not given, the reflection position changes with 'a', which can be corrected by higher order corrections [[Yilmaz, 2001](#)].

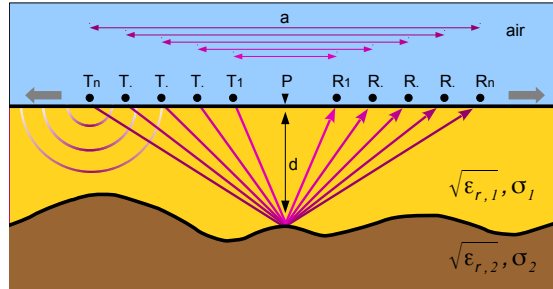


Figure 4.3: Illustration of the CMP measurement configuration.

(Multi) Common Offset – CO Especially for imaging purposes the so called common-offset setup is attractive because large areas can be covered very efficiently. In the most basic execution, a transmitter (T) and receiver antenna (R) are kept at a fix distance and moved along a measurement line to observe traces at different locations. Figure 4.5 depicts an radargram retrieved from measurements in the CO setup. The observations are only obtained with a single antenna separation. Hence, quantitative information about the sub-surface can only be retrieved from traveltimes with assumptions on the unknowns in (4.1). This problem, however, can be solved without loss in efficiency, when a multichannel GPR device is employed; i.e., a system consisting of several receiver and transmitter antennas. One implementation of such a device is shown in figure 4.4, where the system consists of two bistatic GPR antennas indicated by the white boxes. Each antenna box contains a transmitter and receiver bow-tie antenna. The boxes are also kept at a fix distance and at each measurement location, traces are recorded at the four different channels. If the transmitter and receiver antenna are in the same box, the channel is called “internal” in the following, while the other two are called “cross-box” channels. By shifting the retrieved information to the common image point, the measurement is similar to a CMP recording; potentially with a smaller amount of antenna separations but a tremendous gain of measurement efficiency. Measuring along the same measurement line, but with different separations, the number of available antenna separations can even be increased.

The datasets corresponding to this measurements setup are denoted for this thesis as multi common-offset datasets.

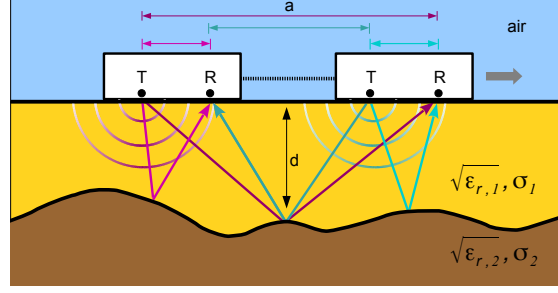


Figure 4.4: Schematic of a common-offset multichannel measurement setup in the TE mode. The raypaths of the four different channels are indicated.

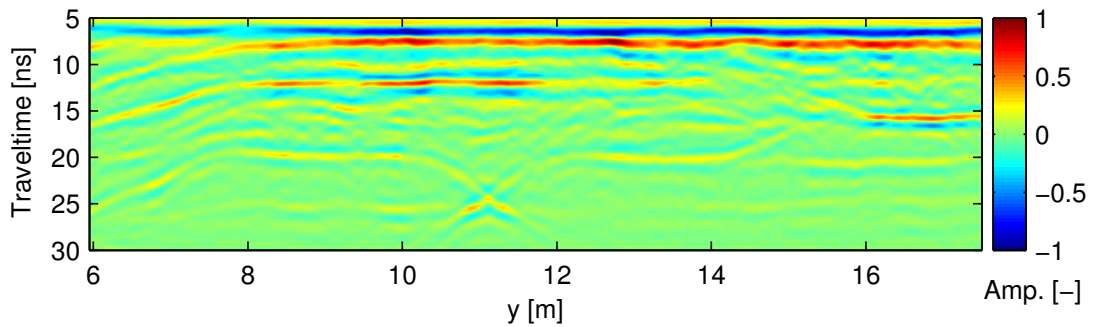


Figure 4.5: Common-offset section obtained at the ASSESS-GPR testbed (section 6.1.1) with a frequency of 400 MHz and an antenna separation of 1.08 m. The imaging-points are referenced to the testbed’s coordinate system. This “radargram” shows the signal amplitude in arbitrary units along in each trace (vertical direction) at each recording position (y-direction).

4.3 Scope of Application and Limitations

The GPR system design, the object of investigations as well as physical and information theoretical principles inherently determine a possible scope of application and certain limits of the GPR measurement technique:

Frequency Range GPR systems are designed to operate in the frequency range from about 10 MHz to 3 GHz. The bow-tie antennas employed in this work are categorized as broad-band antennas covering a bandwidth of some 100 MHz with nominal center frequencies between 200 MHz and 400 MHz. In vacuum, this corresponds to a wavelength of 1.5 m and 0.75 m, respectively. To provide a sufficient sampling density of signals in that frequency range, a temporal discretization on the order of 10^{-2} ns is required.

Antenna Dimensions To provide sensitivity at the nominal center frequency, the size of the bow-tie elements in figure 4.1 differs with frequency. In the given case the longest extent is several decimeters. The distance between the bow-tie elements is chosen on the order of few decimeters, to provide small antenna dimensions and a good directionality; while attempting to minimize antenna cross-talk.

Displacements Since surface GPR is applied in the field, the measurement setup has to be flexible enough to adapt to surface roughness. This introduces a limit to the actual measurement precision caused by displacements of the antennas, which is discussed for the CO setup: Of special importance is the rotation of individual antenna boxes along the long axis of the bow-tie elements. This causes an apparent dipping of reflecting interfaces and thus a change of the traveltime. Moreover, the image point position is changed in the radiation pattern and hence amplitude variations can occur as well. The radiation pattern can also be affected if the surface roughness is present at a scale which is smaller than the antenna box extent. Hence, air gaps beneath the antenna effect the ground coupling.

Signal Amplitude Various factors contribute to the amplitude modification of the electromagnetic pulse after it has entered the subsurface. Attenuation by dielectric and conductive losses as well as geometrical spreading were already discussed in sections 3.2.2 and 3.4.3, respectively. In addition, the radiation pattern of the transmitter and receiver antenna introduces a direction dependent change of the signal amplitude. If reflections occur at changes in the electromagnetic properties, the resulting signal amplitude is modified as well. The reflections caused by scattering at small objects, which are not of interest, is often summarized as clutter. The lower limit for the received signal amplitude is given by the instrument's signal to noise ratio. The common strategy to address this issue, however, is stacking, i.e., the averaging of multiple traces recorded at one position.

Penetration Depth With common GPR devices a penetration depth of several meters is reached for sandy soils, while it decreases for soils with much smaller grain size. As discussed in section 3.2.1, the latter is due to an increase of ε_r'' , which gets even larger with frequency. In practice, this limits the maximum frequency of time-domain GPR systems to about 1 GHz, although even higher frequencies would be desirable because of the increased resolution. A high resolution, however, also causes more energy to be reflected at small particles, which states an additional limit. In contrast, equation (3.9) shows that the influence of σ increases with ω^{-1} . Nevertheless, the lower limit to frequency (50 MHz) is rather given by the insufficient resolution.

Vertical Resolution The ability of a GPR system to resolve two vertically aligned objects with distance Δy is determined by the overlap of the reflection responses from these objects. If two signals overlap, depends on their temporal extent Δt . Because of the uncertainty-principle this is, however, rather determined by the bandwidth of a signal than by its dominant wavelength. A possibility to retrieve Δt is depicted in figure 4.6, where the envelope of the signal is calculated. The temporal extent can then be defined by the points corresponding to, for instance, half of the maximum amplitude. This choice is decided by the question if a single wavelet feature or the complete wavelet is of interest. If the two signals overlap in-between Δt , the object is defined not to be resolved. On that basis the minimum distance of two objects, i.e., the vertical resolution, under a small incident angle (measured against the vertical axis) is found as

$$\Delta y = \frac{c\Delta t}{2}, \quad (4.2)$$

where c is the mean velocity between the two objects.

Horizontal Resolution To determine the minimum distance of two point scatterers located at depth d in far field observations in the CO mode, the amplitude variation depending on the observation angle ϕ is relevant. This is dominated by the scattered power of a point scatterer. With that, Daniels [2004] finds for the horizontal resolution Δx given by the half power points

$$\Delta x = 4d\sqrt{\frac{\ln 2}{2 + \alpha d/2}} \quad (4.3)$$

where $\alpha/2$ is the damping constant introduced in (3.12).

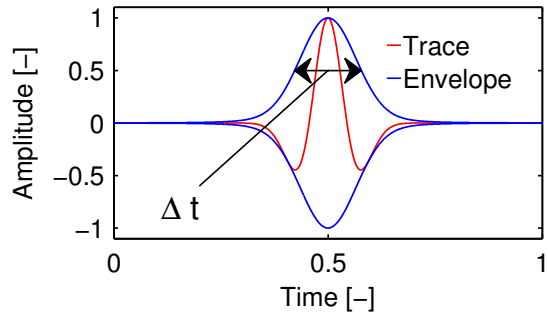


Figure 4.6: A Ricker wavelet in arbitrary units with the corresponding envelope and its temporal extent.

4.4 Evaluation Techniques

This section has the purpose to (i) give a short overview of various available evaluation techniques for the different measurement setups mentioned in section 4.2, (ii) to enable a comparison with the method described in this study, and (iii) to motivate why another evaluation technique is necessary.

The most simple technique is the conversion of traveltime to depth via (4.1) with assuming some value for ε_r . While this might be an appropriate approach for imaging purposes, it does not necessarily provide reliable quantitative information. Hence, more sophisticated techniques, as the ones introduced below, are favorable.

In the following, the retrieval of quantitative information about the subsurface has priority. Thus, standard signal processing techniques are not addressed and the reader is kindly referred to *Yilmaz* [2001] or *Daniels* [2004].

4.4.1 Traveltime and Amplitude Calculation

Although the calculation of traveltime and amplitude is not an evaluation technique by meaning, it is at the core of several approaches and thus special emphasis is given here.

Traveltime As already discussed, neither monochromatic signals nor infinitely short pulses are employed by time-domain GPR systems. Hence, the received signals are wavelets and their shapes are in general modified by the subsurface. For instance, phase changes are caused by reflections at interfaces with an increase in ε_r and dispersion might cause an elongation of the wavelet. Thus, the determination of the signal's traveltime can be carried out in different manners.

Methods which rely on the identification of specific wavelet features, like extrema, zero crossings, or the leading edge, are also associated with “picking”. While the common aspect of these is the determination of a phase traveltime, they exhibit different sensitivities to the wavelet shape changes. The leading edge is favored in the evaluation of bore-hole measurement, relying on first-arrival signals. However, the overlapping of multiple signals decreases the effectiveness of this technique. While zero-crossings are also strongly effected by interference, the usage of extrema has the disadvantage that user judgement is necessary to identify phase flips.

Cross-covariance approaches are an established alternative to picking techniques. For instance, *Peraldi and Clement* [1972], *Irving et al.* [2007], *Giroux et al.* [2009] used the cross-covariance of a signal with a reference wavelet to retrieve signal travel-times. However, this approach is very sensitive to differences between the observed signal and the reference wavelet. Hence, a more robust approach is introduced in section 5.3, which identifies the “center of intensity” of a signal: The cross-covariance is calculated using a Gaussian shaped function and the absolute value of the signal. From another point of view, this approach is the application of a Gaussian filter to the absolute value of the traces. This leads to unique maxima indicating the position of reflected signals along the traces. By a following automatic detection of these maxima, the procedure resembles the matched filter approach used for detection and ranging (e.g. *Turin* [1960]). However, the latter approach focuses on the differentiation of signal from noise while the

given method follows the premise of an unique identification of signals in the presence of several ones. Figure 4.7 gives an example to the method introduced in this study. Since the actual wavelet is symmetric, the identification point coincides with its maximum.

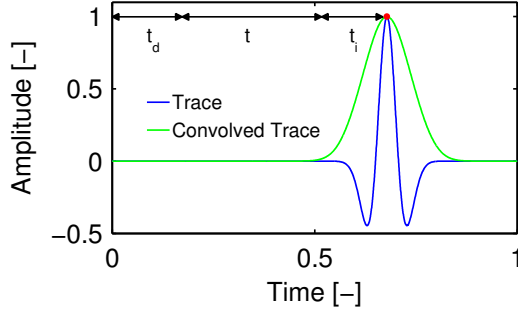


Figure 4.7: Example of a signal detection by identifying the center of intensity.

All the methods mentioned above give rise to the issue of the time-offset (t_0) determination: When a signal is identified, an apparent travelttime t_a is retrieved. However, as indicated in figure 4.7, this does not equal the actual travelttime t since a device offset t_d and an offset t_i , caused by the employed identification procedure, have to be considered. Hence the apparent travelttime is given by

$$t_a = t + \underbrace{t_d + t_i}_{=:t_0}. \quad (4.4)$$

Although t_d could be known in principle, it is not available for common GPR devices. Hence, the combined offset t_0 is determined by a measurement with known t . Since conductible on-site without additional equipment, WARR or single offset measurements of the direct wave in air are attractive for this purpose. However, this is problematic with respect to wavelet shape changes by ground coupling (section 3.4.2) and interface effects (section 3.4.3), which limit the accuracy of this approach for picking methods. Anyway, the “center of intensity” method is accurate as long as the wavelet shape is only stretched or a given symmetry is preserved. It even provides a higher accuracy for non-symmetric wavelets compared to picking (section 3.4.2).

Amplitude In the given study, the term “amplitude” either stands for the magnitude of a signal at each point in time or for the strength of a signal, depending on the context. If “signal-strength” is meant, a reference will be given to the following definition: Two signals, $\psi_1(t) \neq 0$ and $\psi_2(t) \neq 0$, shall be given, which have equal shape but are scaled by a factor α . Then the signal strength is given by $\alpha = \psi_1(t)/\psi_2(t)$. Hence, any signal identification technique which is linear in the signal strength can also be employed to determine the latter or at least proxy information on it, on the basis of a reference signal.

4.4.2 Migration

Migration techniques are standard instruments to provide subsurface images from seismic data (e.g. [Yilmaz \[2001\]](#)), though they can also be applied with minor or without modifications to GPR datasets (e.g. [Daniels \[2004\]](#)). The general purpose of migration techniques is to transform CO sections to appear similar to the subsurface setting. This processing is necessary because of the dislocation of reflections by velocity heterogeneities and dipping interfaces: Because the angle of incidence and emergence are equal, the reflection point at a dipping interface does not coincide with the expected imaging point. The purpose of migration is to move the reflection signal to the actual

position where it originates. A prominent example where such a processing is necessary can be found in figure 4.5 between 10 m and 12 m and from 20 ns to 30 ns. The bow-tie shape is the reflection response of a synclinal structure at about 11 m (figure 6.1 and 6.2): At the image point location 10.5 m, for example, the upper reflection occurs from left slope while the lower reflection originates at the right slope.

Although not principally necessary, most migration procedures operate on several CMP or equivalently multi CO datasets. To achieve the final result the CMP data are stacked, i.e., for each time sample the amplitudes of all traces are summarized after the traces have been shifted to zero-offset ($a = 0$). This is done by employing a time transformation, which is based in the most simple case on (4.1). More sophisticated transformations also allow for dipping reflectors and vertical velocity variations. The information which is required for this can be obtained by cross-correlation velocity analysis. After stacking, a zero-offset CO section is obtained, and depending on the actual algorithm the migration processing step is carried out before (pre-stack) or after stacking (post-stack).

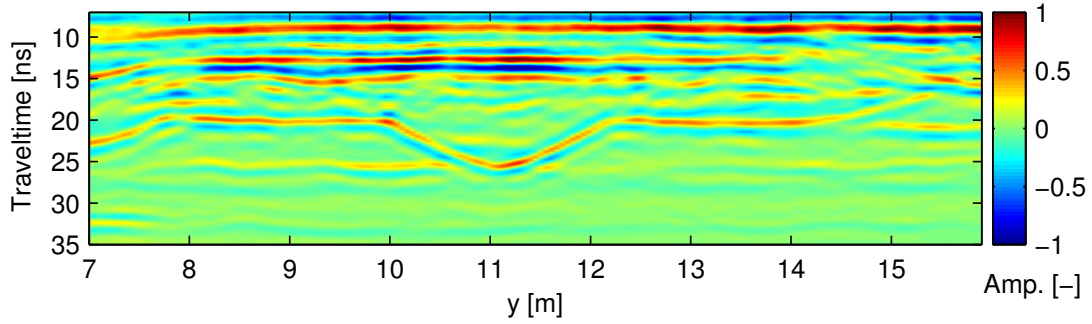


Figure 4.8: Time-migration result of the common-offset section provided in figure 4.5. The time axis is converted to zero offset time and $\varepsilon_r = 2$ was assumed.

Migration strategies which provide results in traveltimes coordinates are called time-migration. They are well suited if small lateral velocity variations are present. Figure 4.8 provides the results for the application of maximum convexity migration [Daniels, 2004] to the CO section given in figure 4.5. Since only single offset data were employed, no stacking was conducted, but the data were shifted to zero-offset. The result was retrieved by adding up all amplitudes of different traces which correspond to the same origin when assuming a point scatterer for every time-sample along a trace. For this, a certain range of neighboring traces is considered for the processing of one trace. Hence, the displayed window needed to be reduced in size compared to the original data. The figure shows that the strategy provides the demanded result as the reflections from the synclinal structure have been “folded” into each other to reveal the actual structure. In fact, this procedure is based on superposition and interference. Hence, the original reflection signals have not necessarily vanished but is just suppressed by the strong contrast to the new signals.

More sophisticated procedures provide information in depth coordinates and are thus called depth-migration. To convert the traveltimes into depth, a velocity model of the subsurface is necessary which is retrieved by an iterative procedure employing the different offset information contained in the CMP data. Thus the computational effort is increased, but also a velocity model is obtained.

The advantage of migration procedures is that a large variety of them is available and is suited for different settings. However, the major drawback is that many strategies rely on the superposition of signals which demands for a high data density.

4.4.3 Multichannel Evaluation

[Gerhards et al. \[2008\]](#) introduced a methodology to efficiently evaluate multi CO measurement data. The approach relies on the retrieval of traveltimes, by picking associated reflections in a set of CO sections. After shifting the sections to image-point coordinates, the traveltimes data are inverted at each point by an extended version of (4.1) to retrieve d , ε_r , and the dipping angle of a reflecting interface. By this, the method is in principle analogous to a CMP velocity analysis at each imaging point. However, it addresses the issue of sparse data by enabling the inclusion of traveltimes from a range of imaging points around the one of interest.

While an advantage of the method is the efficient processing, it includes the assumption of simplified ray-paths which is based on a two-layer model. That is, only one interface is represented in the forward model, even if multiple reflections (in depth) are subsequently evaluated. Hence, distortions of the ray-path by overlaying interfaces are not corrected for. [Buchner et al. \[2011\]](#) have shown that the method allows a reliable estimation of volumetric water content (obtained from dielectric permittivity by (3.41)) and interface position, to an accuracy of 3...4% vol. and 0.1 m, respectively. However, the authors also discuss possible strong correlations of the parameters leading to significant deviations induced by surface roughness effects. Additionally, the treatment of synclinal structures (as given in figure 4.5 between 10 m and 12 m and from 20 ns to 30 ns) and steep reflectors is not explicitly addressed and thus can lead to erroneous results.

In section 6.3 the method is compared to the one introduced in this thesis and deviations are discussed in detail.

4.4.4 Full-Waveform Inversion

Full-waveform inversion is a seismic and GPR evaluation technique which aims for the fitting of the complete signal. For this the data are inverted using a detailed representation of the measurement process and the subsurface. This includes the solution to the equations describing the propagation of the measurement signal, i.e., Maxwell's equations in the case of GPR.

The method was initially introduced by [Tarantola \[1984\]](#) for the inversion of seismic reflection data and is strongly related to depth-migration techniques. Independently, different implementations of this method have been developed to invert borehole GPR measurements in the frequency-domain [[Ellefson et al., 2011](#)] and in the time-domain

[Kuroda *et al.*, 2007]. Another time-domain realization of Ernst *et al.* [2007b] was improved by including the vector properties of the electric field [Meles *et al.*, 2010] and by optimizing the measurement setup [Klotzsche *et al.*, 2010]. All these methods rely on finite difference modeling which allows an arbitrary distribution of the electromagnetic properties. However, the waveform inversion problem is in general non-linear and ill-posed [Virieux and Operto, 2009]. This makes appropriate regularization and preconditioning techniques necessary (e.g. Guitten *et al.* [2012]). The typically huge number of unknowns (\approx the number of grid cells) also demands for a large number of different antenna configurations to make the inversion problem well conditioned. This involves a significant experimental and computational effort. Because of the oscillating behavior of waveforms, also local minima cannot be excluded. This is addressed by obtaining the initial parameter distribution from previous analysis of the data, e.g., by travelttime- and amplitude tomography (e.g. Ernst *et al.* [2007b]). However, fitting the full waveform also relies crucially on the knowledge of a proper source current function. This might be a challenging task if the permittivity distribution shows significant variations close to the antenna, which is likely in on-ground surface GPR surveys.

As a surface GPR full-waveform inversion technique, Lambot *et al.* [2004a] proposed a method operating off-ground and in the frequency domain. By utilizing the exact solution to Maxwell's equations, the method is limited to an effectively one-dimensional layer model of the subsurface. Busch *et al.* [2011] also showed the possibility to employ a frequency domain full-waveform inversion for on-ground CMP surveys, but also with the drawback of a horizontally layered medium.

In summary, many GPR evaluation techniques are available, which are ranging from pure imaging up to highly sophisticated methods, which provide quantitative information. A major drawback is that for some methods simplifying assumptions have to be made. This can be compensated by a high data density; for some methods, however, the latter goes even hand in hand with the simplifications. A common feature of all the above methods is that they essentially provide a local “snapshot” of the subsurface at the time of measurements. That is, the electromagnetic properties and the retrieved subsurface structure can show a spatially and temporally unexpected behavior. Hence, assumption like continuity of layer interfaces or their temporal consistency have to be implemented by regularization techniques or deduced by further evaluation and interpretation. To include such assumptions, however, allows to constrain inversion techniques and, more importantly, provides a direct interface to couple with models describing the observed system, like Richards equation (2.4) with respect to soil water dynamics.

5 Constructive Inversion

An alternative evaluation method, aiming to address the issues mentioned above, was proposed by *Buchner et al.* [2012]. The authors successfully demonstrate the inverse determination of subsurface structure and electromagnetic parameters from surface GPR measurements. For this study, the method was expanded and it is explained in more detail in the following. The general concept behind the method is denoted as “constructive inversion”, which is applied to multi-offset surface GPR data.

The method relies on an inversion scheme which is composed of four major components which are indicated in figure 5.1: (i) The execution of measurements and the initialization of the inversion by defining a subsurface model which is described by a set of parameters to be estimated. (ii) A forward model consisting of a FDTD solver of the two-dimensional Maxwell equations, which simulates the measurements by representing the electromagnetic properties using the subsurface model. (iii) A feature detection procedure which automatically detects reflected or direct signals and retrieves their traveltime and amplitude information. (iv) The pairwise association of the measured and simulated signals and a subsequent minimization of an objective function, the squared difference of the signals travel-times and amplitudes, to estimate the subsurface parameters.

The subsequent sections provide the details of the inversion scheme, employing mathematical formalism. To enable a simultaneous intuitive understanding, some steps are explained with using some instructive results of section 6.1.4 in the forehand.

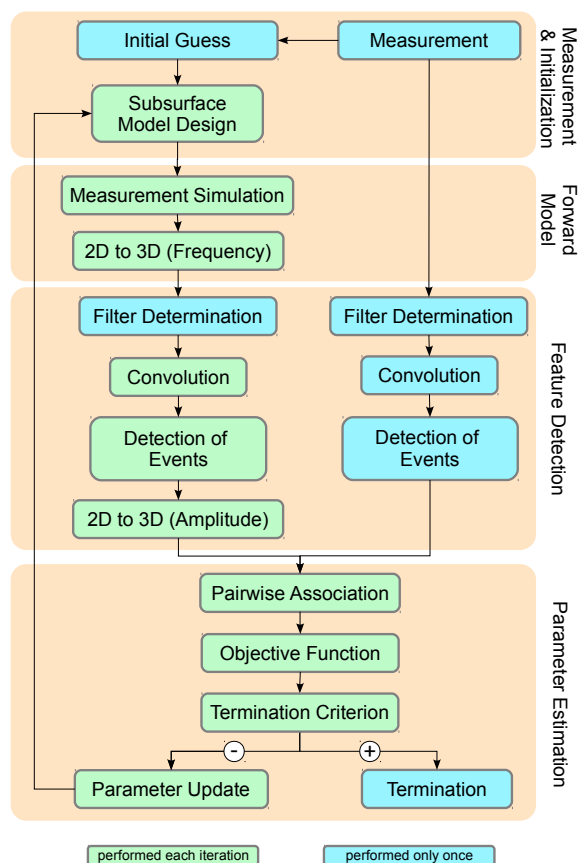


Figure 5.1: Flowchart describing the iterative processing sequence of the inversion scheme. The four orange boxes indicate the major components. Blue and green boxes correspond to individual steps which are carried out only once or for each iteration, respectively.

5.1 Measurement and Initialization

At the beginning of the evaluation stands, as a matter of course, some interest which is the motivation to carry out a GPR survey. The information which is of interest also determines – on the background of the findings of section 4.3 – the appropriate measurement setup and the subsequent design of the subsurface model, as described in the next three sections.

5.1.1 Measurements

The used multi common-offset datasets consist of N sections (e.g. figure 4.5) measured with different antenna separations 'a'. The different separations can either be realized by sequential measurements along the same line or by employing a multichannel setup (figure 4.4). All sections contain M equidistant traces, each comprising L samples recorded with a fixed time interval Δt . Each sample corresponds to one voltage V_{nml} measured at time $t = l\Delta t$ with $n \in \{1, \dots, N\}$, $m \in \{1, \dots, M\}$, and $l \in \{1, \dots, L\}$.

5.1.2 Initial Guess

After acquisition of the datasets, an interpretation follows to bring up an initial guess of the subsurface setting which is used to construct a subsurface model in the next step. The interpretation requires the user to judge what information in the data is of interest with respect to the objective of the survey. Optionally a first quantitative analysis of the data can be conducted, for instance with the method of [Gerhards et al. \[2008\]](#), to provide initial values of the parameters assigned to the subsurface model.

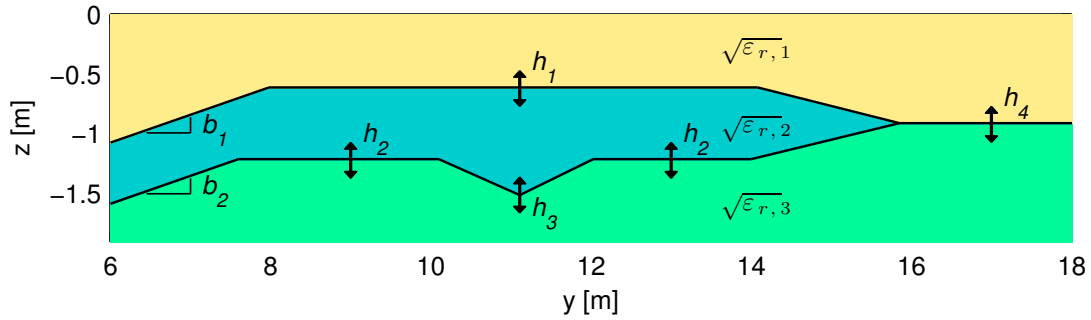


Figure 5.2: Subsurface model with the parameters represented by the different variables.

5.1.3 Subsurface Model Design

The subsurface model is designed on the basis of the initial guess and optionally with support of external information, e.g., from other measurement methods. If the existence of distinct layers appears to be a good assumption – on the basis of a qualitative interpretation of the acquired data and additional geological information – the subsurface geometry is constructed by the interfaces between the layers. By representing these interfaces by parameterized functions, as for example piece-wise linear ones in figure 5.2,

several geometrical parameters are associated with the subsurface model. In addition, the distribution of the electromagnetic properties of these layers is also expressed by functions, which introduces several electromagnetic parameters. Altogether, a set of parameters \mathfrak{P} is assigned to the model which are estimated by the inversion scheme.

5.2 Forward Model

The inversion of the measured data, to estimate the parameters \mathfrak{P} , demands for a forward model which provides simulated data, which can be quantitatively compared with the measured ones. In the given study this is obtained by simulating the GPR measurements with numerically solving Maxwell's equations. This is advantageous since an approximate antenna radiation characteristic is included, near field and higher order effects are accounted for, and because it correctly describes the effects resulting from placing the antennas at an interface (section 3.4.3); the latter allowing the employment of direct groundwave data. If the former effects can be neglected or only traveltime is of interest, an alternative with less computational effort would be to use an appropriate method based on ray-tracing or wavefront propagation (section 3.3.2).

5.2.1 Measurement Simulation

The GPR measurements are simulated by numerically solving equations (3.1)-(3.4) in two dimensions on the domain given by the subsurface model. The transmitter antenna is represented by an infinite dipole pointing in x-direction. It is placed on the surface and a vacuum layer is added above above. With that, any effects which are determined by the real antenna geometry (bow-tie), cross-coupling or the antenna shielding are neglected. The antenna source current density is given by a Ricker excitation function (A.1) with a predefined center frequency. The receiving antenna is not represented explicitly; instead \vec{E}_x at the position of the receiver antenna is used as the actually observed signal V . The spatial and temporal of the calculations are chosen such that the stability criterion (section 3.3.3.1) is fulfilled and the phase velocity error by numerical dispersion is small considering the following steps and the uncertainty of the measured data. Figure 5.3 provides an example of a simulated CO section.

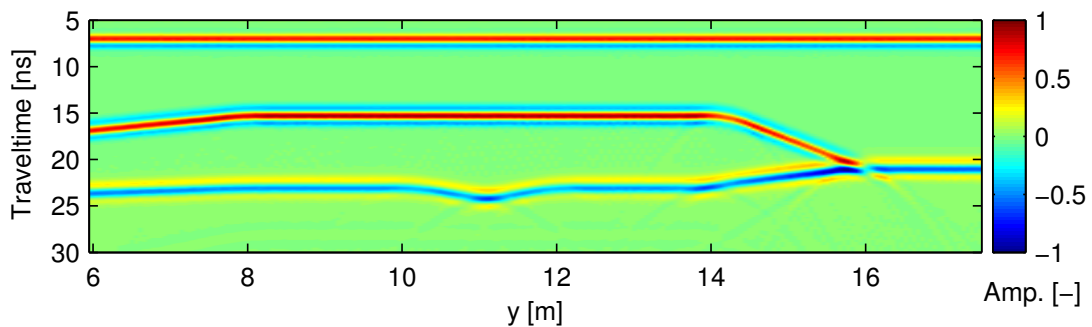


Figure 5.3: Simulated CO section with the same antenna separation as the section provided in figure 4.5, but with the initial guess of the subsurface model (different from figure 5.2).

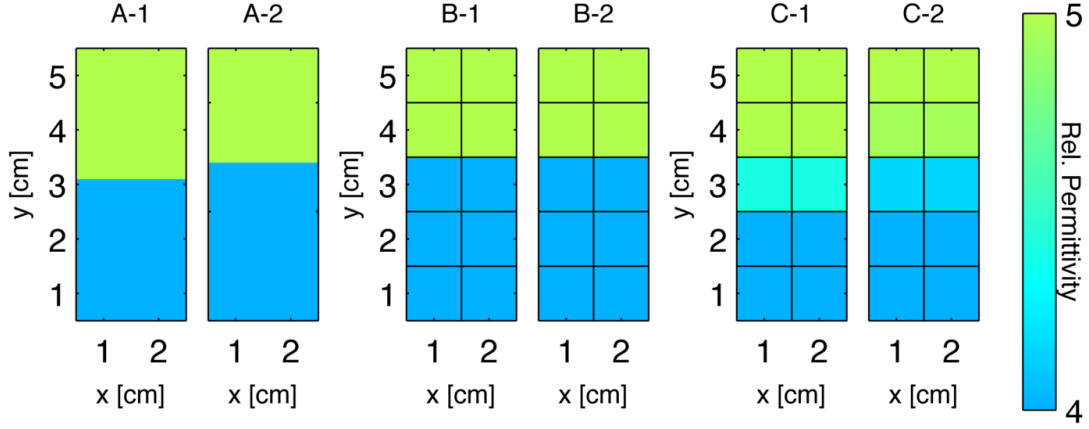


Figure 5.4: Two permittivity distributions (A-1 and A-2) with different interface positions and the resulting distributions after mapping to a structured grid without (B-1 and B-2) and with previous smoothing (C-1 and C-2). The smoothing is realized employing function (3.39) which is centered at the interface and has a width of $\zeta = \Delta x$.

Maxwell's equations are solved by employing MEEP (section 3.3.3.1) on a structured squared grid. Figure 5.4 demonstrates that small changes in the position of an interface are not necessarily recognized after mapping the actual permittivity distribution to the grid using the cell center coordinates. However, an additional smoothing of the permittivity distribution permits that even very small changes in the interface positions lead to changes in the permittivity on the grid. This causes the traveltime and amplitude of reflections occurring at the interface to be sensitive to these changes. This is important, because both quantities contribute to the objective function defined in section 5.4.2. Hence, it is practically guaranteed that the objective function also depends continuously on the geometrical parameters in \mathfrak{P} ; which is a necessary condition for the minimization of the objective function with a derivative based method like the employed Levenberg-Marquardt scheme.

Thus, in addition to the MEEP-internal sub-pixel smoothing of the electromagnetic properties, all layer interfaces are smeared out orthogonal to their extent, using function (3.39) with $\zeta = \Delta x$. For this small width, the impact on the amplitude and frequency content of a typical reflected wavelet was found to be negligible (section 3.5). Nevertheless, changes of the interface position which are three orders of magnitude smaller than the typical cell size can be reliably recognized in the traveltime of a reflected signal.

5.2.2 2D to 3D Conversion – Frequency Correction

Solving Maxwell's equations in just two dimensions involves an intrinsic discrepancy to the measurements which are three-dimensional (section 3.4.4).

However, there exists a transformation for the two-dimensional forward model prediction into “two-and-one-half dimensions” (equation (3.38)). The transformation can be split up into two major modifications: (i) A modification depending on the angular frequency ω and (ii) an amplitude correction, which is applied individually to each detected signal and is addressed later in section 5.3.4. For the first, each trace is transformed to the frequency-domain by the fast Fourier transform (FFT, denoted by $\hat{*}$) and subsequently each sample is modified as:

$$\hat{V}_{nml'} \xrightarrow[\text{correction}]{\text{frequency}} \hat{V}_{nml'} \cdot \sqrt{\frac{|\omega_{l'}|}{2\pi}} \exp \left[-\frac{i\pi}{4} \text{sign}(\omega_{l'}) \right] \quad \forall \quad n, m, l'. \quad (5.1)$$

Where $\omega_{l'} = \Delta\omega \cdot (l' - \frac{L'}{2})$, $l' \in \{1, \dots, L'\}$, and L' is the number of samples per trace enlarged to the next power of two, due to requirements of the FFT. Afterwards, all traces are transformed back to the time-domain by the inverse FFT and their length is readjusted.

5.3 Feature Detection

To compare the measured and modeled data, traveltime and amplitude information of individual signals has to be retrieved. For this purpose, a robust signal identification technique was developed which is based on the convolution of the absolute value of each trace with a filter function. The choice for an appropriate filter function was driven by four criteria: (i) When convolved with the absolute trace it should lead to unique local maxima for each direct or reflected signal. (ii) The temporal position and amplitude of these maxima should be sensitive to the complete wavelet, not just to some particular feature (as it is the case for picking techniques). (iii) To preserve amplitude information (in the sense of signal strength (section 4.4.1)) the filter should be linear in it. (iv) The filter should be scalable by its width and thus applicable to different wavelet shapes obtained in the used datasets.

A filter which has the demanded properties can be employed for both the modeled and measured data to retrieve traveltime and amplitude information, even if the wavelet shape differs. This makes a source-wavelet estimation obsolete. For this study, a Gaussian filter was chosen since it fulfills the upper requirements. Other filter functions, however, could possibly be applied as well.

5.3.1 Gaussian Filter Determination

The width of the Gaussian filter is determined once at the beginning of the workflow for the measured as well as the modeled data: A representative reflection wavelet ψ_l is selected and cut manually from the dataset, its absolute value $|\psi_l|$ is computed, and it is normalized to its maximum. Then, the discrete Gaussian shaped function

$$G_l := \exp\left(-\frac{l^2 \Delta t^2}{2\sigma_G^2}\right) \quad (5.2)$$

is fitted to the result (figure 5.5) by minimizing the sum of absolute differences to estimate the standard deviation σ_G : The upper limit of σ_G is obtained as the size of the cut window and the minimum is necessarily zero. This range is sampled with the time resolution of the trace. For each of these values of σ_G , $|\psi_l|$ is convolved with G_l . The maximum of each result is computed and the mean of the gaussian is fixed to its position. The optimal σ_G is then obtained as: $\min_{\sigma_G} \sum_l ||\psi_l| - G_l|$.

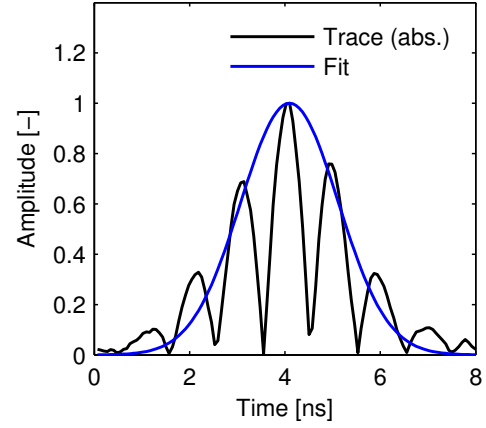


Figure 5.5: Determination of the filter (blue) by fitting a gaussian shaped function (equation (5.2)) to the absolute value of a representative wavelet (in black, from $y = 11.19$ m in figure 4.5).

5.3.2 Convolution

The absolute value of each trace is convolved with the Gaussian filter obtained in the previous step:

$$\tilde{V}_{nml} = \sum_{l'=l-5\sigma_G}^{l+5\sigma_G} |V_{nml'}| \cdot G_{l-l'} \quad \forall \quad n, m, l \quad (5.3)$$

with

$$V_{nml'} = 0 \quad \text{if } l' < 1 \vee l' > L. \quad (5.4)$$

Figure 5.6 provides an example of the implications of this procedure for a measured and a simulated trace. As can be noticed, the convolution removes the wavelets' details. However, it also simplifies the automated detection of signals along the trace since the actual computation is equivalent to the calculation of the cross-covariance between the trace and the Gaussian filter. The result indicates the optimal agreement of the Gaussian shaped function with the signals along the trace by local maxima.

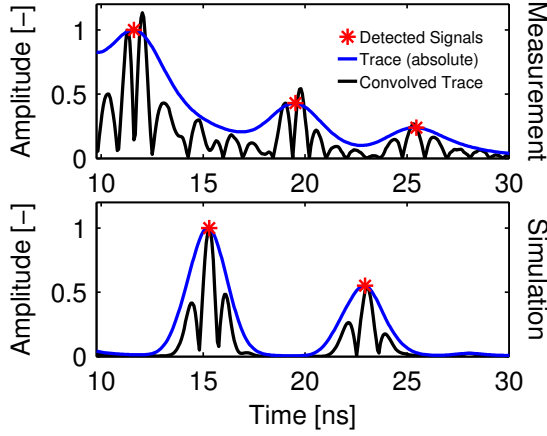


Figure 5.6: Automatic detection of events for measured (upper) and simulated (lower) data: the normalized absolute values of a trace (figure 4.5 at $y = 9.70$ m) are convolved with the Gaussian filter. The local maxima indicate the best agreement between the absolute trace and the Gaussian filter. These maxima are detected by their amplitude using a top-down approach. The amplitude above is normalized to the maximal amplitude of all detected events per trace.

The convolution can also be interpreted as the calculation of the weighted mean along each trace; with the weighting function given by G_l . By design (section 5.3.1), G_l has a similar extent as the signals of interest and thus information from the complete wavelet is included in the mean value. If $|V|$ is interpreted as the intensity of the signal, the local maxima also indicate the position of the local “center of intensity”.

With respect to amplitude (in the sense of signal strength (section 4.4.1)), the given approach has an important property: In case of negligible interference, the amplitude of the maxima scales with the amplitude of each wavelet since the convolution (equation (5.3)) is a linear operation with reference to scalar multiplication.

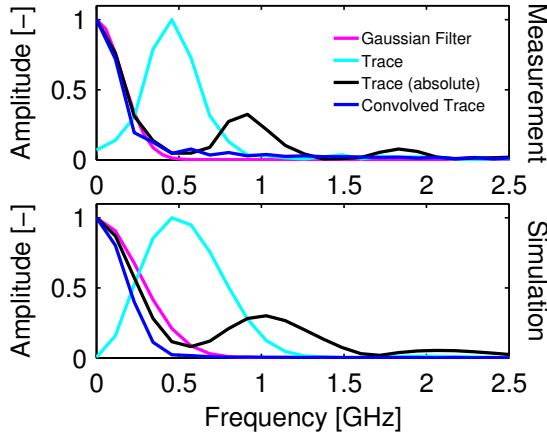


Figure 5.7: One-sided discrete amplitude spectra of the Gaussian filter together with the actual, the absolute, and the convolved trace given in figure 5.6. The upper and lower results are calculated from the time intervals 23.68...28.08 ns and 13.00...18.00 ns, respectively. The spectra are normalized to their maximum value.

From a different perspective, the computation represents a filtering of each trace, which cuts off high frequency components. This becomes clear by investigating the various signals in the frequency domain (figure 5.7): The computation of the absolute value adds low frequency components as well as it doubles the frequency of the main peak and introduces higher order modes. Both effects can be understood when considering the computation of the corresponding discrete Fourier coefficients

$$\hat{a}_{\omega_j} = \sum_{l=1}^L e^{-i\omega_j \Delta t(l-1)} |V_l|, \quad (5.5)$$

with $\omega_j = \frac{2\pi j}{\Delta t L}$. Since $|V_l| > 0$ for some l , $|\hat{a}_{\omega_j=0}| > 0$ as well. In contrast, \hat{a}_{ω_j} is small if ω_j is close to the center frequency of the wavelet: The approximately periodic but positive parts of the signal are added up after being multiplied with the real and imaginary parts of $e^{-i\omega_j \Delta t l}$. Since the latter change their signs with the double period, the contributions of the different positive wiggles cancel out each other. In contrast, if ω_j is double the center frequency of the wavelet, the canceling is not given; as becomes clear when analyzing the function $|\sin(2\pi t)| \cos(4\pi t)$ in a similar fashion.

The filtering of the absolute value of the trace with the Gaussian shaped function corresponds to a multiplication of the two functions in the frequency domain. This suppresses the higher frequency parts of the signal. By that the frequency composition as well as the time-domain representation of the absolute signal becomes similar to the Gaussian, at least with respect to shape.

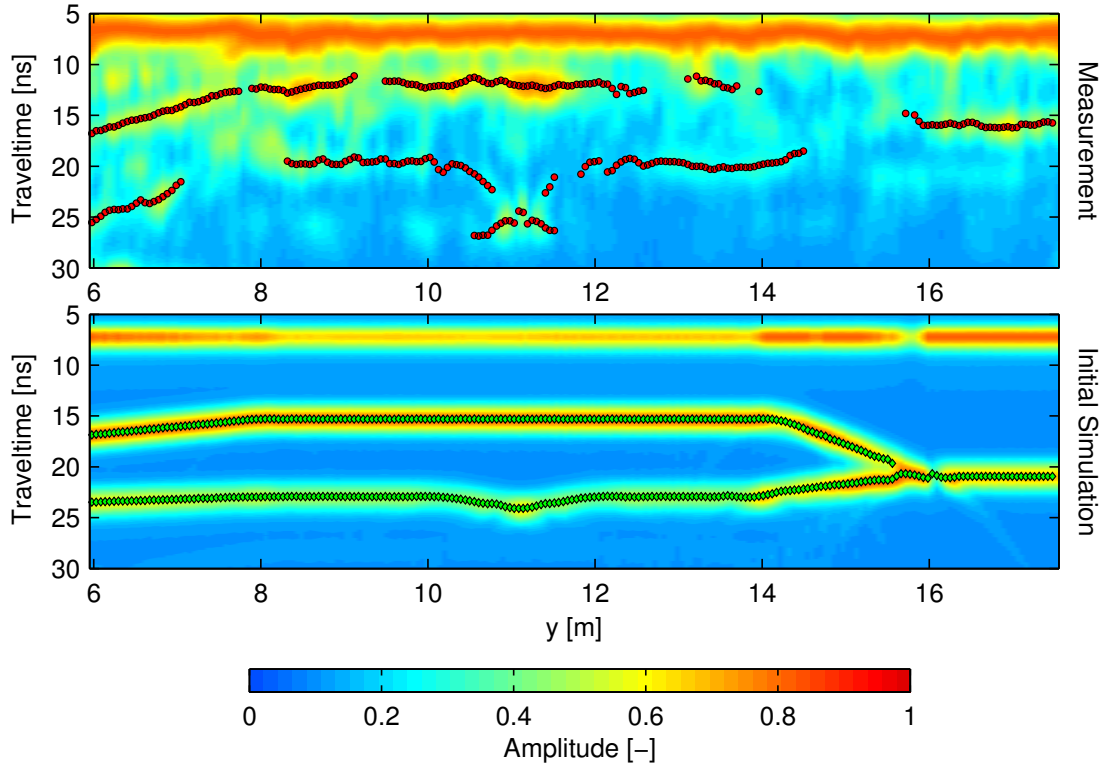


Figure 5.8: CO sections (figure 4.5 and 5.3) after the convolution with the corresponding Gaussian filters. The markers indicate the positions of the detected maxima. For the measured data the maxima of interest were manually selected. The colorscale represents the normalized amplitude of the convolved signal. For both, the direct groundwave signals (5-10 ns) are excluded from the evaluation and thus no markers are present.

5.3.3 Signal Detection

After normalization of each convolved trace to its maximum amplitude, the local amplitude maxima are detected (figure 5.6 and 5.8) following a top-down approach: The maximal \tilde{V}_{nml} is determined and all \tilde{V}_{nml} within the surrounding $\pm\sigma_G$ are excluded from further selection to prevent multiple recognition in case of strong distortions of the wavelet shape. This is repeated until Q maxima are found or all amplitudes are smaller than a noise threshold.

The traces are only provided with a discrete time sampling both by the measurement and by the forward model. Thus, the traveltimes of the maximal \tilde{V}_{nml} will also only be found at one of the time sampling points, which most likely does not correspond to the traveltimes of the actual maximum. This will rather be somewhere in-between two time sampling points. Hence, small changes in the actual maximum's traveltimes, e.g., caused by small changes in the model parameters, might not be recognized. The resulting implication, again, would be a discontinuous dependency of the objective function (5.10) on traveltimes and thus potentially on parameters contained in \mathfrak{P} . To prevent this, the maximum is first determined on the discrete time-grid. Then, traveltimes and amplitude are estimated by fitting a Gaussian to five samples around the maximum. Afterwards the new traveltimes are retrieved from the Gaussian's peak position.

Finally, all this can be expressed by mapping the individual traces to sets \mathfrak{M}_{nm} containing Q "events". Each event, representing a direct or reflected signal, consists of an amplitude A_{nmq} and a corresponding traveltimes t_{nmq} :

$$\left\{ \tilde{V}_{nm1}, \dots, \tilde{V}_{nmL} \right\} \xrightarrow[\text{detection}]{\text{signal}} \mathfrak{M}_{nm} = \left\{ \left(\begin{smallmatrix} A_{nm1} \\ t_{nm1} \end{smallmatrix} \right), \dots, \left(\begin{smallmatrix} A_{nmQ} \\ t_{nmQ} \end{smallmatrix} \right) \right\} \quad \forall \quad n, m. \quad (5.6)$$

For both the measured and simulated datasets the traveltimes are time-offset corrected, which is done for the simulated data with reference to an interface reflection. Hence, temporal shifts introduced by the convolution in (5.3) cancel out. In case that the direct groundwave signal (figure 3.6) is of interest, it is treated similar as a reflection signal. However, only the traveltimes information of the groundwave can be reliably exploited, while using the amplitude would require a very detailed representation of the antenna geometry and radiation pattern. Thus the amplitude information of the direct groundwave signal is not used. If the direct groundwave is not of interest anyway, it is omitted in the modeled dataset by estimating its traveltimes from the model-parameters. In case of the measured dataset, the direct groundwave is excluded by the manual selection of the events which are of interest.

Finally, the amplitudes are normalized to the maximum amplitude of each trace. This has the advantage that the magnitude of source current intensity, the antenna's geometry, ground coupling, and energy losses by reflections above the uppermost event, do not have to be represented in the simulation. Hence, only the amplitude ratio of different reflections is accounted for in the evaluation. However, the normalization has the implicit disadvantage that the amplitude information can only be exploited if several reflections are present along each trace. This could be improved by normalizing for instance to the maximal amplitude of a complete CO section. This strategy would have the more severe disadvantage that a parameter which influences this particular

maximal amplitude would also effect all amplitudes over the complete section. By that an artificial correlation of parameters would be introduced.

5.3.4 2D to 3D Conversion – Amplitude Correction

This step addresses the correction of amplitude (in the sense of signal strength (section 4.4.1)), corresponding to the frequency correction performed in (5.1). Assuming that t_{nmq} stems from a horizontal reflector which is reached on a straight ray-path, the distance d_{nmq} and mean square-root of the dielectric permittivity $\sqrt{\varepsilon_{r,nmq}}$ are computed for each event from its traveltime t_{nmq} as

$$\min_{d_{nmq}} \left| t_{nmq} - \frac{\sqrt{\varepsilon_{r,nmq}}}{c_0} \sqrt{4d_{nmq}^2 + a^2} \right| \quad (5.7)$$

given the restriction

$$\sqrt{\varepsilon_{r,nmq}} = \frac{1}{d_{nmq}} \int_0^{d_{nmq}} \sqrt{\varepsilon_r(z)} dz. \quad (5.8)$$

With this first-order approximation, the amplitude correction is performed for the modeled data via

$$A_{nmq} \xrightarrow[\text{correction}]{\text{amplitude}} A_{nmq} \sqrt{\frac{\sqrt{\varepsilon_{r,nmq}}}{c_0 d_{nmq}}}, \quad (5.9)$$

followed by a normalization similar as in the previous section.

Equation (5.9) states a modification of the amplitude, which is depending on the travel distance of each signal. Hence, to apply it at the same position of the processing chain as the frequency correction would make an automatic identification and cutting of each signal necessary. However, this identification is delivered by the signal detection procedure. Since the inverse FFT as well as the convolution are, for negligible interference, linear in reference to scalar multiplication the amplitude modification can be applied afterwards.

Although increasing computation time, the 2D to 3D correction – both for frequency and amplitude – is applied to the modeled data for every forward calculation and not to the measured data once at the beginning. This is because knowledge on the subsurface dielectric permittivity is required which is only reliably available for the modeled data.

Since amplitudes are set to zero for direct groundwave signals, transformation (5.9) becomes obsolete for these signals.

5.4 Parameter Estimation

In order to formulate the parameter estimation problem for the parameters \mathfrak{P} , the simulated events $\mathfrak{M}_{nm}^{\text{sim}}$ have to be related to the measured events $\mathfrak{M}_{nm}^{\text{meas}}$. After that relation is obtained, an objective function is defined as the squared difference of the events amplitudes and traveltimes. The parameters are estimated by minimizing this objective function.

The association of the events and the previous identification technique involve several complications which have to be treated. Hence, a direct comparison of the actual, the absolute, or even the convolved traces would be a favorable alternatives preventing this complications. This approach, which is employed by the full-waveform techniques (section 4.4.4), would make a source wavelet estimation necessary and does not allow to select the data of interest. Consequently, all information contained in the measured data – including clutter, irrelevant reflections, and wavelet deformations – would be accounted for by the inversion procedure. This, however, can make the parameter estimation problem ill-posed and likely causes the occurrence of local minima in the objective function.

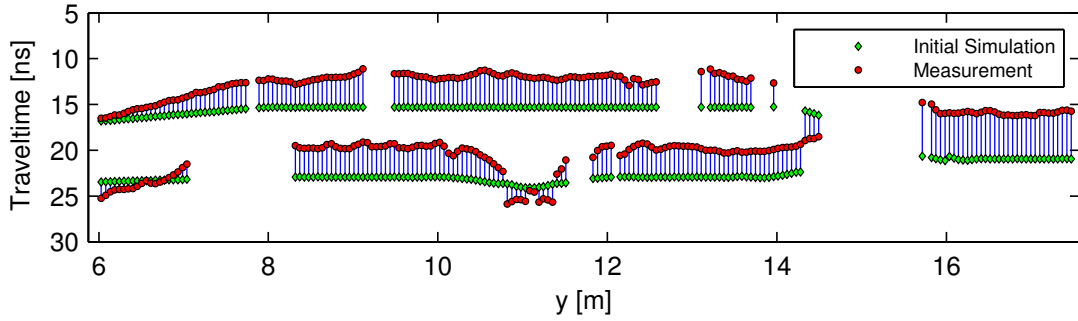


Figure 5.9: Example of pairwise association of events which were detected in the measured and the simulated data (same as in figure 5.8). Measured events without a partner are excluded and thus not shown.

5.4.1 Pairwise Association

The measured and modeled events are related to each other in every inversion step via a heuristic approach which forms pairs of events (figure 5.9): For each trace, all possible combinations of pairwise associations of the measured $\mathcal{M}_{nm}^{\text{meas}}$ with the modeled events $\mathcal{M}_{nm}^{\text{sim}}$ are computed, assuming each event can find one or no partner. From all combinations with a maximal number of possible pairs, the one with the minimal summed squared difference in traveltime is chosen to retrieve the final pairwise association. However, there is the possibility that the number of events in $\mathcal{M}_{nm}^{\text{meas}}$ is different than in $\mathcal{M}_{nm}^{\text{sim}}$. If this is the case and more modeled events are present, some of these do not find a partner and they are excluded for this particular inversion step. In the alternative case of more measured events, the measured events without a partner are “tagged” as partnerless. These tagged events are treated separately as described below. Finally, the amplitudes of the modeled results are again normalized for each trace to the maximum amplitude of events with a partner.

Associations may change during the parameter estimation process, i.e., events may find a different partner, tagged events may get untagged, or vice versa. This is a particular challenge dealt with in the following section.

5.4.2 Objective Function

To state the actual parameter estimation problem for the parameter-set \mathfrak{P} , the objective function

$$\Omega(\vec{p}) = \sum_{n=1}^N \sum_{m=1}^M \sum_{q=1}^Q \left[\left(\frac{A(\vec{p})_{nmq}^{\text{sim}} - A_{nmq'}^{\text{meas}}}{\sigma_A} \right)^2 + \left(\frac{t(\vec{p})_{nmq}^{\text{sim}} - t_{nmq'}^{\text{meas}}}{\sigma_t} \right)^2 \right] \quad (5.10)$$

is defined. Here, $\left(\frac{A(\vec{p})_{nmq}^{\text{sim}}}{t(\vec{p})_{nmq}^{\text{sim}}} \right)$ and $\left(\frac{A_{nmq'}^{\text{sim}}}{t_{nmq'}^{\text{meas}}} \right)$ are the events which have been associated with each other in the previous step, while σ_A and σ_t denote the standard deviation of the measured amplitude and traveltime, respectively. The parameter vector \vec{p} has P entries corresponding to the elements of \mathfrak{P} . The summations cover all sections, traces, and events per trace; although the number of events can actually vary with each trace. This is handled operationally by ignoring additional entries in Ω with setting both the measured and simulated values of A and t to zero if less than Q events are given in a measured trace. The actual parameter estimation problem is given by minimizing Ω with respect to \vec{p} . It is solved iteratively via the Levenberg-Marquardt [[Marquardt, 1963](#)] routine for which the parameter update $\Delta\vec{p}$ in each iteration is obtained by solving the linear system of equations

$$[\mathbf{S} + \Lambda \cdot \text{diag}(\mathbf{S})]\Delta\vec{p} = \vec{R} \quad (5.11)$$

employing singular value decomposition [[Press et al., 1992](#)]. In the above equation \mathbf{S} stands for the sensitivity matrix, Λ is the positive damping factor, and \vec{R} the weighted residuum. To define these quantities equation (5.10) is redefined as

$$\Omega(\vec{p}) := \sum_{j=1}^{2NMQ} \left(\frac{y_j - f_j(\vec{p})}{\sigma_j} \right)^2. \quad (5.12)$$

Here, the index $j \in \{1, \dots, 2NMQ\}$ relates to the index triple nmq in (5.10) by

$$j = \begin{cases} 2q + 2(m-1)Q + 2(n-1)MQ & \text{if } j \text{ is even} \\ 2q + 2(m-1)Q + 2(n-1)MQ - 1 & \text{if } j \text{ is uneven.} \end{cases} \quad (5.13)$$

With that the data vector is given by

$$y_j := \begin{cases} A_{nmq}^{\text{meas}} & \text{if } j \text{ is even} \\ t_{nmq}^{\text{meas}} & \text{if } j \text{ is uneven} \end{cases} \quad (5.14)$$

and the forward model is defined accordingly as

$$f_j(\vec{p}) := \begin{cases} A_{nmq}^{\text{sim}}(\vec{p}) & \text{if } j \text{ is even} \\ t_{nmq}^{\text{sim}}(\vec{p}) & \text{if } j \text{ is uneven.} \end{cases} \quad (5.15)$$

This provides the Jacobian matrix obtained from numerical differentiation as

$$\mathbf{J}_{i,j} = \frac{f_j(\vec{p} + \delta p_i \vec{e}_i) - f_j(\vec{p})}{\delta p_i} \quad (5.16)$$

$$\forall i \in \{1, \dots, P\} \wedge j \in \{1, \dots, 2NMQ\}, \quad (5.17)$$

where δp_i is the disturbance of the i -th parameter, and \vec{e}_i a cartesian unit vector in i -th direction. Finally the sensitivity matrix and the weighted residuum are defined as

$$S_{i,k} = \sum_{j=1}^{2NMQ} \frac{J_{i,j} J_{j,k}}{\sigma_j^2} \quad \forall i, k \in \{1, \dots, P\} \quad (5.18)$$

and

$$R_i = \sum_{j=1}^{2NMQ} \frac{J_{i,j} [y_j - f_j(\vec{p})]}{\sigma_j^2}, \quad (5.19)$$

respectively.

Due to certain parameter choices during the estimation process, signals may change their amplitude or even disappear. Furthermore the complete reflection answer from interfaces, can change its shape in the simulated CO section. For example the reflections stemming from the syncline at $y \approx 11$ m (figure 5.2) appear continuous in y -direction if $h_2 - h_3 \approx 0$, as it is the case in figure 5.3. In contrast, the real data show a bow-tie shape of the reflections (figure 4.5), i.e., in close proximity of the syncline two events appear. Thus, only one of these events can find a partner in the simulated data, while the other one is excluded and tagged. However, when the syncline gets more pronounced, i.e., the difference $h_2 - h_3$ gets larger, during the parameter estimation process, the bow-tie shape also appears in the simulated data. Hence, the association changes and the tagged events which were previously excluded become untagged. Since this has relevant implications on Ω , modifications of the Levenberg-Marquardt scheme were necessary:

1. The contribution to Ω and J of a measured event which was tagged because no partner was found is excluded, i.e., A and t of the event as well as of a hypothetically simulated partner are set to zero.
2. If an event has been tagged and becomes untagged after the parameter update, the contribution of the event and its new partner to Ω is added to the recent as well all previous objective function values. If an event has not been tagged and becomes tagged after the parameter update, its contribution to Ω is subtracted from recent as well as all previous values of Ω . This prevents the objective function from getting discontinuous in its dependency on the parameters. An example of this is provided by the syncline case mentioned above: When the double events around the syncline get untagged because of the improvement of the parameters, a significant contribution is introduced to Ω by these events. If the reduction of Ω , stemming from the previously untagged events, is smaller than this contribution, the new parameters would be rejected although they are closer to the optimal parameter set. In summary, the above modification changes the number of significant terms in (5.10), during the estimation procedure. This in turn means that the slope of the objective function changes with the changing number of terms; a fact which can directly be derived for any linear forward model.

3. The tagging also has to be considered for the computation of J . Thus, $J_{i,j}$ of tagged events are set to zero, which excludes these events from the inversion process. Since S , which results from J , is just an approximation of curvature it will not change significantly with a small number of tagged events. In addition to the above reason for tagging changes, the association may also vary when the parameters are disturbed to compute the derivatives. This may lead to large changes in traveltime or amplitude difference and hence to wrong entries in J . If the residuum of model prediction and the measured value is nonzero for the corresponding entry, this entry would be overweighted, the parameter update could be disturbed and the inversion procedure take a wrong route or get stuck. To prevent this, entries of J exceeding some extremal values are set to zero. These extremal values are obtained from exemplary cases by manually identifying events for which the association changed during the parameter disturbance.

5.4.3 Termination Criterion

For the Levenberg-Marquardt routine the damping factor Λ is decreased or increased in each iteration by one order of magnitude if the objective function can be improved or not, respectively. The routine terminates if λ exceeds 10^{10} or if the relative improvement of Ω with respect to Ω of the previous step falls below a chosen level. In both cases, the termination criterion determines if the algorithm has reached a point where it is not able to significantly decrease Ω by a parameter correction. This, however, does not necessarily imply that the global minimum of Ω is found. Hence, the fit quality has to be judged by the user.

6 Results and Discussion

In the following, four applications of the constructive inversion method are presented. To investigate the consistency, performance, and accuracy of the approach, it is tested with a synthetic and a measured dataset obtained at the ASSESS-GPR testbed. The methods applicability to field data is demonstrated at the Hirschacker dataset, while the evaluation of the data observed in Daheigang shows the advantages of the approach when applied to a time-series of measurements. Computational aspects, such as the specific parallelization and the computational effort involved with the analyses, are provided in section A.3.

Please note, that for the descriptions of radargrams, the term “reflections” is occasionally used with an extended meaning: Instead of the reflection of a single wave, the reflected signals of several waves, recorded at different positions but stemming from the same interface, are meant. This is useful if these signals appear continuous in radargrams (as for instance in figure 5.3 between 6 m and 15 m and 20 ns and 25 ns).

6.1 Performance Test and Accuracy Analysis

This section closely follows *Buchner et al.* [2012], who applied the inversion scheme to the man-build ASSESS-GPR testbed (next section), which provides detailed ground-truth on a known layer geometry and point information on the subsurface dielectric permittivity and thus water content. By comparing the ground-truth data to the inversion results, the performance of the constructive inversion method is investigated.

6.1.1 The ASSESS-GPR Testbed

The ASSESS-GPR testbed (figure 6.1 and A.1) was designed and build with the purpose to analyze the accuracy of surface GPR measurements in vadose zone applications. Thus, detailed information on the geometry as well the dielectric permittivity respectively the volumetric water content is provided. The site is located in the close surrounding of Heidelberg, Germany and consists of an artificial sand volume placed in a concrete cuboid which is 4 m wide, 19 m long, and 2 m deep. The bottom and the walls of the cuboid are sealed with polyethylene foil to ensure that no water can enter or leave the testbed from these boundaries. In contrast, the surface is open to the atmosphere what makes precipitation and evaporation inducing the upper boundary condition of the water dynamics. The testbed consists of five layers made from three types of quartz sand (table A.1), with translational symmetry along the x-axis (figure 6.1). The subsurface geometry comprises a variety of simplified but basic features (figure 6.2) which are also characteristic for natural soils: (i) multiple layers, (ii) dipped interfaces, (iii) a syncline ($y > 10 \text{ m} \wedge y < 12 \text{ m}$), and (iv) an interface merging point ($y = 16 \text{ m}$). The layers

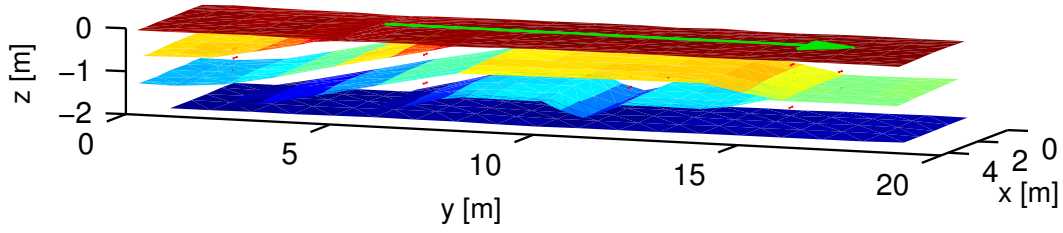


Figure 6.1: Three dimensional illustration of the geometry at the ASSESS-GPR testbed. The lowest interface corresponds to the upper surface of the gravel layer while the sand surface is at the top. The green arrow represents the GPR measurement line (y -direction at $x = 2.1\text{ m}$) and the red markers indicate the position of TDR probes. The probe centers are located at $x = 0.8\text{ m}$, i.e., 1.3 m besides the GPR line. A rotating view of the geometry is provided in the movie [ASSESS_Geometry_3D.mp4](#).

were built into the volume and finally compacted using a vibrating plate (figure A.1b) to prevent compaction by the materials own weight after the building. The positions of the layer interfaces were obtained with a TCRA1102 tachymeter (Leica GeoSystems, Germany) and by manual measurements (figure A.1c); hence ground-truth information on the layer geometry is provided with a precision of 1 cm. However, the accuracy of the information when comparing with GPR-data is most-likely not better than 5 cm. The reasons are (i) additional compaction of the sand layers during the building procedure, (ii) changes of the soil surface height by external influences, (iii) sinking of the GPR antennas into the sand, and (iv) the variations of geometry along the x -direction. The latter is relevant since the comparison is made between the 2D crosscut (figure 6.2) in y -direction and the evaluation of GPR data. The data, however, also include information transverse to the measurement line because of the three-dimensional propagation of the electromagnetic pulses in the subsurface.

Spatial or temporal changes in water content cause significant changes in the effective dielectric permittivity of the sand-water-air mixture. In the unsaturated state, the water content across layer interfaces is discontinuous (figure 2.5) in most cases if the layers' hydraulic properties are different due to variations of the pore-size distribution. On the one hand this can be induced by differences in the grain-size distribution, as given for the materials build into the testbed (table A.1). On the other hand, spatial variations of porosity, as possibly introduced by the compaction of the layers, affect the pore geometry. For both reasons jumps in dielectric permittivity are expected across the interfaces in the testbed.

Dielectric permittivity of as well as direct current conductivity is observed at 32 positions. This is done by temperature and TDR probes (figure 6.2). The latter have 3 rods of 0.2m length. The measurements are conducted on a regular basis by a TDR100 time-domain reflectometer (Campbell Scientific, UT, USA) which is part of an automatic weather station.

The TDR probes were calibrated in the laboratory for dielectric permittivity and conductivity measurements. The evaluation for both quantities is conducted with standard techniques [Roth *et al.*, 1990, Heimovaara *et al.*, 1995] employing signal traveltime and attenuation, respectively.

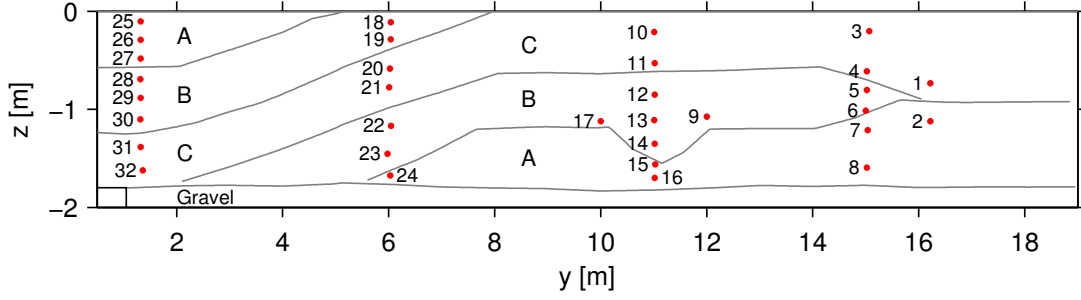


Figure 6.2: Crosscut along the GPR measurement line (figure 6.1). The capital letters (A,B,C) indicate the different sand types (table A.1). The positions of the TDR sensors are indicated by the red dots.

6.1.2 GPR data acquisition

Two shielded bistatic GPR antenna pairs (Ingegneria dei Sistemi S.p.A., Italy) with a nominal center frequency of 400 MHz were employed in a multichannel setup (figure 4.4) to sequentially record multi common-offset sections with different box-separation. The employed data are part of a dataset which was recorded in the context of the state examine work of Kühne [2010]. Only the longer cross-box channel provided reliable data and thus the quantitative analysis is restricted to it. Altogether, seven sections with different antenna separations were observed (figure 6.4), along the measurement line shown in figure 6.1. The crosscut below that measurement line is provided in figure 6.2. For each CO section, 217 equidistant traces with a distance of 0.053 m were recorded with 586 samples over a time window of 40 ns. The recording was triggered by a measuring wheel.

6.1.3 Synthetic Test

Before applying the inversion scheme to the real dataset, it was tested with a synthetic dataset which was generated equally to the real dataset. This allows to show the consistency of the approach, in the sense that the actual parameter estimation problem can be addressed at all and that the problem is well-posed by the employed antenna separations.

To save computational resources, the trace distance was doubled. The subsurface model (figure 5.2) which was chosen for the real and the synthetic dataset is a simplified representation of the subsurface setting at the ASSESS-GPR testbed (figure 6.2). The middle part of the volume ($y = 6 \dots 18$ m) is represented by three layers, each having constant electromagnetic properties.

Figure 5.2 shows the set of parameters $\mathfrak{P} = \{h_1, h_2, h_3, h_4, b_1, b_2, \sqrt{\varepsilon_{r,1}}, \sqrt{\varepsilon_{r,2}}, \sqrt{\varepsilon_{r,3}}\}$ which was assigned to the model. The symbols $h_{1\dots 4}$ denote vertical interface positions, b_1 and b_2 are slopes of interfaces. $\sqrt{\varepsilon_r}$ is preferred to dielectric permittivity itself because of the linear dependency of the waves' traveltimes on it. The layers are assumed to be uniform in $\sqrt{\varepsilon_{r,1}}, \sqrt{\varepsilon_{r,2}}, \sqrt{\varepsilon_{r,3}}$ and h_1, h_2, h_4 are valid for the flat parts of the interfaces,

respectively. To reduce the number of degrees of freedom, each interface is assumed to be continuous in y -direction. Direct current conductivity was assumed to be constant with a value of 0.003 S m^{-1} and was not estimated.

The true parameters for the subsurface model are given in table 6.1. The nominal frequency of the Ricker source current function (A.1) was set to 400 MHz. Traveltimes and amplitude values observed after the detection of reflection events were randomly perturbed with standard deviations similar to the ones observed for the real dataset (0.4 ns for the traveltimes and 0.1 for the amplitudes). For the FDTD simulation, the spatial resolution and the Courant number were chosen as 0.0125 m and 0.5, respectively.

Parameter	Initial	Estimated	True
$\sqrt{\varepsilon_{r,1}}$ [-]	3.150	2.899 ± 0.010	2.900
$\sqrt{\varepsilon_{r,2}}$ [-]	2.600	2.403 ± 0.013	2.400
$\sqrt{\varepsilon_{r,3}}$ [-]	6.000	4.970 ± 0.301	5.000
b_1 [-]	0.150	0.234 ± 0.007	0.233
b_2 [-]	0.300	0.233 ± 0.004	0.233
h_1 [m]	1.150	1.299 ± 0.004	1.300
h_2 [m]	0.550	0.700 ± 0.004	0.700
h_3 [m]	0.250	0.402 ± 0.007	0.400
h_4 [m]	0.800	1.000 ± 0.004	1.000

Table 6.1: Initial, estimated, and true parameter values of the subsurface model (figure 5.2) used for the evaluation of the synthetic dataset.

The inversion procedure was started with the initial parameter set given in table 6.1. Since both the synthetic and simulated measurements are retrieved in two dimensions, the correction to three dimensions was not necessary.

Figure 6.3 shows the convergence of the Levenberg-Marquardt routine. An example of how the non-linearity of the inversion problem arises, is apparent when considering b_1 and the association of events in figure 5.9 from $y = 6 \dots 8 \text{ m}$ and $t = 12 \dots 18 \text{ ns}$. In the given situation, the algorithm will decrease b_1 . Nevertheless, it will also increase h_1 and decrease $\sqrt{\varepsilon_{r,1}}$ such that all events stemming from this interface get a shorter traveltime. Hence, after a parameter update the events from the dipping part of the interface might have shorter traveltimes than the measured ones and b_1 needs to be increased again.

Figure 6.3: Evolution of Ω for each step of the iterative parameter estimation. The slope of the curve changes drastically due to changes in the association, i.e., by the variations in the number of significant terms in Ω , but also caused by the non-linearity of the problem.

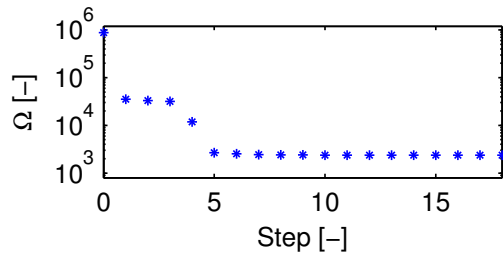


Table 6.1 shows that the method is able to estimate the real parameters within their 1σ confidence limits obtained from the covariance estimate of the Levenberg-Marquardt algorithm. Comparing the standard deviations of the $\sqrt{\varepsilon_{r,i}}$, the one for $\sqrt{\varepsilon_{r,3}}$ is largest. This expresses that $\sqrt{\varepsilon_{r,3}}$ is only depending on amplitude information of the reflection

from the lower interface. Since the standard deviation of the amplitude values is larger than that of the traveltimes, the estimation of $\sqrt{\varepsilon_{r,3}}$ is less reliable. However, it is a significant advantage of this method to be able to estimate this parameter, which would not be accessible by traveltime information alone.

6.1.4 Real Dataset

The synthetic test showed the ability of the inversion method to solve the actual inversion problem. By this, however, the influence of systematic errors of the measurement process and of simplifying assumptions by the measurement simulations is not captured. To demonstrate that the method still provides accurate results, it was applied to the real dataset obtained at the ASSESS-GPR site.

Inversion Scheme Setup The data, observed in the GPR acquisition (figure 6.4), were used to design the subsurface model (figure 5.2). By assuming this model and simulating the measurements by the 2D solution to Maxwell's equation, translational symmetry in x-direction is inherently assumed; however, this is a reasonable simplification since the symmetry can be approximately assumed for the testbed as well. The parameterization of the subsurface model was chosen on the basis of the known general shape of the interfaces. Some of the interfaces did not lead to significant reflections and were not included in the model. An example of this is the uppermost dipping interface in figure 6.2 between $y = 6 \dots 8$ m.

The initial parameters (table 6.3) were chosen such that large initial differences in traveltime and amplitude were given between the measured and modeled data (figure 5.9). However, there are some general limitations to the choice of the initial parameters which had to be fulfilled:

1. The contrast in $\sqrt{\varepsilon_r}$ at an interface must be large enough to reliably detect reflections.
2. Reflections must not vanish by interference with other reflections or the direct groundwave.
3. The relation between $\sqrt{\varepsilon_r}$ of different layers has to be similar to the optimal configuration. That is, for example, if $\sqrt{\varepsilon_{r,1}} > \sqrt{\varepsilon_{r,2}}$ for the optimal parameter set, this has to be true for the initial values as well. Otherwise, $J_{i,j}$ in (5.16) for amplitude values may have the wrong sign. Consequently, the parameter update may be wrong as well and finding of the minimum of Ω is not guaranteed. Anyway, this leads to an obvious deviation in the fitting result and thus may be clearly identified and overcome by changing the initial values appropriately.
4. The association has to be correct for a majority of the events. If, for instance the upper reflections in figure 6.5 are associated to the lower ones of the simulated data, the algorithm could converge to a local minimum of Ω . Nevertheless, comparing the associations in figure 5.9 and figure 6.5 around $y = 14.5$ m and at the syncline reflection demonstrates that the method is able to overcome few wrong associations.

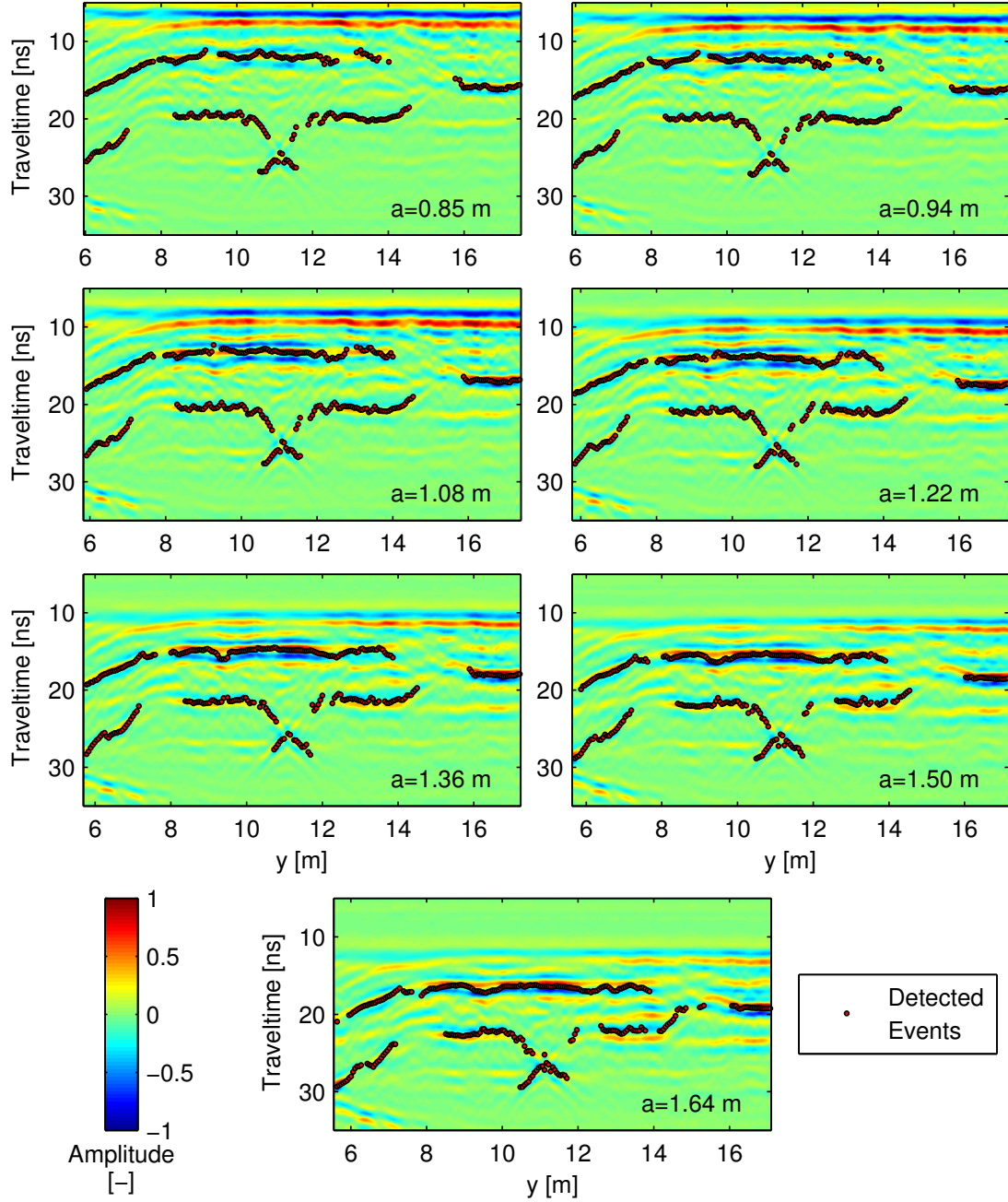


Figure 6.4: Measured CO sections (time-offset corrected) obtained with seven different antenna separations 'a' (lower right of each graph) and a nominal center frequency of 400 MHz. In each section the events are indicated which were retrieved from the feature detection procedure, followed by a manual selection of the ones corresponding to the reflections of interest.

Direct current conductivity was set to 0.0022 S m^{-1} and 0.0031 S m^{-1} for the upper and middle layer, respectively. These values correspond to the mean of the TDR measurements in these layers (figure 6.2). For the lowest layer, conductivity was set to zero since it has only a negligible impact on the amplitudes of the reflections from the lower interface. A nominal frequency of 400 MHz of the Ricker source current function (A.1) was assumed for the measurement simulation. The width σ_G of the Gaussian shaped function (5.2) was found to be 1.02 ns and 0.61 ns for the real and the simulated measurement, respectively. The spatial resolution of the FDTD routine was set to 0.01 m with a Courant number of 0.5. The amplitude noise-level threshold was set to 0.1 to ensure that only major reflections are automatically detected.

Given the Gaussian filter function, the feature detection procedure was applied to the direct signal recorded in air, by tilting the antennas, and to the data observed on the measurement line. From that the time-offset and the events shown in figure 6.4 were obtained. Having these, the standard deviations of the traveltime and amplitude measurements were estimated individually for each antenna separation. Employing the variations of a reflection from a horizontal part of the lower interface they were found as provided in table 6.2.

a [m]	0.85	0.94	1.08	1.22	1.36	1.50	1.64
σ_t [ns]	0.20	0.20	0.24	0.20	0.24	0.28	0.28
σ_A [-]	0.11	0.10	0.08	0.08	0.07	0.10	0.10

Table 6.2: Standard deviations of traveltime (σ_t) and amplitude (σ_A) of the measured events for the different antenna separations (a).

Estimation Results Figure 6.5 and 6.6 depict the fitting result for the traveltime and amplitude differences, respectively. For both, the fit is judged to be satisfying, except of the differences around $y = 15 \text{ m}$ for $a = 1.64 \text{ m}$. The measured events in this region were included since they appear trustworthy in figure 6.4. However, the fitting results show that their traveltimes cannot be reproduced by the simulated data with the given geometry restrictions of subsurface model. Hence, the measured traveltimes in this region are likely biased by interference with reflections from compaction interfaces, which were introduced during the building process.

Around $y = 6.5 \text{ m}$ the model significantly overestimates the amplitude. However, the related measured traveltimes also show a flattening around this position. A comparable effect can also be found for the lower reflection around $y = 13 \text{ m}$. Here, the situation is vice versa, i.e., the model underestimates the amplitude. Again, the explanation can be found by investigating the traveltimes. In this case, however, the ones of the upper reflection are relevant, where a strong variation is present. Since the amplitudes are normalized to the upper reflections, variations in their amplitudes are translated to the amplitudes of the lower reflections. Both cases represent the general finding that the amplitude variations are correlated with variations in traveltime. The reason for this effect is artificially generated surface roughness caused by the movement of the antennas. Due to the roughness the antennas are rotated and energy which is radiated towards the reflection point changes with the angular dependency of the radiation pattern (section 3.4.2).

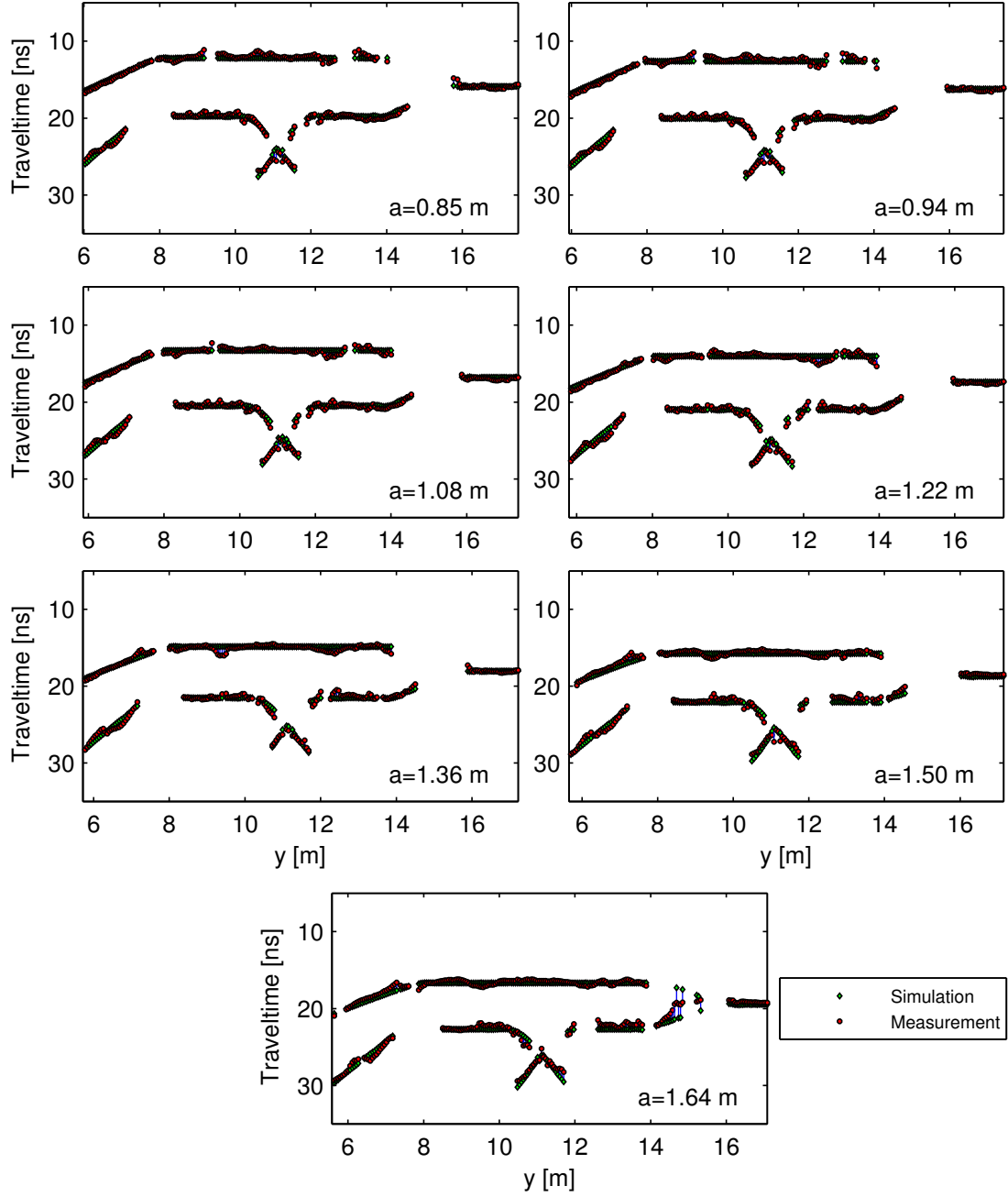


Figure 6.5: Results of the final inversion step for all employed antenna separations (lower right of each graph). The graphs shows the traveltimes of the simulated and measured (same as figure 6.4) event pairs.

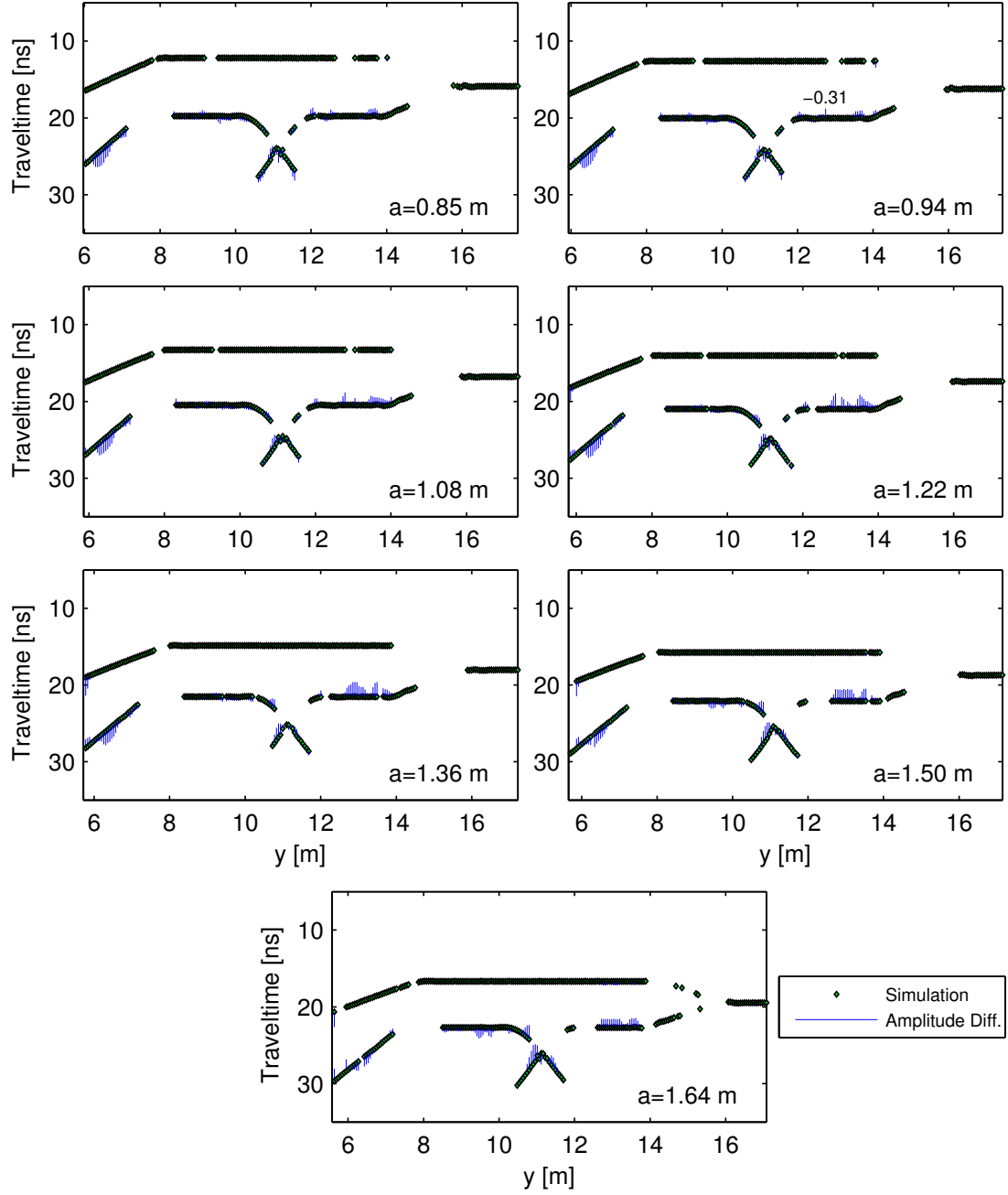


Figure 6.6: Amplitude differences corresponding to the event pairs given in figure 6.5 for all employed antenna separations (lower right of each graph). The traveltime of the simulated events is shown while the amplitude difference to their measured partners is indicated by the blue lines. The length of these lines times a factor of 0.25 ns^{-1} corresponds to the magnitude of the amplitude difference. A reference example is given for $a = 0.94$ m at $y = 12.74$ m. The direction indicates its sign (negative time-direction means that the amplitude of the modeled event is lower than the measured one). Because of the amplitude normalization, the maximum amplitudes for each trace are equal to one and show no difference.

No kinks are present in the convergence of the estimation routine (figure 6.7) since there is only one tagged reflection event after the first step. The graph also demonstrates the fast convergence, since after just five steps Ω is reduced by a factor of 30 and the parameters deviate less than 2.5 % from their final values. The reason for the six more steps, showing only small improvement, is the nonlinearity of the problem and the strict termination criterion. Thus, by weakening the latter the computation time could be significantly reduced without heavily compromising the accuracy of the estimated parameters.

The comparison for the layer geometry is shown in figure 6.8. The results show an agreement within the accuracy range of the ground-truth measurements for almost all parts of the interfaces. Exceptions are the slight deviations at the bottom of the syncline and around $y = 14.0$ m at the upper interface. Both deviations are most likely caused by a too coarse representation of the structure.

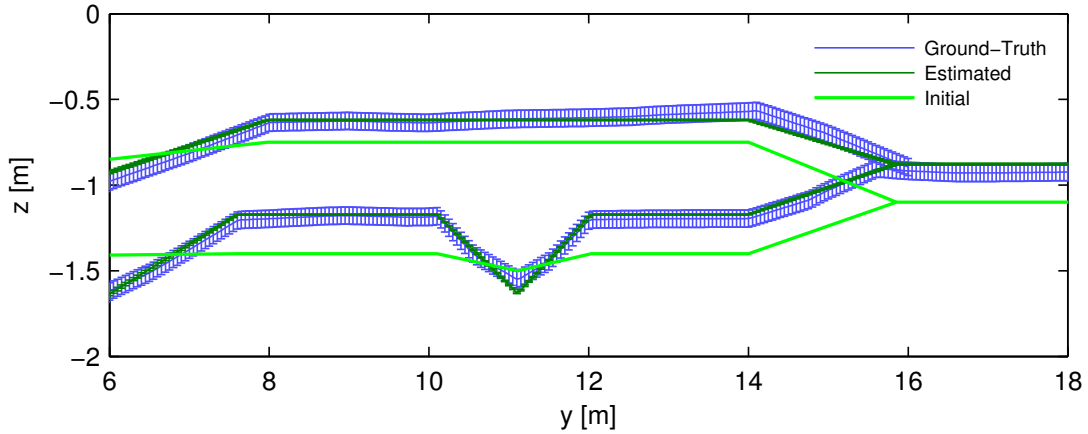


Figure 6.8: Comparison between ground-truth and estimated geometry. The error-bars of the ground-truth and the estimation represent the ± 0.05 m accuracy range and the covariance estimate of the Levenberg-Marquardt routine, respectively. The movie [ASSESS_Geometry_Comparison.mp4](#) provides the comparison for all iteration steps.

The comparison between the estimated $\sqrt{\varepsilon_r}$, and the ones observed by the TDR is presented in table 6.3. Since the estimated values are valid for a complete layer the ground-truth values had to be averaged. However, because of the sparse probe density in y -direction, an horizontal averaging would sufficiently lack accuracy. Hence, averaging was only done for each layer and vertically over probes which were positioned on a straight line. The used probes are indicated by the superscript numbers. The measurements of these probes were interpolated linearly, while values above the highest or below the lowest probe were set to the value of these probes. Afterwards, the average of the

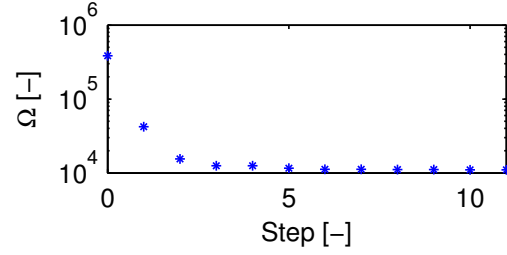


Figure 6.7: Ω for each step of the iterative parameter estimation process.

interpolation was computed. The confidence limits represent the precision of the TDR measurements determined from their temporal fluctuations after detrending. However, these values are at the lower limit of error estimation, since (i) the actual accuracy of TDR measurements is considered to be about 1 % [Roth *et al.*, 1990]. (ii) Deviations can occur since TDR probes are located 1.3 m off the GPR measurement line. (iii) The linear interpolation can differ from the actual vertical water content distribution.

Table 6.3: Initial values and estimation results for $\sqrt{\varepsilon_{r,i}}$ and θ with their confidence limits for the real measurement compared to the ground-truth data observed from the TDR probes. The superscripts at the ground-truth values indicate the TDR probes (figure 6.2) which were used for interpolation.

Parameter	Initial	Estimated	Ground-Truth		
$\sqrt{\varepsilon_{r,1}}$ [-]	2.65	2.45 ± 0.01	$2.33 \pm 0.01^{20,21}$	$2.37 \pm 0.02^{10,11}$	$2.31 \pm 0.01^{3,4}$
$\sqrt{\varepsilon_{r,2}}$ [-]	2.00	2.31 ± 0.01	$2.28 \pm 0.01^{22,23}$	$2.34 \pm 0.01^{12,13,14}$	$2.33 \pm 0.01^{5,6}$
$\sqrt{\varepsilon_{r,3}}$ [-]	4.00	2.61 ± 0.01	4.81 ± 0.03^{24}	3.17 ± 0.02^{15}	2.41 ± 0.01^7
θ_1 [%]	10.9	8.2 ± 0.1	$6.9 \pm 0.3^{20,21}$	$7.4 \pm 0.3^{10,11}$	$6.6 \pm 0.3^{3,4}$
θ_2 [%]	2.8	6.6 ± 0.1	$6.4 \pm 0.2^{22,23}$	$7.1 \pm 0.2^{12,13,14}$	$6.9 \pm 0.2^{5,6}$
θ_3 [%]	28.0	10.7 ± 0.5	38.2 ± 0.3^{24}	17.5 ± 0.3^{15}	7.9 ± 0.2^7

Although the values do not agree within the error estimates, the agreement is still considered to be acceptable for the following reasons. (i) For both, ground-truth and estimation, a slightly higher $\sqrt{\varepsilon_r}$ is found in the upper layer compared to the middle layer. (ii) The deviations in the upper two layers are less than 10 %. (iii) The values observed for $\sqrt{\varepsilon_{r,3}}$ by the probes directly below the lowest interface show a clear increase with depth. This represents the increase of water content with depth towards the saturated part at the bottom of the volume. Hence, the estimated $\sqrt{\varepsilon_{r,3}}$, which represents a mean value over the complete interface of the lowest layer, is expected to lie in-between the ground-truth values, which is the case.

Table 6.3 also gives the results for mean volumetric water content which has been calculated via (3.41). For this purpose porosity and relative dielectric permittivity of the quartz sand were chosen as 0.37 (observed from samples) and 5, respectively. The dielectric permittivity of water was temperature-corrected employing equation 8 of Kaatz [1989]. For the same reasons as for $\sqrt{\varepsilon_r}$ the interpretation of the water content results for the lowest layer is limited. However, the water contents of the upper two layers show no difference larger than 2 % vol. in water content.

Recalling additionally the finding that the geometry can be determined almost everywhere within the accuracy range of ± 5 cm, the comparison between ground-truth and estimation results show a good agreement for a field method like GPR. It also demonstrates that the constructive inversion method is able to handle the various subsurface features (section 6.1.1), which alludes its suitability for field applications.

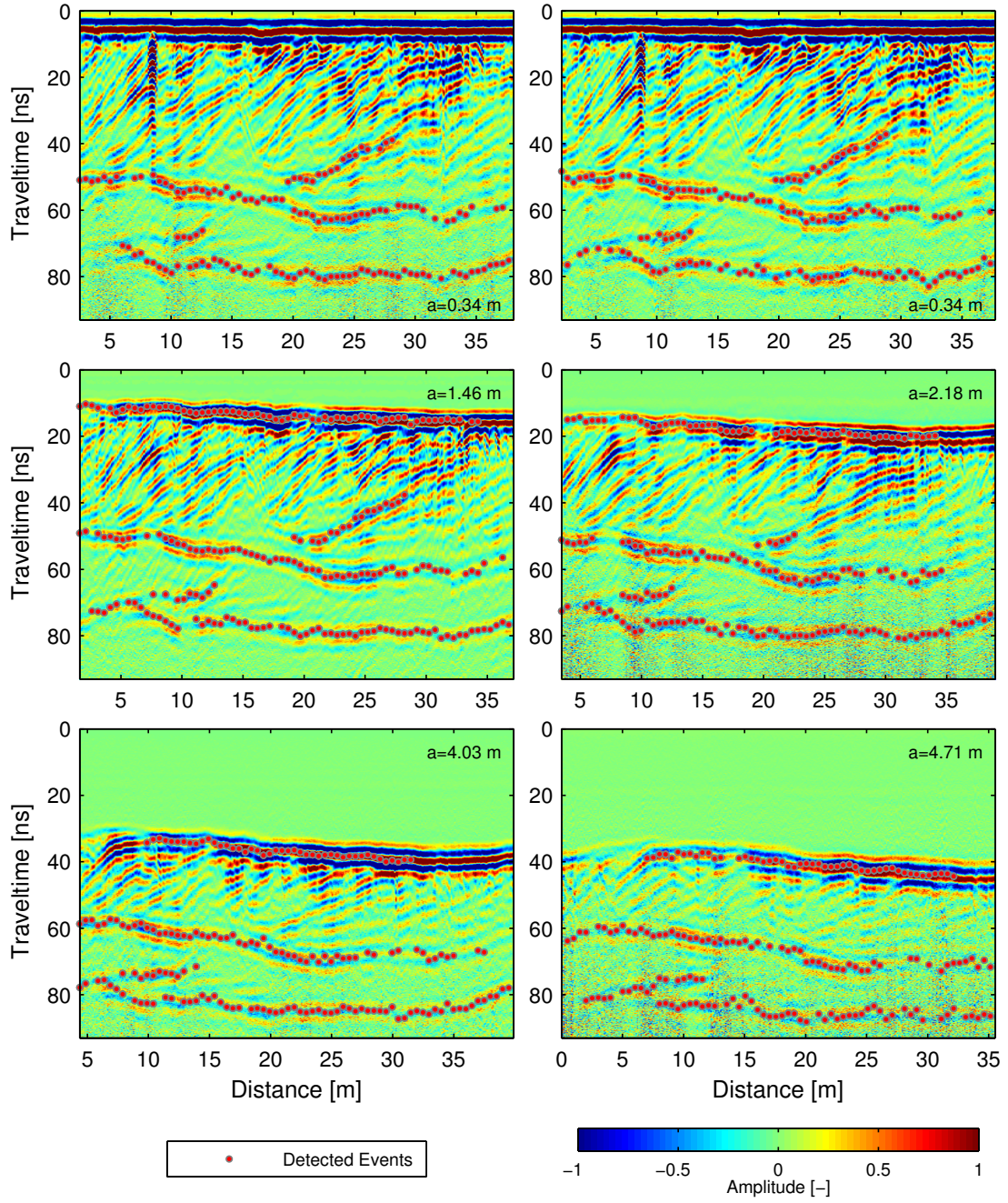


Figure 6.9: CO sections measured with a nominal frequency of 250 MHz for the different antenna separations ' a ' (lower or upper right of each graph). The two shortest separations correspond to the internal channels, while the others were retrieved from the four cross-box channels. Each section is time-offset corrected and the imaging-points spatially referred to the coordinates of the subsurface structure. For imaging purposes, an amplitude gain $\propto t^{1.5}$ was applied to each trace. The events obtained from the feature detection procedure with subsequent manual selection are indicated.

6.2 Field Measurements at Hirschacker

The evaluation which is discussed in this section is based on a GPR dataset (also investigated by [Schneider \[2007\]](#) and [Gerhards \[2008\]](#)) which was obtained at the military drill ground and nature protection area “Hirschacker and Dossenwald” close to Oftersheim, Germany. The survey area is widely forested with the presence of glades, which are vegetated with sparse grass cover. The topography is partly shaped by aeolian dunes and with that the dominant soil fraction is characterized as sand. The subsurface layer geometry is shaped by different stages of dune development.

The subsurface model in the previous example was strongly restricted by employing piecewise linear functions to describe the interfaces and assuming constant values of $\sqrt{\varepsilon_r}$ for each layer. While this was reasonable for the upper layers in that case, the subsurface setting in natural soils is expected to be more complicated. Hence, this is addressed in the given case by employing smooth spline functions for the interfaces and similar ones for the distribution of $\sqrt{\varepsilon_r}$ to account for its horizontal variability. This approach, however, involves a larger amount of parameters to be estimated, but consequently allows for a more detailed interpretation of the hydraulic state of the subsurface.

GPR survey A surface GPR survey was performed at the site with two shielded bistatic antenna pairs (nominal frequency of 250 MHz, MALÅ Geoscience, Sweden) operated in a multichannel setup (figure 4.4). Two sequential CO measurements were conducted back and forth the same line with different box separations, but a common trace distance of 0.1 m. The trace recording was triggered by a measurement wheel. For the evaluation, six CO sections were used which are shown in figure 6.9. While two of them correspond to the internal channels with the same antenna separation, the four others are retrieved from the cross-box channels and have different antenna separations. The sequential measurements resulted in a spatial shift, which was determined by minimizing the mean absolute difference between the overlapping parts of the internal channel sections.

Dataset Description Figure 6.9 provides the recorded radargrams which show several characteristic and common features:

- Prominent direct wave signals, which are present at the top of each radargram. Since these are an interference of the direct air- and groundwave for the internal channels, only the pure direct groundwave signals of the cross-box channels can be used for the evaluation.
- Several diagonal reflections are present in the upper region of the radargrams (e.g. between 10 and 50 ns for the internal channels). However, these signals show strong interference with each other and are not of interest in the following.
- Below the diagonal reflections, there are three reflections which are continuous along the measurement line. Two of them are dominantly horizontal while the other one crosses the radargrams diagonally. The hypothesis is that these signals

corresponds to four layer interfaces with spatial trends which are similar to the reflections.

- The penetration depth is found to be about 4 m, which is comparatively high. This also expresses in the fact that even for long antenna separations a significant reflection is recorded from the lowest interface. Hence, it is concluded from the findings in section 3.2.2, that (i) electric conductivity and the imaginary part of ε_r have an insignificant impact on the signal attenuation considering the precision of the employed amplitude information and (ii) that dispersive effects are negligible as well.
- The signal-to-noise ratio in the sections of the long cross-box channel with $a = 2.18$ m is worse compared to the short cross-box channel with $a = 4.03$ m, although the latter travel path is longer. This is an instructive example of the dependency of the observed signal on the technical configuration. However, the convolution procedure applied during the feature detection enables a reliable usage of the data.

Inversion Scheme Setup The subsurface model (figure 6.10) employed in the inversion scheme was designed with the assumption of four continuous interfaces which delineate five layers. The subsurface model was constructed by setting several interpolation points for the layer interface positions. In addition, interpolation points were set for the magnitude of vertical mean dielectric permittivity in the region covered by the GPR

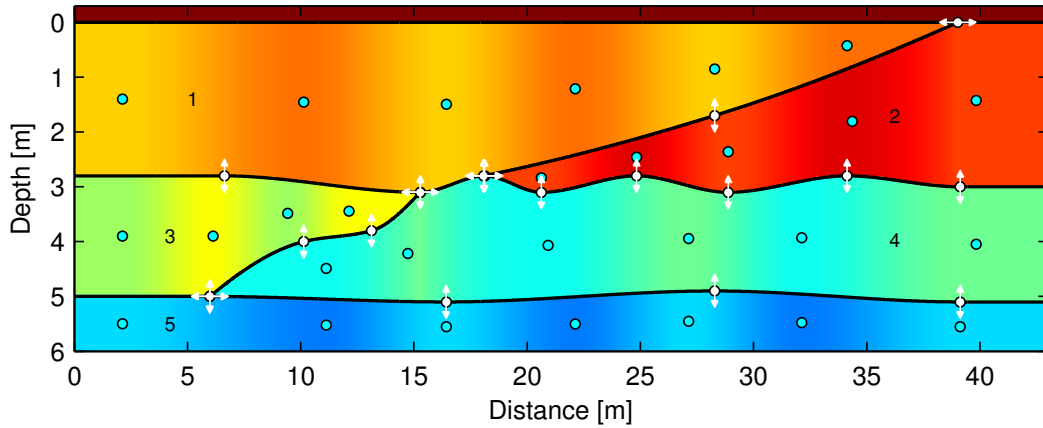


Figure 6.10: Subsurface model representing the volume observed by the GPR survey. White and cyan points mark the interpolation points of interface position and dielectric permittivity. The points are connected by spline functions to retrieve the interfaces' position (black line) and vertical mean permittivity (color). The interpolation points are enabled to vary in permittivity magnitude as well as in vertical and horizontal position (indicated by the white arrows). The color variations represent the shape of the spline functions of permittivity with arbitrary absolute values.

measurements. In contrast to the previous dataset, this allowed the estimation of the horizontal variability of the dielectric permittivity in addition to the one of the geometry. Representing the vertical variability in each layer is not realizable if the parameter estimation relies on traveltimes and amplitudes of reflections measured at the surface. The interpolation points of each layer and each interface were connected employing monotonic cubic piecewise spline functions [Fritsch and Carlson, 1980]. Using this type of splines prevents overshoots around interpolation points, which would in turn introduce variations contradicting the assumed shape of the interface. The derivatives at the open ends were set to zero and by that all degrees of freedom of the spline are restricted in combination with the monotonicity condition.

The interpolation points were set such that the spatial variability of the radar data is represented at the scale of interest, which is in this case several meters. That is, the data variability at a smaller scale is not attempted to be represented in the subsurface model and thus considered as statistical variations which is quantified by σ_t (table 6.4).

To obtain the events indicated in figure 6.9 the standard deviation of the Gaussian filter function was determined (table 6.4) from representative reflection wavelets. On that basis, the time-offset was determined from the direct signal observed by emitting the antennas in air. However, for the internal channels a significant offset between the simulated and measured events occurred during the fitting procedure. This is explained by strong changes of the wavelet shape due to the ground coupling (section 3.4.2); an effect which is most significant for the internal channels, since antenna crosstalk is possible and the direct signal is given as a mixture of the direct air- and groundwave. Hence, by carrying out a test-fit, this offset was determined as -1.7 ns and -1.8 ns from the final result for the first and second internal channel, respectively.

a [m]	0.34	0.34	1.46	2.18	4.03	4.71
σ_G [ns]	1.96	1.74	1.85	2.07	1.96	2.07
σ_t [ns]	1.00	1.11	0.89	1.03	0.61	1.38
σ_A [-]	0.22	0.21	0.20	0.16	0.15	0.16

Table 6.4: Gaussian filter width σ_G as well as the standard deviations of measured traveltimes σ_t and amplitudes σ_A for the different antenna separations a .

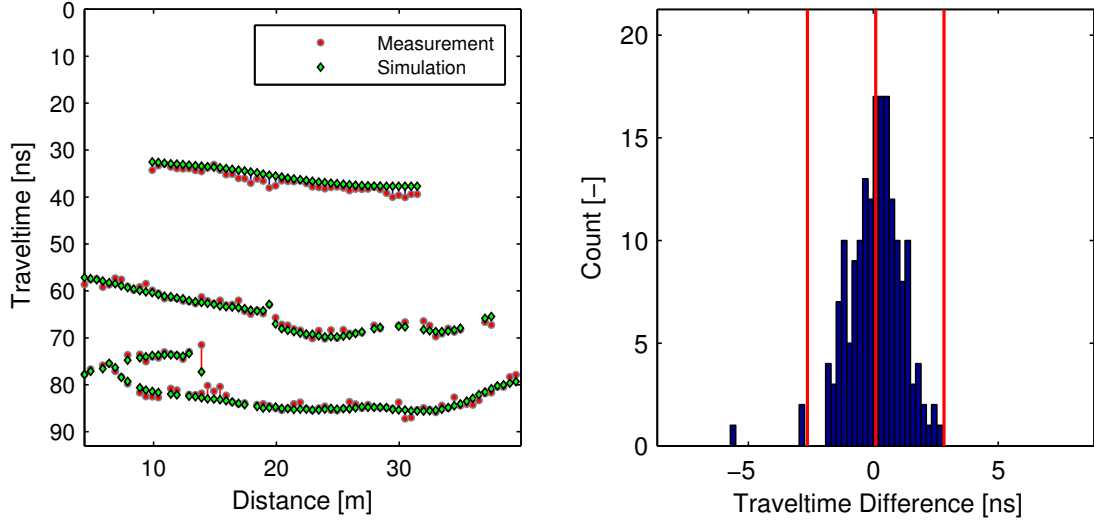
Applying the Gaussian filter to every 5th trace, events were detected and subsequently the ones of interest were selected. In the given case these were the reflections from the four continuous interfaces as well as the direct groundwave signals of the cross-box channels. The latter were not used if interference with reflections is present in the measured data or expected in the modeled data; as below 8 m and between 32 and 39 m for $a = 4.03$ m. Employing several of the lower reflections with similar traveltime, σ_t and σ_A were determined and are given in table 6.4. One can find that the worse signal-to-noise ratio of the longer cross-box channel causes statistical variations of the traveltime of the detected events, which is manifested in σ_t . Independent from that, the standard deviation of the normalized amplitude σ_A is high compared to the previous dataset (table 6.2). This expresses that this information is significantly worse in precision compared to traveltime and consequently had a smaller impact in the parameter estimation. Nevertheless, it can still be utilized to get an estimate of the permittivity of the lowest layer. This is possible, even in the presence of the diagonally reflections in the upper part of the radargrams: The used events all occur below these reflections and

the amplitude is normalized to the maximum event amplitude along each trace. Thus, the upper layers do not have to be represented in the subsurface model with respect to amplitude. The same holds for traveltimes, since the influence of the upper reflections is represented in the forward model by the average permittivity.

To obtain the simulated measurements, Maxwell's equations were solved in 2D on the domain defined by the subsurface model with an overlying vacuum layer of one meter extent. By solving the equations in two dimensions it is implicitly assumed that the subsurface has translational symmetry in the direction pointing out of the projection plane. This assumption fails in general when considering the spatial variability along the measurement line to be representative in the symmetry direction. However, if no side reflections are present and the measurement line is in direction of steepest ascent of the diagonal interface, the assumption is still reasonable. The simulations were carried out with a spatial resolution of 0.014 m and Courant number 0.5, while the source current density was given by a Ricker wavelet with a nominal frequency of 250 MHz. As discussed above, electric conductivity was not accounted for. Traces were recorded with at the same positions where the events are detected, i.e., with a trace distance of 0.5 m. For the feature detection, σ_G is determined to be 0.87 ns and no noise-level threshold was employed. Since the number of reflections per trace depends on the antenna position, the number of events to be detected is set accordingly. The direct groundwave events were also detected and distinguished from reflections by their expected traveltime, which was deduced in every inversion step from the subsurface model. They were only included in the evaluation if no interference with the airwave is given.

The inversion procedure was initialized with a linear interface shape and constant permittivity for each layer, such that the majority of simulated events were assigned correctly to the measured events. Due to the presence of several interfaces which merge at only four points, the interfaces were restricted not to cross at other positions. Similar to the previous evaluation, the permittivity distribution had to be initialized such that the relation between different permittivity values was similar to the optimal solution. Additional restrictions to the permittivity distributions were given by the phase of the measured reflection signals. Thus, at each interface the permittivity of the adjacent layers had to fulfill the constraints $\varepsilon_{r,1} > \varepsilon_{r,2}$, $\varepsilon_{r,3} > \varepsilon_{r,1}$, $\varepsilon_{r,4} > \varepsilon_{r,3}$, $\varepsilon_{r,4} > \varepsilon_{r,2}$, $\varepsilon_{r,5} > \varepsilon_{r,3}$, and $\varepsilon_{r,5} > \varepsilon_{r,4}$; with the subscripts denoting the layer numbers shown in figure 6.10. The actual parameters which were estimated, however, were the $\sqrt{\varepsilon_{r,i}}$, because of the linear dependency of traveltimes on these.

Steep interfaces, the crossing of interfaces and the necessity to estimate the horizontal position of the crossing points makes the association of events potentially defective. This can lead to wrong associations, e.g., in figure 6.11 (a). Because of the large traveltime difference of the most prominent outlier, which quadratically contributes to Ω , the Levenberg-Marquardt algorithm would correct the parameters to decrease this difference. However, this correction would actually be wrong, since it would result in a larger traveltime difference for some of the correctly associated pairs. To prevent this, a basic outlier detection procedure was employed for this evaluation: The mean and standard deviation σ of the traveltime differences of each CO section was computed, including the outliers. Then all event pairs of each section with a traveltime difference



(a) Measured and simulated events obtained for $a = 4.03$ m for iteration step six. The blue lines indicate the association of events while the red lines mark the three event pairs which are identified by the outlier detection procedure.

(b) Histogram of the traveltime differences in (a). The red lines mark the distribution's mean and the $\pm 2.5\sigma$ bounds referred to the mean. The three outliers are given at the left hand side of the left bound.

Figure 6.11: Example of the outlier detection procedure.

which is below or above the 2.5σ bounds (figure 6.11 (b)) were excluded by treating them as tagged events (section 5.4.2). Although the example shows that the procedure has the intended effect, also correctly associated event pairs were excluded. Because of redundancy of the measured data, however, the parameter estimation problem is still well posed if a small number of correctly associated event pairs is excluded. In the given evaluation, the number of excluded pairs (including outliers) was never larger than 5 % per section.

Estimation Results Figure 6.12 depicts the traveltime fit, obtained after 12 successful parameter updates and finally reaching $\Lambda = 10^{10}$. The fit shows systematic deviations for the direct groundwave events in some CO sections. This is, first of all, due to the representation of permittivity by a vertical averages: The measured groundwave traveltimes are only determined by uppermost part of the subsurface, while the simulated ones are retrieved from the averages. These, however, represent the complete vertical extent of the layer and are also determined by the reflection traveltimes. Secondly, a systematic trend to shorter traveltimes is present in the last CO section ($a = 4.71$ m), which is balanced by the fit. Since this trend is also present for the reflections, it is most likely caused by an erroneous determination of the time-offset for this particular CO section. But, in contrast to the internal channels (as discussed above), no theoretical justification is given for a correction. The systematic traveltime differences in the last CO section also lead to a trend in the amplitude differences (figure 6.13).

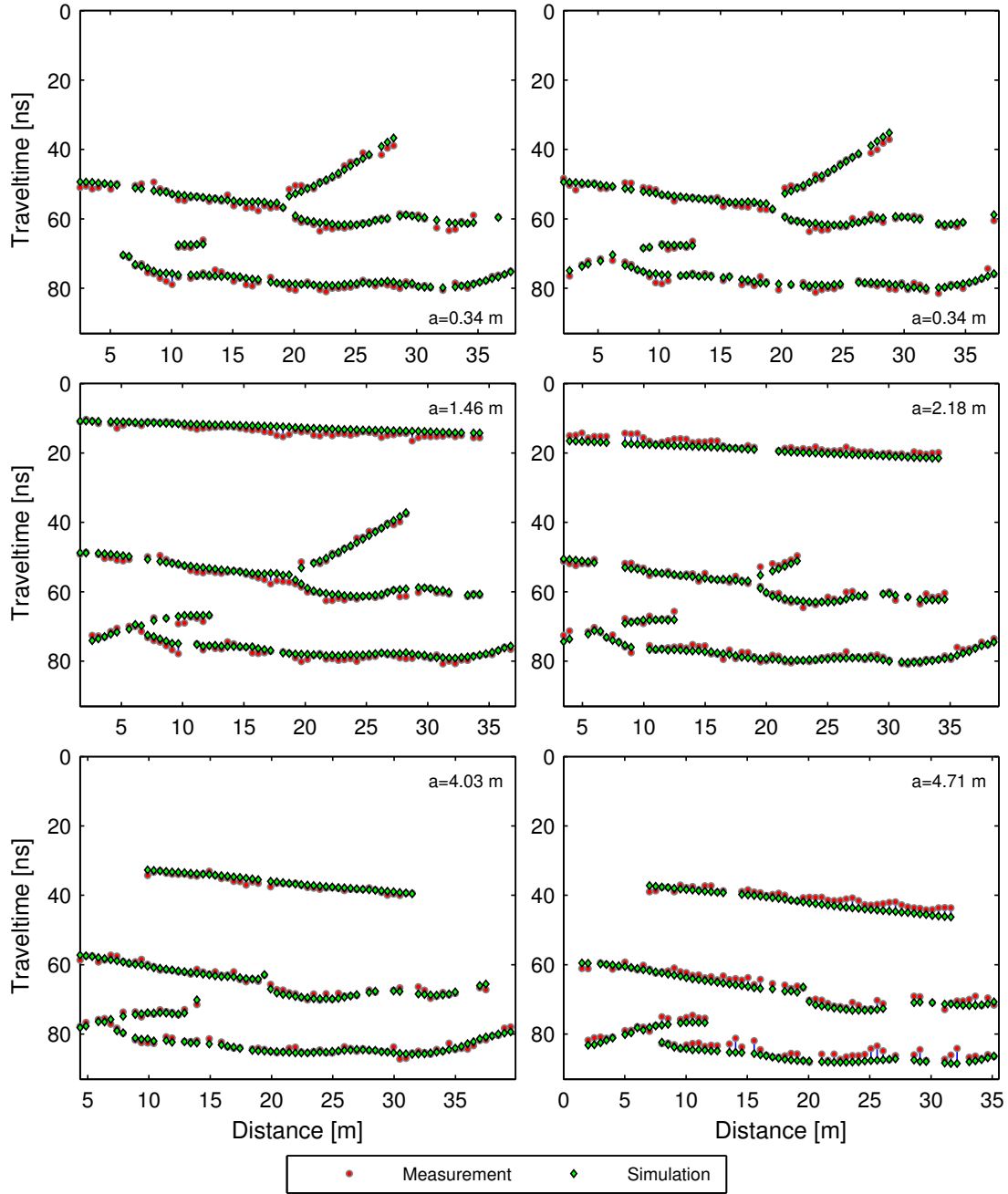


Figure 6.12: Traveltime fit for all antenna separations (lower or upper right of the graphs). The blue lines connect the traveltimes of the simulated and measurement events (same as figure 6.9), which were paired. Measured events without a partner and removed outliers are not shown.

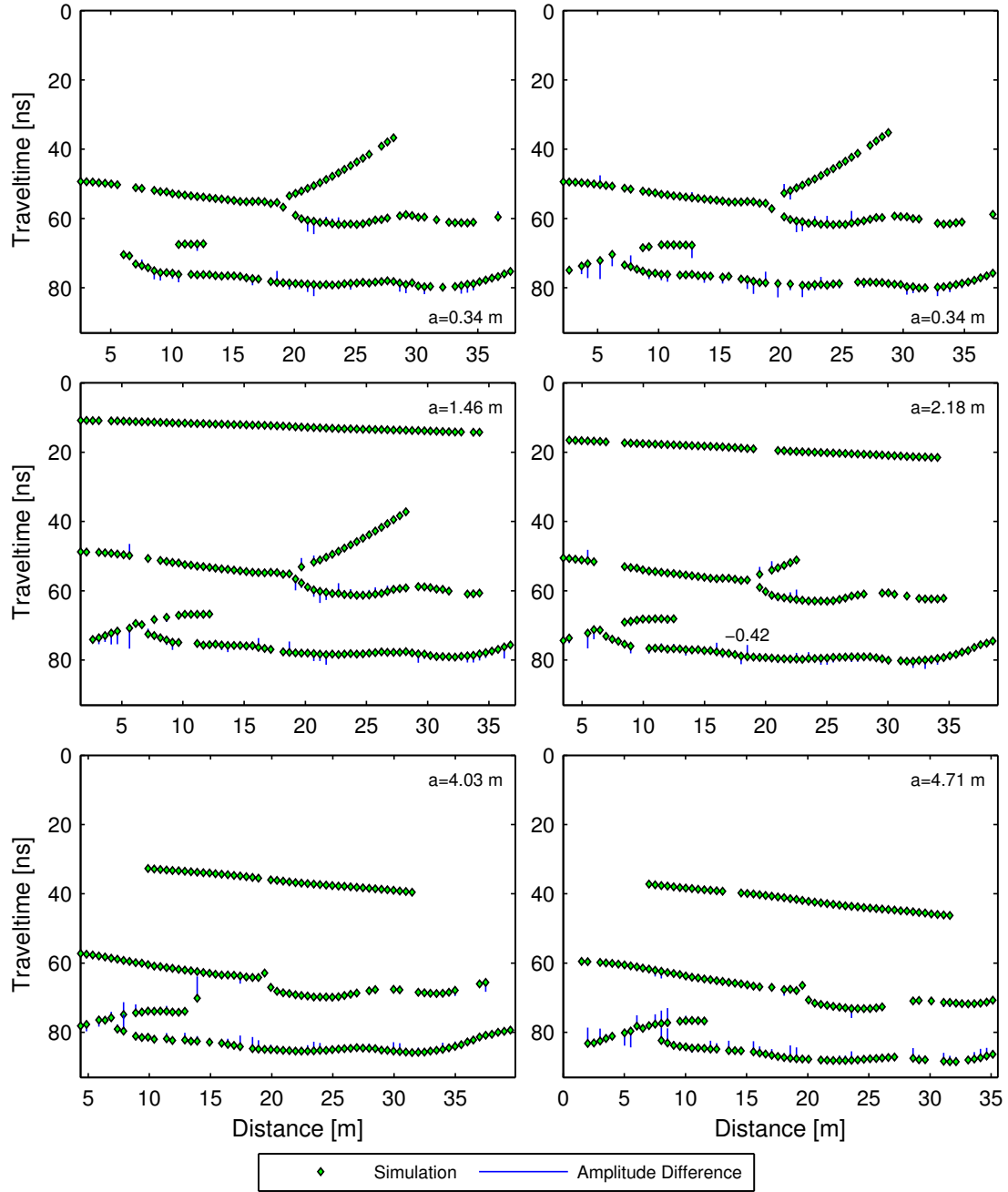


Figure 6.13: Amplitude differences for the event pairs of figure 6.12 for all antenna separations (lower or upper right of the graphs). The traveltime of the simulated events is shown while the amplitude difference to their measured partners is provided by the blue lines. The length of these lines times a factor of 0.12 ns^{-1} gives the magnitude of the amplitude difference. A reference example is given for $a = 2.18$ m at $x = 18.25$ m. The direction indicates its sign (negative time-direction means that the amplitude of the modeled event is lower than the measured one). Because of the amplitude normalization, the maximum amplitudes for each trace are equal to one and show no difference. For the events of direct groundwave the amplitudes are not employed.

In some CO sections a prominent overestimation of amplitudes by the model is given for the lowest reflections between 0 and 8 m. The reason is the sparse density of measured events corresponding to the lowest interface. Consequently, the estimation of the permittivity above and below the interface is badly determined by the data.

The estimation of altogether 48 parameters resulted in the interfaces' position and the water content distribution which are provided in figure 6.14. The water content was determined via (3.41), assuming a porosity of 0.35 and $\varepsilon_r = 5$ for the soil matrix. The temperature correction of $\varepsilon_{r,w}$ was performed after Kaatz [1989] using a measured soil surface temperature of 15 °C. The water contents for the lowest layer are deduced from amplitude information only and are thus worst determined by the data. This is manifested in the related standard deviation (2.5 % vol.), which is the largest of all layers. Especially the water contents in the middle and lower layer, between 0 and 8 m, possibly deviates from reality because of the amplitude deviations discussed above. The standard deviation of the interface position is always better than 13 cm, which is significantly larger than the ones obtained for the previous evaluation (6.8). The reason is given by the larger amount of estimated parameters (47 compared to 9), which are also estimated on the basis of less antenna separation (5 compared to 7).

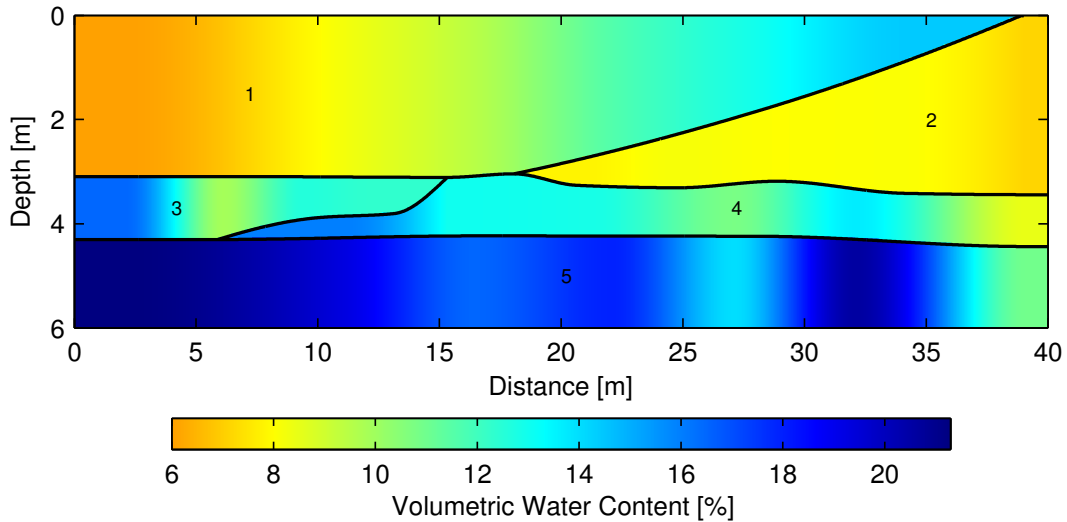


Figure 6.14: Estimated interface positions and water content distribution. The latter is given as the vertical mean in each layer, by design of the subsurface model (figure 6.10). The numbers identify the layers.

The subsurface is found in figure 6.14 to be under dry to medium-wet conditions, while spatial variations are present. For instance, layer two is dryer than layer one directly above it. This might be caused by differing hydraulic properties of the materials, that prevent water to enter layer two (as discussed in section 2.3 for the horizontal case). The explanation for the increased water content in layer three between 5 m and 15 m could be found by the decreased layer thickness in this region: The decreasing layer thickness restricts the vertical averaging distance to the lower parts of the layer. Hence, if a

vertical gradient in water content would be present throughout this layer – for instance by ponding of water at the lower interface – an increase in average water content would be observed. An equivalent situation is given for layer one between 20 m and 40 m: If the water content in the whole layer increases towards the surface, e.g., by an infiltration front, the mean water content would necessarily increase along the ascending interface. Anyways, this can be excluded in the given case since the direct groundwave data show a clear increase in traveltime in that region (figure 6.9). The direct groundwave traveltime, however, is only sensitive to the water content in the upper part of the soil, thus it should show no trend for an homogeneously distributed infiltration front.

The observed variations in water content, however, may also be explained by small scale variations of the soil’s hydraulic properties or by different dynamical effects. This shows that a reliable hydraulic interpretation is only possible if the subsurface is in a well known hydraulic state, e.g., dynamic or static equilibrium, or on the basis of a time-series measurement as investigated in the following section.

Nevertheless, the results show the inversion scheme’s ability to robustly solve the non-linear estimation problem for a large amount of unknowns (47) and to give reasonable results for a field dataset, employing a cubic-spline representation of the subsurface geometry and dielectric permittivity.

6.3 The Daheigang Time-Series

In this section, the evaluation results of a time-series of GPR measurements are discussed. The time-series was obtained in May 2011 near Daheigang village, Fengqiu County, Henan province, China [Pan *et al.*, 2012]. Located some 20 km from the Yellow River, the topography at the site can be considered to be flat at the scale of the GPR survey. During the time of year when the measurements were conducted, the local climate was dominated by the monsoon. The site is an agriculturally utilized field which was cultivated with wheat. The soil profile in figure 6.15 depicts the subsurface stratification which is qualitatively representative for the survey area, where the subsurface structure is dominated by paleo-dunes shaping the fine to coarse sand interface.

As in the previous example, a spline representation of the interface shape and dielectric permittivity was employed for the evaluation. In addition to this smoothness constraint, the interface geometry was considered to be temporally constant, in contrast to permittivity. The estimation results are compared with the results of [Pan *et al.*, 2012].

GPR Survey The survey was conducted over a period of nine days, during which GPR measurements were carried out at days 1, 4, 5, 7, and 9, covering a large area with several parallel measurement lines. For this study, however, only one of these lines is evaluated. Between day 1 and 4 a large precipitation event occurred which induced a strong increase and following decline of soil water content. The observation of these dynamics was the major objective of the survey. To provide spatial reference, the start of the GPR measurement line was marked by a wooden marker and the distance along the line was measured by the same wheel which also triggered the GPR trace recording. For the first measurement day, a GPR system with a nominal center frequency of 200 MHz was employed, while for the other four measurements a different system with 400 MHz was used. The respective trace distance was 0.11 m and 0.05 m. In both cases the GPR system consisted of two shielded bistatic GPR antenna pairs (Ingegneria dei Sistemi S.p.A.) operated in a multichannel setup. For the analysis three channels were employed, corresponding to one internal and two cross-box channels (figure 4.4). The resulting CO sections are depicted in figure 6.16.



Figure 6.15: Image of a soil profile which was dug with a minimal distance of 18 m from the GPR line. The image was stretched to provide a perpendicular point of view, which caused a stretching of the tape measure as well. The layer interfaces are indicated in addition to the soil classification of the various layers. This configuration is typical for the survey area, although the clay layer is not horizontally continuous.

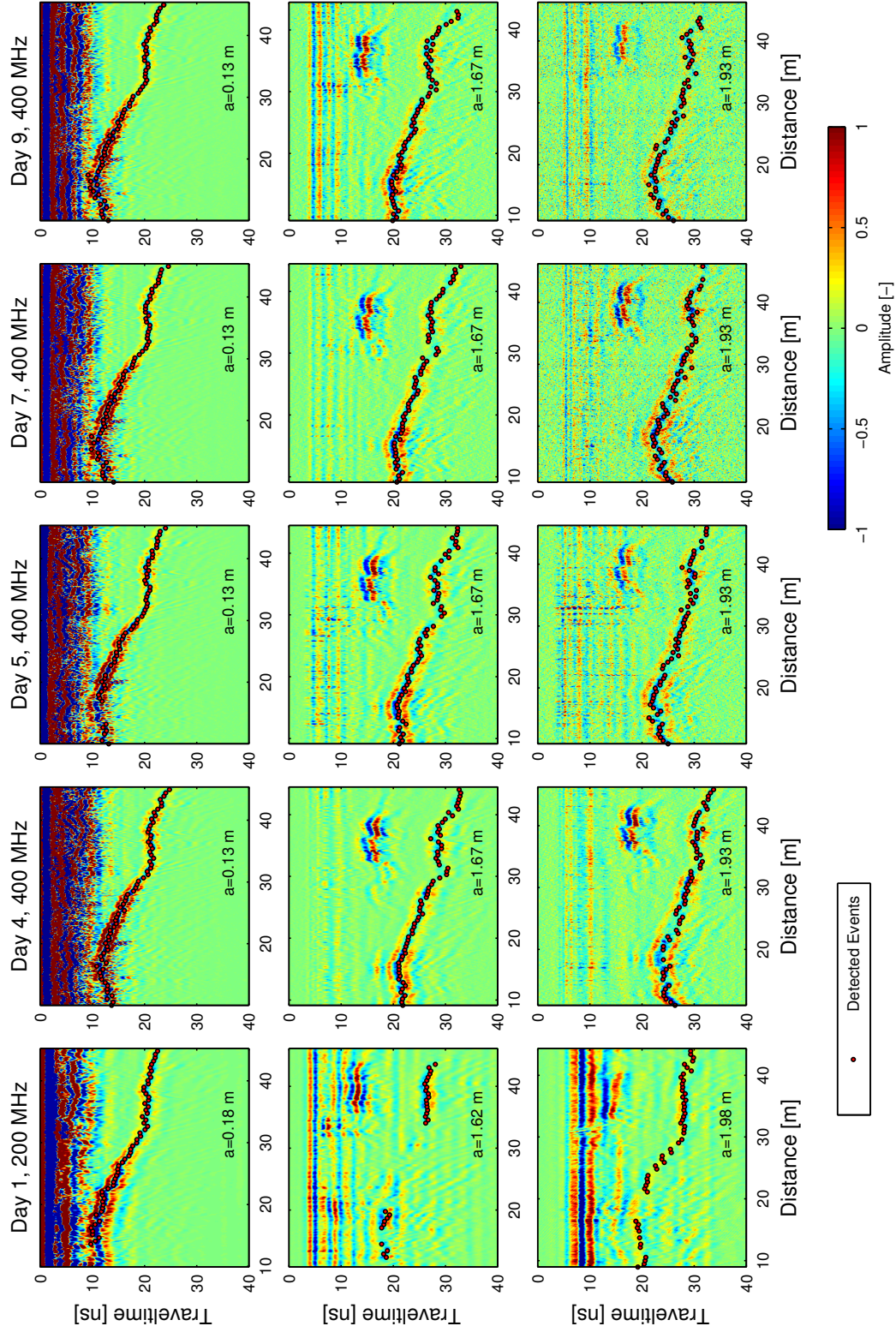


Figure 6.16: CO sections observed at the Daheigang site for different days and frequencies (rows). Each section is time-offset corrected and the imaging-points spatially referred to the coordinates of the subsurface structure. The antenna separations are provided in the lower right of each graph. The upper row and the lower two rows correspond to the internal and cross-box channels, respectively. Detected events after manual selection are shown in each section.

Inversion Scheme Setup The evaluation was carried out using the subsurface model sketched in figure 6.17. The model was constructed with the purpose to capture the spatial variability of the subsurface structure and water content at a scale of several meters. The importance of this variability for the explanation of hydrological processes, defines the upper limit of the given scale of interest. Additionally, its lower limit is defined by the precision the radar data and the necessity of a well-posed inversion problem. The latter is relevant here, because of the small number of antenna separations, which is given for this explorative survey.

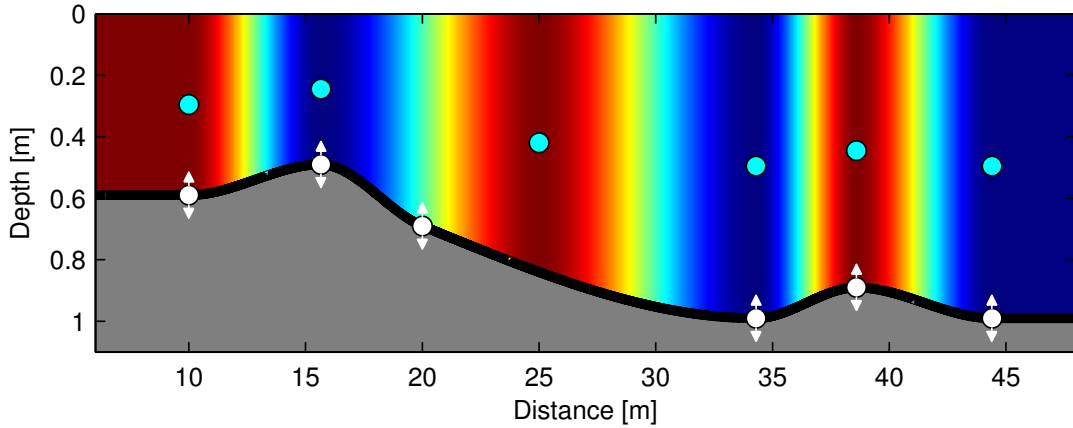


Figure 6.17: Subsurface model employed for the evaluation. White and cyan points mark the interpolation points of interface position and dielectric permittivity. Connecting the points by spline functions, interface position (black line) and vertical mean permittivity are obtained (color). The color variations represent the shape of the spline functions of permittivity with arbitrary absolute values. The interface was assumed to be temporally invariant in contrast to permittivity. The permittivity of the grey area was not estimated.

The subsurface model was constructed by setting several interpolation points for the layer interface position as well as the magnitude of vertical mean dielectric permittivity, in the region covered by the GPR measurements. The interpolation points were connected with monotonic cubic piecewise spline functions, i.e., similar as described in section 6.2. Using cubic spline functions inherently assumes that the spatial variation is first order continuous. Concerning water content this is a meaningful assumption, since it coincides with the smoothness of the solution to Richards equation (2.4) in a homogenous medium. For the layer interface it also appears to be reasonable, at least at the scale of interest. The GPR survey was conducted over a time-period in which water content changes are expected, due to the precipitation event, but variations of the subsurface structure can be excluded for the observation period. This crucial assumption was implemented into the subsurface model by restricting temporal variations to the permittivity with the aim to provide an explanation of the events' traveltime changes (figure 6.16) over time. This way six geometrical parameters and 30 permittivity parameters were estimated during the evaluation. For this purpose, these parameters were allowed to vary in vertical position and permittivity magnitude, respectively. For the parameter estimation, again, $\sqrt{\varepsilon_r}$ was employed instead of ε_r .

Table 6.5: Gaussian filter width σ_G and standard deviation of measured traveltimes σ_t for the different days and antenna separations a .

	Day 1			Day 4			Day 5		
a [m]	0.18	1.62	1.98	0.13	1.67	1.93	0.13	1.67	1.93
σ_G [ns]	1.17	1.25	1.25	0.88	1.37	1.17	0.94	1.25	1.41
σ_t [ns]	0.38	0.30	0.24	0.33	0.71	0.54	0.32	0.69	0.76

	Day 7			Day 9		
a [m]	0.13	1.67	1.93	0.13	1.67	1.93
σ_G [ns]	0.86	1.25	1.56	0.86	1.25	1.25
σ_t [ns]	0.30	0.31	0.60	0.35	0.55	0.70

The Gaussian filter width had to be determined for each day and antenna separation (table 6.5), since the different channels and frequencies were employed and the measurement setup was reinitialized for each day. Each value was determined from a representative reflection wavelet. This leads to obvious variations of σ_G in table 6.5, mainly due to the variability of the wavelets' shapes for different traces. Employing σ_G for the feature detection procedure described in section 5.3.3, the events of the direct wave, which was observed when emitting the antennas in air while tilting them, were detected. From this the time-offset was determined.

Similarly, the events in the CO sections were detected and the ones indicated in figure 6.16 were manually selected for further analysis. These events stem from the continuous interface between coarse and fine sand (figure 6.15) and are of main interest here. At day 1, several events are missing for $a = 1.62$ m because of bad signal quality. In the upper part of the radargrams, reflections from a clay inclusion are visible between 35 to 45m. These are hardly visible for the internal channels since they interfere with the direct signals. However, these reflections are not present throughout the complete sections. This is coherent with the finding that the clay inclusions are not continuous over the whole site and either are extended perpendicular to the measurement line or are only small lenses. The high intensity of the reflections indicate a strong contrast in dielectric permittivity, possibly due to a high water content in the clay. Since the main interest of this evaluation was not on the clay inclusions, the corresponding events were not considered, which is equivalent to incorporating the clay inclusions into a vertical mean representation of permittivity. Effects on amplitude also don't have to be accounted for, since only one reflection per trace is available for the normalization and hence amplitude information could not be exploited.

Direct groundwave signals are not reliably available for most of the sections either since they are too weak or because they interfere strongly with the direct air wave, as for the internal channel data. However, a strong direct groundwave signal is present for $a = 1.98$ m at day 1. This is due to a different ground coupling of the antennas since they were applied without removing the wheat, in contrast to the following measurement days. In addition, dryer soil conditions also increase the signal intensity; in contradiction to the weak direct-groundwave for the shorter antenna separation of $a = 1.62$ m. This

can be explained by the generally smaller signal intensity of the transmitter-receiver combination employed for this CO section.

Table 6.5 also provides the standard deviations of the traveltimes, which were employed for the inversion procedure. They were deduced from flat parts of the interface reflections.

The measurement simulations were carried out by solving Maxwell's equations in 2D on the domain given by the subsurface model with an additional vacuum layer of 1 m thickness. This again neglects changes of the subsurface properties perpendicular to the measurement line. Electric conductivity and the imaginary part of ε_r were not included in the evaluation since amplitudes were not considered. Dispersive effects by the influence on the signals' velocity (equation (3.17)) are assumed to be negligible because of the given strength of the signal. The spatial resolution and the Courant number was set to 0.0125 m and 0.5, respectively. To decrease computation time the trace spacing was increased to 0.53 m which is equal to the spacing of the events in figure 6.16. The simulated events corresponding to the interface were detected with $\sigma_G = 1.1$ ns and $\sigma_G = 0.5$ ns for the Ricker wavelets with a nominal frequency of 200 MHz (day 1) and 400 MHz (other days), respectively. By setting the $\varepsilon_r = 25$ for the lower layer the reflection from the interface had sufficient intensity to be detected without using a noise-level threshold and to uniquely distinguish it from the direct groundwave signal.

The inversion procedure was initialized by setting $\sqrt{\varepsilon_r} = 2$ for all days and assuming the interface shape to be similar to the expected one.

Estimation Results Figure 6.18 shows the fitting results, which were obtained by the inversion procedure. The results are judged to be satisfying; especially for the smallest antenna separations the measured and simulated traveltimes match well. In contrast, larger systematic deviations are found for some of the longer antenna separations. Both findings have to be interpreted on the basis of the standard deviations which were determined for the different sections (table 6.5). The best fits for each day are obtained for the sections with the smallest standard deviations, which is determined by the weighting in the objective function (5.10). The systematic deviations, however, can be explained if an traveltime shift is given for individual sections, which cannot be described by the forward model. Hence, the shift is balanced out between different sections for each day, e.g., day 5. There, the traveltimes fit well for $a = 0.13$ m, but are underestimated for $a = 1.67$ m and overestimated for $a = 1.93$ m. Such a temporal shift is most likely due to an erroneous time-offset determination, which is performed section specific. Unfortunately, there was no reliable correction for the time-offset determination available. In addition to that, there are also local deviations of the traveltime for $a = 1.67$ m at day 4, 5, and 9 around 30 m and 42 m, where the measured traveltimes are significantly larger than the simulated. However, figure 6.16 reveals a disagreement of the result for $a = 1.67$ m compared the other two antenna separations, with respect to the evolution of the traveltimes along the distance. This disagreement, cannot be reproduced by the forward model. Consequently, the fit will be better for the two CO sections which agree, since they contribute about two times more terms to the objective function (5.10).

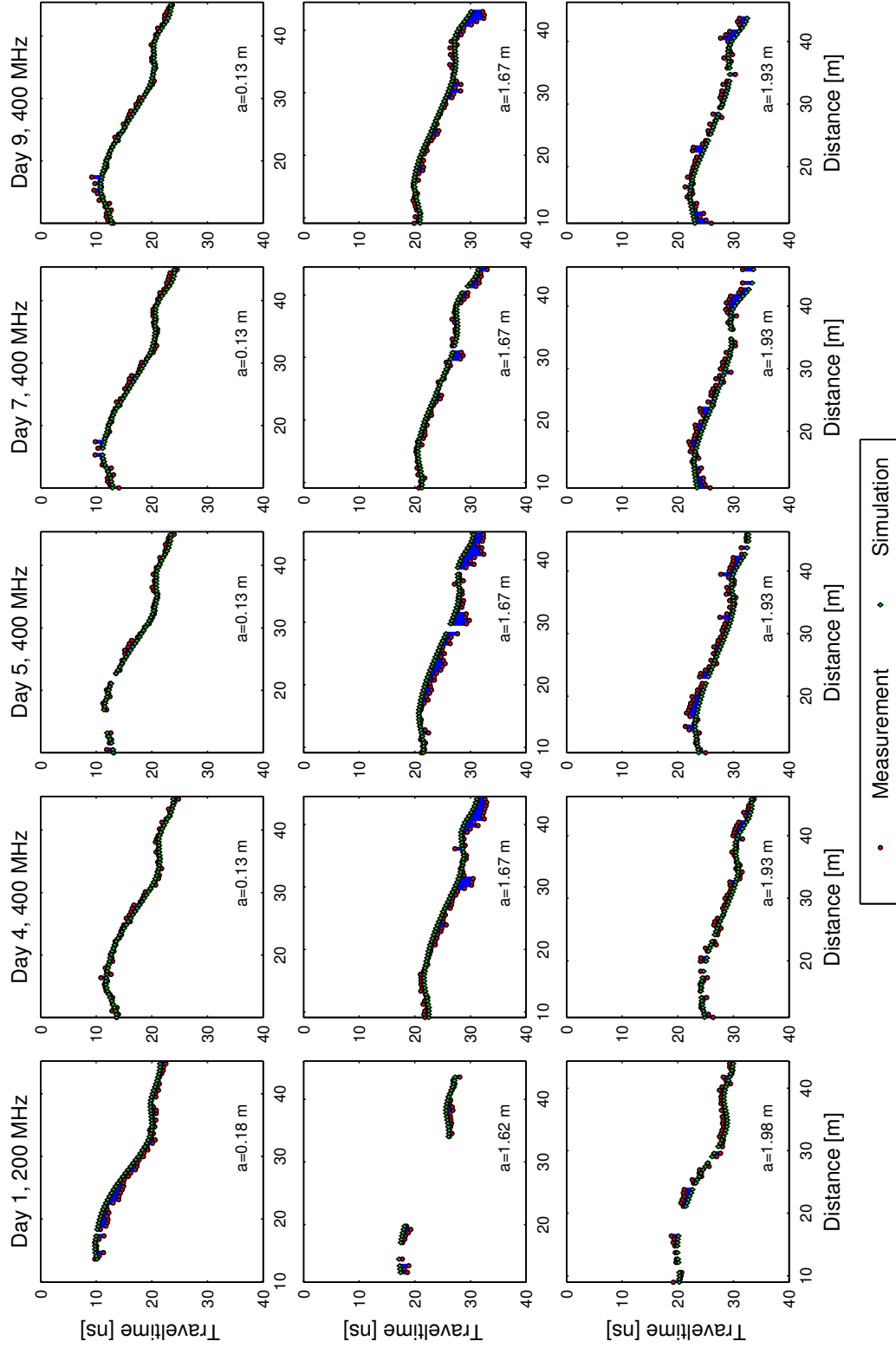
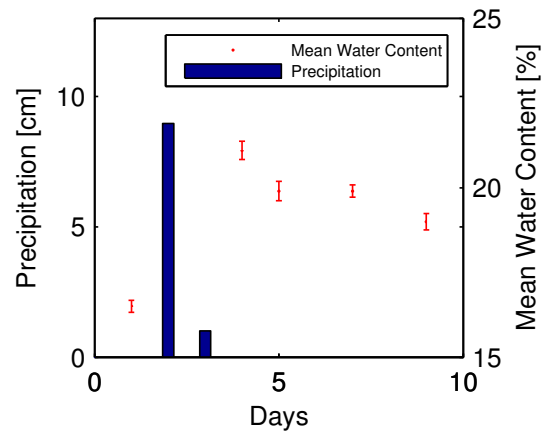


Figure 6.18: Fit obtained for the final iteration after 24 successful parameter updates for the different days and antenna separations (lower right of each graph). The red symbols mark the measured events which are also provided in figure 6.16. The simulated events which are associated with measured ones (indicated by the blue lines) are given by the green symbols.

The results for the interface position and water content are depicted in figure 6.20. The water content was retrieved from dielectric permittivity via (3.41) assuming a porosity of 0.45 and $\varepsilon_r = 5$ for the soil matrix. The temperature correction for ε_r of water [Kaatze, 1989] was performed assuming a soil temperature of 20 °C for all days. These results and the fit quality, discussed above, show that the chosen interpolation point density is appropriate to describe the spatial variability at the scale of several meters. As assumed, the interface structure is temporally stable, while the water content shows significant variations over space and time. At day 1, the soil is relatively dry, while a strong increase in water content can be found for the next measurement day. In the following three days the water content decreases steadily, at most on the left hand side. As already mentioned, the reason for the temporal variation is the precipitation event (figure 6.19). It caused the strong increase in water content between the first two measurement days. The corresponding difference in the total water content (table 6.6) is 3.72 cm, which is significantly smaller than the input by precipitation (9.98 cm). This deviation is most-likely a combined effect of evapotranspiration, drainage at the lower interface, and lateral water flux. All these processes could also be responsible for the decrease of water content in the following days.

For all measurement days a minimum in water content is present between 35 and 40 m. This coincides with the position of the clay inclusion observed in the radar data in figure 6.16. The hypothesis for the presence of the water content minimum is that the clay inclusion prevents water to enter the volume below it. This is due to the smaller hydraulic conductivity, which is expected from the smaller dominant grain-size fraction. Thus, water ponds on the clay after the precipitation event. In the following days that water is redistributed to all sides. Hence, the water content above the clay decreases and consequently also the vertically averaged water content. However, from that explanation one would expect a local maximum of water content to the left and right of the clay inclusion. Hence, the water either dominantly drains out of the observation plane or evaporates at the surface.

Figure 6.19: Mean water content in the observed subsurface volume and precipitation measured 3 km away from the site. The errorbars of mean water content represent the largest standard deviation of all estimated water content values, while the precision of the precipitation data is 0.01 cm. The explanation for the almost equal water contents at day 5 and 7 is the decrease of water content at day 7 for almost the complete measurement line (figure 6.20) which is compensated by a strong increase around 45 m.



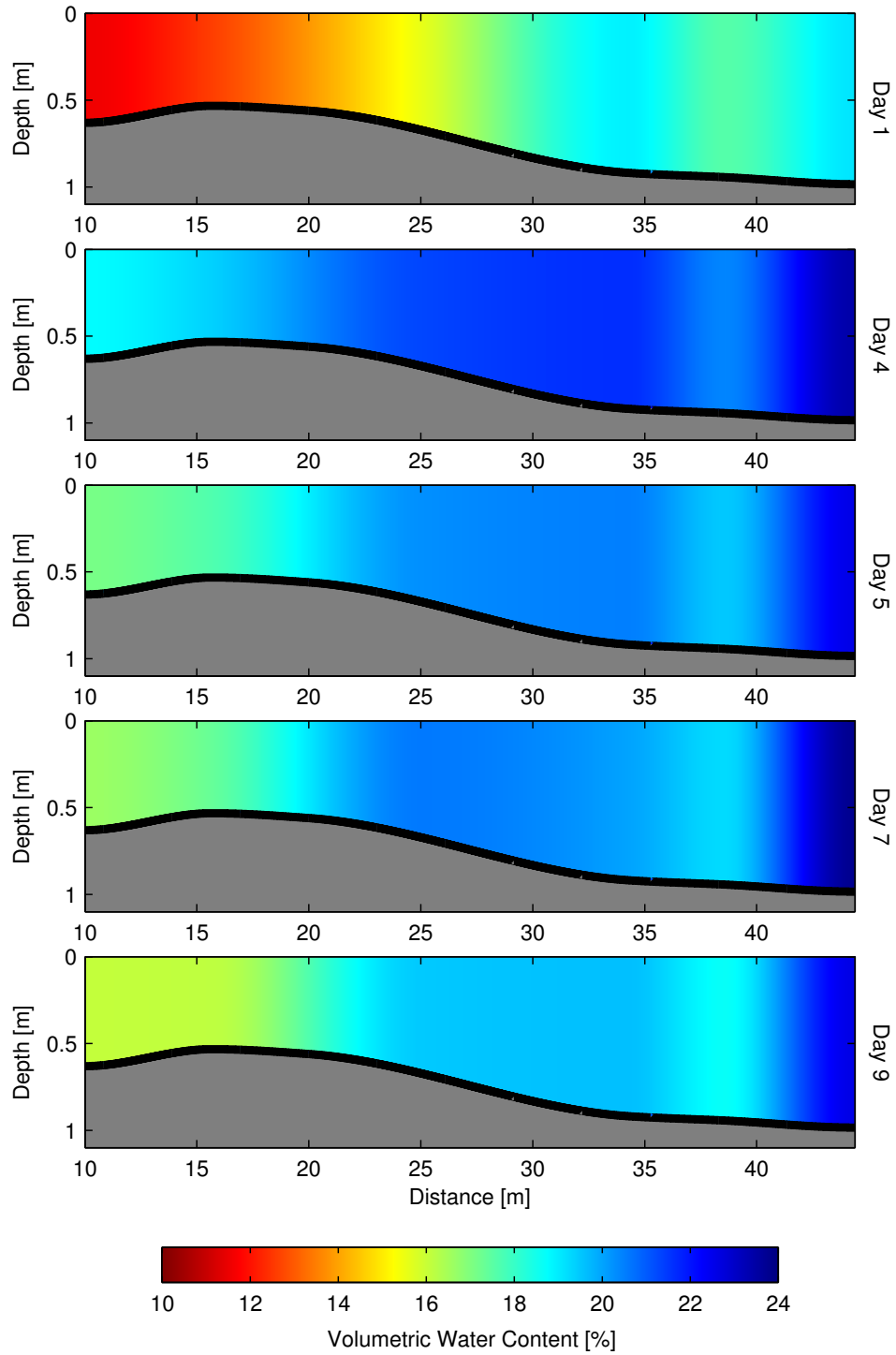


Figure 6.20: Estimation results for interface position and water content (vertically averaged) for the different measurement days. The volumetric water content in the grey area was not accessible with the amplitude information of only one reflection per trace.

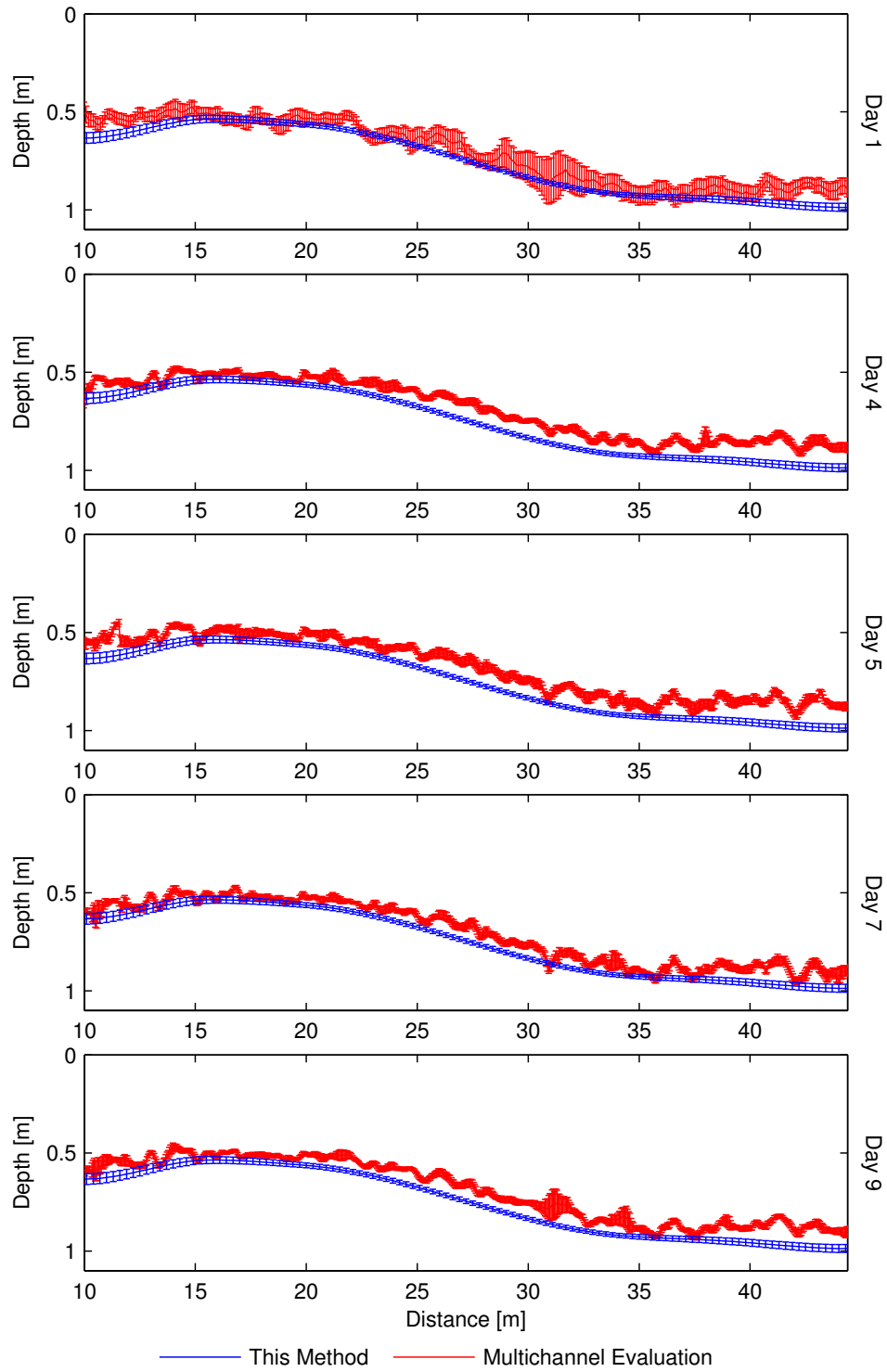


Figure 6.21: Results for interface position of this method and the multichannel evaluation method applied by *Pan et al. [2012]* for the different days. The errorbars represent the 68.3 % confidence intervals obtained from each parameter estimation procedure.

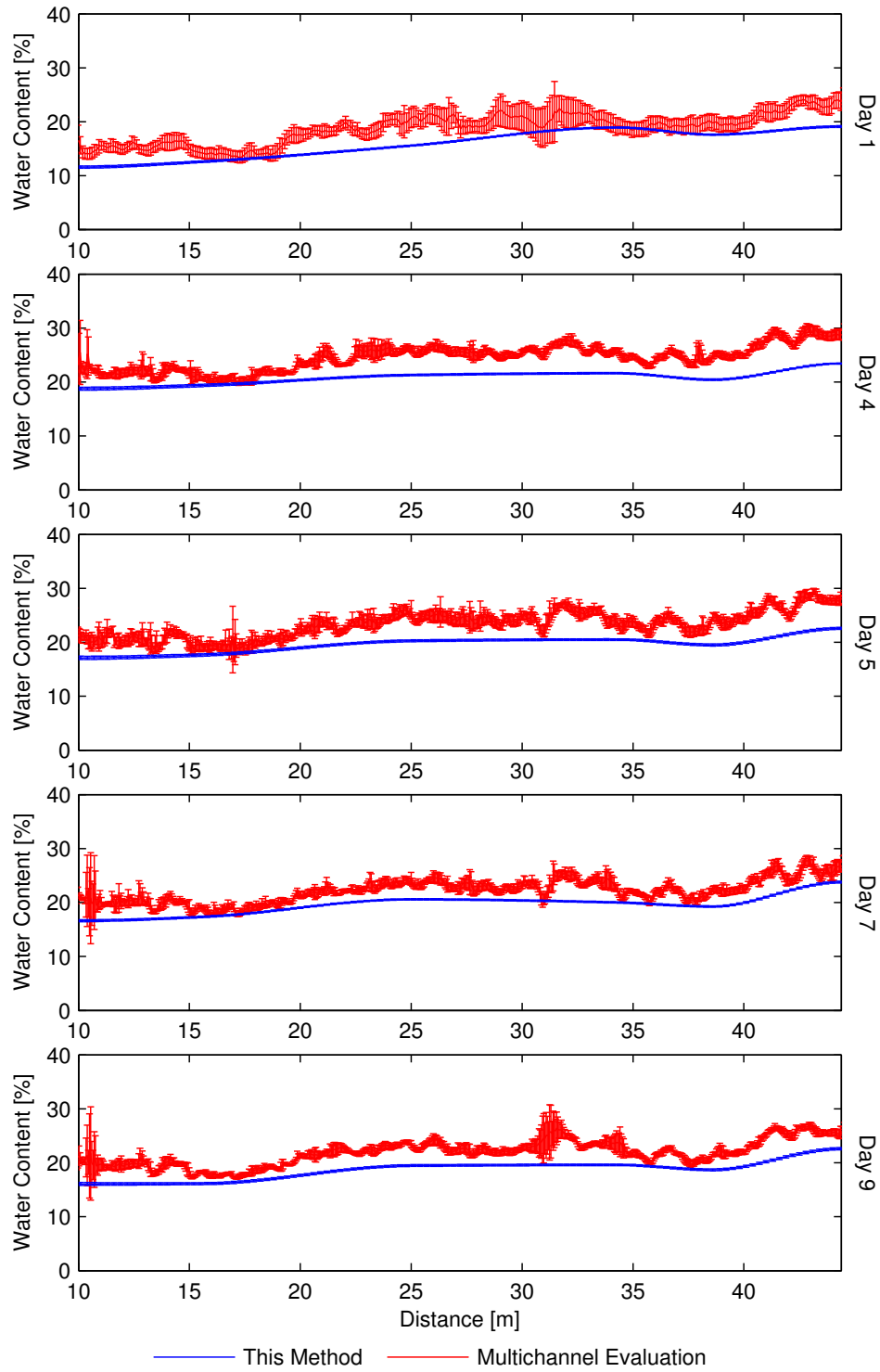


Figure 6.22: Results for vertical mean water content corresponding to the interface positions depicted in figure 6.21. The errorbars represent the 68.3 % confidence intervals obtained from each parameter estimation procedure.

The question how the given method compares with the multichannel evaluation method of [Gerhards et al. \[2008\]](#) is addressed in the following. This method was applied by [Pan et al. \[2012\]](#) to obtain the results which are presented in figure 6.21 and 6.22. Although both methods show a similar trend, there are systematic deviations in both, interface position and water content. These are not explained by the estimated confidence intervals. Additionally, the confidence intervals do not represent the spatial variability of the multichannel evaluation results. This variability is likely caused by an anti-correlation of interface position and water content, which can be found when comparing local extrema of the two. The anti-correlation, however, could also explain the systematic deviations: If the systematically smaller depth of the interface is compensated by a higher water content, the two methods could coincide for the total water content. Thus, one would expect the total water content to be the same for both methods which is, however, not the case (table 6.6).

Table 6.6: Total water content calculated from interface position and vertical mean water content for the multichannel evaluation method (column 2) and this method (column 3).

Days	$\theta_{tot,mc}$ [cm]	$\theta_{tot,this}$ [cm]
1	15.72	12.13
4	19.36	15.85
5	18.40	14.96
7	17.97	14.96
9	17.45	14.30

Various studies [[Kühne, 2010](#), [Bogda, 2011](#), [Buchner et al., 2011](#)] reported systematic deviations and parameter correlations, when comparing the results of multichannel evaluation method to the geometry of the ASSESS-GPR site. In summary, the relevant reasons are: (i) Biased time-offset estimates because of wavelet deformations caused by ground-coupling. (ii) Simplifications of the measurement process by using ray-tracing for locally flat but dipping interfaces. (iii) A large number of parameters are estimated (three for each trace position) which increases the estimation uncertainty of each parameter and can be shown to introduce the anti-correlation mentioned above. (iv) Surface roughness, which causes the antennas to rotate and thus introduces an apparent dipping of the interface.

These issues are addressed by the given method with (i) Using a more robust time-offset estimation based on the center of intensity and not on individual wavelet features, (ii) a more detailed representation of the measurement process by solving Maxwell's equations, (iii) significantly less parameters (36 for all days), and (iv) by introducing a scale of interest and the smooth spline functions. Hence, the small scale variability of traveltimes is inherently treated as statistical variations.

While the given method resolves the above issues, it has the major drawback of significant computations times (section A.3). Especially for this dataset, the combined inversion of all measurements also involves the large number of 24 parameter updates, even though only one layer is considered. The reason is that the simulated data of all days depend on the interface position. For instance, if a fit is optimal for four days but strong deviations are given for one single day, this causes the adjustment of the permittivity for that day and of the interface position as well. As long as the next parameter update does not cause the inversion to terminate, additional corrections of

the permittivities, at least for some of the other days, are necessary. This would not be the case if the interface position is estimated independently for each day, hence the given estimation problem has a higher degree of nonlinearity from a qualitative perspective.

A disadvantage of both employed methods is, that only vertical averages of water content are retrieved. This could be circumvented on the basis of additional information obtained from different raypaths, as for examples given in borehole measurements. Hence, a well determined estimation of smooth vertical changes of permittivity is only feasible with the given approach and measurement setups, if these changes cause reflections (section 3.5). To exploit these reflections, however, some modifications of the feature identification technique would be necessary, to account for the modifications of the wavelet shape.

The inversion of the Daheigang time-series of GPR measurements with the constructive approach shows acceptable results, considering the systematic errors of the measurement device. The estimated water content distribution and its temporal evolution enables a reliable but limited hydraulic interpretation. The general trend of the water content evolution can be explained with the aid of precipitation data, while a quantitative deviation in total water content is likely due to evapotranspiration, drainage losses, and lateral flux. In comparison to the multichannel evaluation method (section 4.4.3), the given method is able to resolve the major problems of the former by representing the subsurface setting by cubic spline functions. The latter step is a rigid regularization, which makes the inversion problem better posed and introduces a scale of interest of several meters with which small scale variations can be treated as statistical variations. Additionally, the spline representation incorporates assumptions on the smoothness and spatial correlation of each, structure and dielectric permittivity, which are reasonable on this case. For the given evaluation, the assumption of a static subsurface structure is included. This provides, in combination with the actual subsurface model, an appropriate interface to directly include a hydraulic model into the inversion procedure.

7 Summary and Conclusions

The headstone of this thesis is the constructive inversion, which was conceptually introduced by *Buchner et al.* [2012]. The method's principle of operation is the inversion of data, describing the response of a measurement device when observing an object. The method's purpose, however, is to determine the object's structure and other properties which are of interest. At the core of the constructive inversion approach stands the design of a model, which represents the observed object and provides a parameterization of its structure as well as its properties. This model is employed to simulate the measurement process itself. By a quantitative comparison of the simulated and measured response, an objective function is defined, whose minimization allows to estimate the model parameters.

The constructive inversion method was used to evaluate multi common-offset surface GPR data, with the aim to determine the subsurface' structure and water content distribution. The evaluation of surface GPR data, using an explicit parameterization of these quantities in combination with a complete representation of the subsurface, is new in its kind – to the best of the author's knowledge. The inversion was realized with a model of the subsurface, representing the structure and dielectric permittivity distributions by parametrized functions. Two-dimensional FDTD solutions to Maxwell's equations were employed to simulate the GPR measurement process, on the basis of the subsurface model. A feature detection procedure was used to automatically detect events in the simulated and measured signals. This procedure relies on the convolution of the absolute signal with a Gaussian filter and provides traveltime and amplitude for each event. By heuristically associating the measured and simulated events with each other, the objective function was defined: the summed squared difference of the event's traveltimes and amplitudes. By its minimization the subsurface parameters were estimated. The water content distribution was calculated from dielectric permittivity via a petrophysical relationship.

At the core of the above approach is the construction of the subsurface model, which is designed by the user on the basis of the given data. By adding several parameters to it, this model is flexible albeit limited by its design, e.g., with assuming local monotonicity by employing suitable spline functions for the interface representation. This leads to an adjustable regularization of the inversion process which allows to focus on relevant data and to introduce a scale of interest by choosing the spatial density of parameters. Additionally it allows to include assumptions based on knowledge about the observed object, e.g., a temporally constant structure.

Altogether, four datasets were analyzed with the intention (i) to test if the method is suitable to evaluate surface GPR datasets, (ii) to investigate its performance and accuracy, (ii) to demonstrate its applicability to field data, and (iv) to observe the water dynamics by analyzing a time-series of measurements.

For the first two datasets, the ASSESS-GPR testbed was employed, which is an artificial and partially saturated sand volume comprising a well-defined layer geometry with characteristic and complicated features. It provides ground-truth information on the geometry as well as on dielectric permittivity and accordingly water content. A synthetic dataset was generated similar to a real one, which was measured on the testbed. The evaluation of the former confirms that the method is able to robustly solve the parameter estimation problem and that the true parameters can be recovered within the confidence limits. A comparison of the evaluation results from the real dataset with the ground truth data showed (i) that the estimated geometry corresponds to the in-situ measurements almost everywhere within ± 5 cm and (ii) a difference in the water content which is not larger than 2 % vol., for the layers where traveltime information was exploited in addition to amplitude.

The third dataset was recorded in the context of the work of [Schneider \[2007\]](#) at a field site with a complex subsurface setting. Hence, cubic monotonic spline functions were employed to represent the structure and dielectric permittivity distribution, allowing for its horizontal variability but only providing vertical averages per layer. The parameters to be estimated were then given by the values at the interpolation points. By choosing the density of interpolation points, a scale of interest of several meters was introduced. This involved an increase of the number of parameters to be estimated by a factor of five, compared to the previous case. The estimation problem could still be solved by the employed Levenberg-Marquardt scheme and reasonable results were found for structure and water content. This enabled a rudimentary hydraulic interpretation, which is, however, limited without further knowledge of the system state and boundary conditions.

The previous issue was resolved for the fourth dataset which consists of a time-series of five measurements. These are part of a larger exploration [[Pan et al., 2012](#)], which was conducted with the aim to observe the subsurfaces response to a strong precipitation event. For its evaluation, again cubic spline functions were employed for the subsurface model. To account for the dynamics of water, the dielectric permittivity was allowed to vary while the structure was assumed to be constant over time. The forcing of the system by precipitation was recaptured by the retrieved water dynamics, while a quantitative deviation between the total water content and the precipitation records could be explained by the loss of water by evapotranspiration, drainage, and lateral fluxes. A comparison with the multichannel evaluation method demonstrated that the constructive inversion method is able to resolve the major problems involved with the latter.

It is concluded that the constructive inversion approach, in its given application, provides accurate and overall reliable information on subsurface structure and water content. This holds, besides for the evaluation at the ASSESS-GPR testbed also for the two field datasets which show worse data quality and were recorded with less antenna separations. Exceptions with respect to reliability are indicated by the fitting results and involve little interpretation. A benefit of the method is that it employs a model of the subsurface representing its properties, hence the results are provided in the same manner and not at single locations. By numerically solving Maxwell's equations to simulate the GPR measurement process, the direct groundwave and reflected waves can be employed

by an intrinsic inclusion of relevant electromagnetic effects. This also enables to exploit amplitude information in addition to signal traveltime, which gives access to additional information on the lowest layers. The major drawback of the given implementation is the high computational effort which is involved. This, however, could be circumvented by employing alternative methods which simulate the measurement process, e.g., wavefront propagation techniques, with accepting the implied simplifications.

Recalling the five requirements to measurement methods which observe soil moisture, the employed GPR evaluation technique addresses the first three of them: (i) the spatial distribution and temporal evolution of water content, (ii) accurate water content information, and (iii) the subsurface stratification. The method does not provide information on the boundary conditions – the fourth demand – but other standard measurement techniques are already available for this purpose.

The fifth requirement, which is a characterization of the hydraulic properties of the subsurface's materials, is not directly be addressed by the method. However, it does not only provide a distribution of water content, but also gives access and control on the structure of the subsurface. This is well suited to directly include a model describing the water dynamics. While maintaining the parametrization of the interface geometry, the parameterization of the electromagnetic parameters could be transferred to the level of hydraulic parameters. Hence, an estimation of the latter could be attempted and even improved by a combined constructive inversion of data retrieved from other measurement techniques.

The concept of constructive inversion is in general not limited to geophysical measurement techniques and could be applied even beyond.

A Appendix

A.1 Additional Figures and Tables



(a) Gravel layer placed in the concrete cuboid which is covered with foil. The pumping tube is shown in back left.



(b) First sand layer with a TDR and CS616 probe installed in the foreground. In the back one finds a white geotextile and the plate vibrator used for compaction.



(c) Manual measurement of the layer geometry.



(d) Top view at the end of construction.

Figure A.1: Different stages of the construction of the ASSESS-GPR site.

Table A.1: Textural composition given in gravimetric fractions [%] of the different sands (first row) built into the ASSESS-GPR site as indicated in figure 6.2. The first column contains the grain size fractions. For sand B, two samples were investigated and shown in column three and four. The occasional significant differences demonstrate that the sand samples are only representative to show trends in the textural composition of the sands.

	A	B – 1	B – 2	C
[0, 2) μm	0.06	0.02	0.09	0.04
[2, 6.3) μm	0.20	0.01	0.18	0.07
[6.3, 20) μm	0.27	0.03	0.23	0.08
[20, 63) μm	0.34	0.07	0.31	0.18
[63, 200) μm	22.05	7.61	7.44	6.18
[200, 630) μm	65.31	63.90	67.96	71.53
[630, 2000) μm	9.62	23.66	19.97	17.26
[2, 6.3) mm	2.15	4.54	3.82	4.66
[6.3, 20) mm	0.00	0.16	0.00	0.00

A.2 The Ricker Source Current Density Function

For the given study the Ricker source current density function with an antenna at \vec{x}_0 pointing in direction \vec{y} is defined as

$$\vec{j}(t, \vec{x}) := -2j_0\delta(\vec{x} - \vec{x}_0)\zeta\sqrt{e^{1/2}\zeta}e^{-\zeta(t-\chi)^2}(t - \chi)\frac{\vec{y}}{|\vec{y}|} \quad (\text{A.1})$$

with j_0 being a charge length [C m], $\zeta = \omega^2/2$, $\chi = 2\pi/\omega$, and ω denotes the nominal angular frequency. Figure A.2 shows the time-dependency of the function.

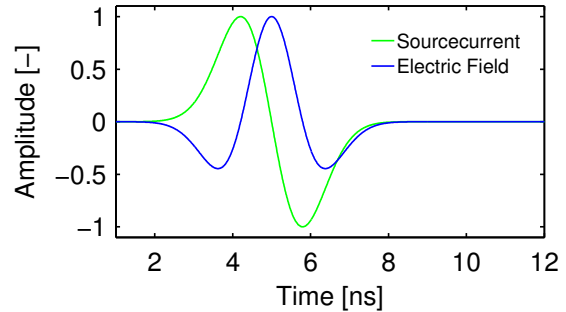


Figure A.2: Time dependency of the Ricker source current density function and the corresponding electric field obtained from (3.33) in the far field. The curves are obtained with $\omega = 2\pi * 200$ MHz and are normalized to their maximum amplitude.

A.3 Computational Aspects

The implementation of the inversion scheme was done in C++ combined with Octave. The computations were carried out in parallel on the bwGRiD cluster (<http://www.bw-grid.de>), member of the German D-Grid initiative, funded by the Ministry for Education and Research (Bundesministerium für Bildung und Forschung) and the Ministry for Science, Research and Arts Baden-Württemberg (Ministerium für Wissenschaft, Forschung und Kunst Baden-Württemberg). The parallelization was implemented by splitting the computation of the CO sections, i.e., for a given number of processes np and M traces, each process computes np/M traces. The traces of each process are next to each other, which permits to reduce the domain size accordingly. The CO sections for different antenna separations were computed all-at-once, by shifting them to a common transmitter position.

Concerning the Daheigang time-series, the permittivity parameters of one day do only influence the results of that day. This was accounted for when assembling J and reduced the computation time for that parameters approximately by a factor of five.

The computation times for all evaluations are given in table A.2.

Application	# Processes	Time [h]
ASSESS-GPR synthetic (section 6.1.3)	112	7.5
ASSESS-GPR real (section 6.1.4)	224	6.8
Hirschacker (section 6.2)	71	108
Daheigang (section 6.3)	72	50

Table A.2: Computation time for the different evaluations.

Bibliography

- Annan, A. P. (1973), Radio interferometry depth sounding: Part I – theoretical discussion, *Geophysics*, 38(3), 557–580, doi: [10.1190/1.1440360](https://doi.org/10.1190/1.1440360).
- Archie, G. E. (1942), The electrical resistivity log as an aid in determining some reservoir characteristics, *Transactions of the American Institute of Mining, Metallurgical and Petroleum Engineers*, 146(99), 54–62.
- Balanis, C. A. (Ed.) (1997), *Antenna theory*, 2nd ed., Wiley, New York.
- Beljaars, A. C. M., P. Viterbo, M. J. Miller, and A. K. Betts (1996), The anomalous rainfall over the united states during July 1993: Sensitivity to land surface parameterization and soil moisture anomalies, *Monthly Weather Review*, 124(3), 362–383.
- Bettenay, E., A. V. Blackmore, and F. J. Hingston (1964), Aspects of the hydrologic cycle and related salinity in the Belka valley, Western Australia, *Australian Journal of Soil Research*, 2(2), 187–210.
- Bleistein, N. (1986), Two-and-one-half dimensional in-plane wave propagation, *Geophysical Prospecting*, 34(5), 686–703, doi: [10.1111/j.1365-2478.1986.tb00488.x](https://doi.org/10.1111/j.1365-2478.1986.tb00488.x).
- Bogda, F. (2011), Untersuchung der Bodenwasserdynamik mit Mehrkanal-GPR, Staatsexamensarbeit, Heidelberg University.
- Bronstert, A., and E. J. Plate (1997), Modelling of runoff generation and soil moisture dynamics for hillslopes and micro-catchments, *Journal of Hydrology*, 198(1-4), 177–195, doi: [10.1016/S0022-1694\(96\)03306-9](https://doi.org/10.1016/S0022-1694(96)03306-9).
- Brovelli, A., and G. Cassiani (2008), Effective permittivity of porous media: a critical analysis of the complex refractive index model, *Geophysical Prospecting*, 56(5), 715–727, doi: [10.1111/j.1365-2478.2008.00724.x](https://doi.org/10.1111/j.1365-2478.2008.00724.x).
- Brovelli, A., and G. Cassiani (2010), A combination of the Hashin-Shtrikman bounds aimed at modelling electrical conductivity and permittivity of variably saturated porous media, *Geophysical Journal International*, 180(1), 225–237, doi: [10.1111/j.1365-246X.2009.04415.x](https://doi.org/10.1111/j.1365-246X.2009.04415.x).
- Brutsaert, W. (2005), *Hydrology: An introduction*, Cambridge University Press.
- Buchner, J. S., A. Kühne, B. Antz, K. Roth, and U. Wollschläger (2011), Observation of volumetric water content and reflector depth with multichannel ground-penetrating radar in an artificial sand volume, in *Proceedings of 6th International Workshop on Advanced Ground Penetrating Radar (IWAGPR)*, 2011, pp. 1–5, doi: [10.1109/IWAGPR.2011.5963910](https://doi.org/10.1109/IWAGPR.2011.5963910).

- Buchner, J. S., U. Wollschläger, and K. Roth (2012), Inverting surface GPR data using FDTD simulation and automatic detection of reflections to estimate subsurface water content and geometry, *Geophysics*, *77*(4), H45–H55, doi: [10.1190/geo2011-0467.1](https://doi.org/10.1190/geo2011-0467.1).
- Buchner, R., J. Barthel, and J. Stauber (1999), The dielectric relaxation of water between 0 °C and 35 °C, *Chemical Physics Letters*, *306*, 57–63, doi: [10.1016/S0009-2614\(99\)00455-8](https://doi.org/10.1016/S0009-2614(99)00455-8).
- Busch, S., J. van der Kruk, J. Bikowski, and H. Vereecken (2011), Combined effective wavelet estimation and full-waveform inversion of GPR data, in *Proceedings of 6th International Workshop on Advanced Ground Penetrating Radar (IWAGPR)*, 2011, pp. 1–5, doi: [10.1109/IWAGPR.2011.5963885](https://doi.org/10.1109/IWAGPR.2011.5963885).
- Carsel, R. F., and R. S. Parrish (1988), Developing joint probability distributions of soil water retention characteristics, *Water Resources Research*, *24*(5), 755–769, doi: [10.1029/WR024i005p00755](https://doi.org/10.1029/WR024i005p00755).
- Cheng, G., and T. Wu (2007), Responses of permafrost to climate change and their environmental significance, Qinghai-Tibet Plateau, *Journal of Geophysical Research*, *112*, F02S03, doi: [10.1029/2006JF000631](https://doi.org/10.1029/2006JF000631).
- Christensen, T. R., T. Johansson, H. J. Åkerman, M. Mastepanov, N. Malmer, T. Friberg, P. Crill, and B. H. Svensson (2004), Thawing sub-arctic permafrost: Effects on vegetation and methane emissions, *Geophysical Research Letters*, *31*(4), LO4501, doi: [10.1029/2003GL018680](https://doi.org/10.1029/2003GL018680).
- Churkina, G., and S. W. Running (1998), Contrasting climatic controls on the estimated productivity of global terrestrial biomes, *Ecosystems*, *1*, 206–215, doi: [10.1007/s100219900016](https://doi.org/10.1007/s100219900016).
- Crossley, J. (1971), Dielectric relaxation and molecular structure in liquids, *Royal Institute of Chemistry, Reviews*, *4*, 69–96, doi: [10.1039/RR9710400069](https://doi.org/10.1039/RR9710400069).
- Dagenbach, A. (2012), Untersuchung der hydraulischen Bodeneigenschaften durch GPR: Analyse der Kapillarsaumreflexion durch numerische Simulationen, Diploma thesis, Heidelberg University.
- Dai, R., and C. T. Young (1997), Transient fields of a horizontal electric dipole on a multilayered dielectric medium, *IEEE Transactions on Antennas and Propagation*, *45*(6), 1023–1031, doi: [10.1109/8.585751](https://doi.org/10.1109/8.585751).
- Daniels, D. (Ed.) (2004), *Ground penetrating radar*, 2nd ed., The Institution of Electrical Engineers, London, United Kingdom.
- Diamanti, N., P. Annan, and D. Redman (2012), Quantifying GPR responses, in *Proceedings fo the 4th International Conference on Ground Penetrating Radar, June 4-8, Shanghai, China*.
- Ehlers, E., and T. Krafft (Eds.) (2001), *Understanding the Earth systems*, Springer, Berlin, Heidelberg.

- Ellefsen, K. J., A. T. Mazzella, R. J. Horton, and J. R. McKenna (2011), Phase and amplitude inversion of crosswell radar data, *Geophysics*, *76*(3), J1–J12, doi: [10.1190/1.3554412](https://doi.org/10.1190/1.3554412).
- Ernst, J. R., A. G. Green, H. Maurer, and K. Holliger (2007a), Application of a new 2D time-domain full-waveform inversion scheme to crosshole radar data, *Geophysics*, *72*, J53–J64, doi: [10.1190/1.2761848](https://doi.org/10.1190/1.2761848).
- Ernst, J. R., H. Maurer, A. G. Green, and K. Holliger (2007b), Full-waveform inversion of crosshole radar data based on 2-D finite-difference time-domain solutions of Maxwell’s equations, *IEEE Transactions on Geoscience and Remote Sensing*, *45*(9), 2807–2828, doi: [10.1109/TGRS.2007.901048](https://doi.org/10.1109/TGRS.2007.901048).
- Farjadpour, A., D. Roundy, A. Rodriguez, M. Ibanescu, P. Bermel, J. D. Joannopoulos, S. G. Johnson, and G. W. Burr (2006), Improving accuracy by subpixel smoothing in the finite-difference time-domain, *Optics letters*, *31*(20), 2972–2974, doi: [10.1364/OL.31.002972](https://doi.org/10.1364/OL.31.002972).
- Fezoui, L., S. Lanteri, S. Lohrengel, and S. Piperno (2005), Convergence and stability of a discontinuous galerkin time-domain method for the 3D heterogeneous Maxwell equations on unstructured meshes, *ESAIM: Mathematical Modelling and Numerical Analysis*, *39*(06), 1149–1176, doi: [10.1051/m2an:2005049](https://doi.org/10.1051/m2an:2005049).
- Fritsch, F. N., and R. E. Carlson (1980), Monotone piecewise cubic interpolation, *SIAM Journal on Numerical Analysis*, *17*(2), 238–246, doi: [10.1137/0717021](https://doi.org/10.1137/0717021).
- Gerhards, H. (2008), Ground penetrating radar as a quantitative tool with applications in soil hydrology, Ph.D. thesis, Heidelberg University.
- Gerhards, H., U. Wollschläger, Q. Yu, P. Schiwek, X. Pan, and K. Roth (2008), Continuous and simultaneous measurement of reflector depth and average soil-water content with multichannel ground-penetrating radar, *Geophysics*, *73*(4), J15–J23, doi: [10.1190/1.2943669](https://doi.org/10.1190/1.2943669).
- Giannopoulos, A. (2005), Modelling ground penetrating radar by GprMax, *Construction and Building Materials*, *19*(10), 755–762, doi: [10.1016/j.conbuildmat.2005.06.007](https://doi.org/10.1016/j.conbuildmat.2005.06.007).
- Giroux, B., E. Gloaguen, and M. Chouteau (2007), bh_{tomo} – a Matlab borehole georadar 2D tomography package, *Computers & Geosciences*, *33*(1), 126–137, doi: [10.1016/j.cageo.2006.05.014](https://doi.org/10.1016/j.cageo.2006.05.014).
- Giroux, B., A. Bouchedda, and M. Chouteau (2009), Assisted travelttime picking of crosshole GPR data, *Geophysics*, *74*(4), J35–48, doi: [10.1190/1.3141002](https://doi.org/10.1190/1.3141002).
- Göktürkler, G., and Çağlayan Balkaya (2010), Travelttime tomography of crosshole radar data without ray tracing, *Journal of Applied Geophysics*, *72*(4), 213–224, doi: [10.1016/j.jappgeo.2010.09.004](https://doi.org/10.1016/j.jappgeo.2010.09.004).

- Guéguen, Y., and V. Palciauskas (1994), *Introduction to the physics of rocks*, Princeton University Press, Princeton, NJ.
- Guitton, A., G. Ayeni, and E. Díaz (2012), Constrained full-waveform inversion by model reparameterization, *Geophysics*, *77*(2), R117–R127, doi: [10.1190/geo2011-0196.1](https://doi.org/10.1190/geo2011-0196.1).
- Heimovaara, T. J., A. G. Focke, W. Bouten, and J. M. Verstraten (1995), Assessing temporal variations in soil water composition with time domain reflectometry, *Soil Science Society of America Journal*, *59*(3), 689–698, doi: [10.2136/sssaj1995.03615995005900030009x](https://doi.org/10.2136/sssaj1995.03615995005900030009x).
- Hoekstra, P., and A. Delaney (1974), Dielectric properties of soils at UHF and microwave frequencies, *Journal of Geophysical Research*, *79*(11), 1699–1708, doi: [10.1029/JB079i011p01699](https://doi.org/10.1029/JB079i011p01699).
- Holliger, K., M. Musil, and H. R. Maurer (2001), Ray-based amplitude tomography for crosshole georadar data: a numerical assessment, *Journal of Applied Geophysics*, *47*, 285–298, doi: [10.1016/S0926-9851\(01\)00072-6](https://doi.org/10.1016/S0926-9851(01)00072-6).
- Irving, J. D., M. D. Knoll, and R. J. Knight (2007), Improving crosshole radar velocity tomograms: A new approach to incorporating high-angle traveltime data, *Geophysics*, *72*(4), J31–J41, doi: [10.1190/1.2742813](https://doi.org/10.1190/1.2742813).
- Jackson, J. D. (Ed.) (2006), *Klassische Elektrodynamik*, 4th ed., Walter de Gruyter, Berlin.
- Jin, J. (Ed.) (2002), *The finite element method in electromagnetics*, 2nd ed., Wiley, New York.
- Julian, B. R., and D. Gubbins (1977), Three-dimensional seismic ray tracing, *Journal of Geophysics*, *43*, 95–113.
- Kaatze, U. (1989), Complex permittivity of water as a function of frequency and temperature, *Journal of Chemical & Engineering Data*, *34*(4), 371–374, doi: [10.1021/je00058a001](https://doi.org/10.1021/je00058a001).
- Kabat, P., M. Claussen, P. A. Dirmeyer, J. H. C. Gash, L. Bravo de Guenni, M. Meybeck, R. Pielke, C. J. Vörösmarty, R. W. A. Hutjes, and S. Lütkeimer (Eds.) (2004), *Vegetation, water, humans and the climate*, Global change - the IGBP series, Springer, Berlin, Heidelberg.
- Kerr, Y. H., P. Waldteufel, J.-P. Wigneron, J. Martinuzzi, J. Font, and M. Berger (2001), Soil moisture retrieval from space: the soil moisture and ocean salinity (SMOS) mission, *IEEE Transactions on Geoscience and Remote Sensing*, *39*(8), 1729–1735, doi: [10.1109/36.942551](https://doi.org/10.1109/36.942551).
- Kiehl, J. T., and K. E. Trenberth (1997), Earth’s annual global mean energy budget, *Bulletin of the American Meteorological Society*, *78*(2), 197–208.

- Klotzsche, A., J. van der Kruk, G. A. Meles, J. Doetsch, H. Maurer, and N. Linde (2010), Full-waveform inversion of cross-hole ground-penetrating radar data to characterize a gravel aquifer close to the Thur River, Switzerland, *Near Surface Geophysics*, 8, 635–649, doi: [10.3997/1873-0604.2010054](https://doi.org/10.3997/1873-0604.2010054).
- Kramer, P. J., and J. S. Boyer (1995), *Water relations of plants and soils*, Academic Press, San Diego.
- Kühne, A. (2010), Experimentelle Untersuchung der zeitlichen Variabilität des Bodenwassergehalts mit GPR, Staatsexamensarbeit, Heidelberg University.
- Kuroda, S., M. Takeuchi, and H. Kim (2007), Full-waveform inversion algorithm for interpreting crosshole radar data: a theoretical approach, *Geosciences Journal*, 11, 211–217, doi: [10.1007/BF02913934](https://doi.org/10.1007/BF02913934).
- Lambot, S., E. C. Slob, I. van den Bosch, B. Stockbroeckx, B. Scheers, and M. Vanclooster (2004a), Estimating soil electric properties from monostatic ground-penetrating radar signal inversion in the frequency domain, *Water Resources Research*, 40(4), WO4205, doi: [10.1029/2003WR002095](https://doi.org/10.1029/2003WR002095).
- Lambot, S., M. Antoine, I. Van den Bosch, E. C. Slob, and M. Vanclooster (2004b), Electromagnetic inversion of GPR signals and subsequent hydrodynamic inversion to estimate effective vadose zone hydraulic properties, *Vadose Zone Journal*, 3(4), 1072–1081.
- Lampe, B., K. Holliger, and A. G. Green (2003), A finite-difference time-domain simulation tool for ground-penetrating radar antennas, *Geophysics*, 68(3), 971–987, doi: [10.1190/1.1581069](https://doi.org/10.1190/1.1581069).
- Lashof, D. A., and D. R. Ahuja (1990), Relative contributions of greenhouse gas emissions to global warming, *Nature*, 344(6266), 529–531, doi: [10.1038/344529a0](https://doi.org/10.1038/344529a0).
- Marquardt, D. W. (1963), An algorithm for least-squares estimation of nonlinear parameters, *SIAM Journal on Applied Mathematics*, 11(2), 431–441.
- Maurer, H., A. Curtis, and D. E. Boerner (2010), Recent advances in optimized geophysical survey design, *Geophysics*, 75(5), 75A177–75A194, doi: [10.1190/1.3484194](https://doi.org/10.1190/1.3484194).
- Meles, G. A., J. Van der Kruk, S. A. Greenhalgh, J. R. Ernst, H. Maurer, and A. G. Green (2010), A new vector waveform inversion algorithm for simultaneous updating of conductivity and permittivity parameters from combination crosshole/borehole-to-surface GPR data, *IEEE Transactions on Geoscience and Remote Sensing*, 48(9), 3391–3407, doi: [10.1109/TGRS.2010.2046670](https://doi.org/10.1109/TGRS.2010.2046670).
- Millard, S. G., A. Shaari, and J. H. Bungey (2002), Field pattern characteristics of GPR antennas, *NDT & E International*, 35(7), 473–482, doi: [10.1016/S0963-8695\(02\)00023-3](https://doi.org/10.1016/S0963-8695(02)00023-3).

- Mualem, Y. (1976), A new model for predicting the hydraulic conductivity of unsaturated porous media, *Water Resources Research*, 12(3), 513–522, doi: [10.1029/WR012i003p00513](https://doi.org/10.1029/WR012i003p00513).
- Nakanishi, I., and K. Yamaguchi (1986), A numerical experiment on nonlinear image reconstruction from first-arrival times for two-dimensional island arc structures, *Journal of Physics of the Earth*, 34(2), 195–201, doi: [10.4294/jpe1952.34.195](https://doi.org/10.4294/jpe1952.34.195).
- Nussberger, M. (2005), Soil moisture determination with TDR: single-rod probes and profile reconstruction algorithms, Ph.D. thesis, ETH Zurich, doi: [10.3929/ethz-a-004948734](https://doi.org/10.3929/ethz-a-004948734).
- Or, D., and J. M. Wraith (1999), Temperature effects on soil bulk dielectric permittivity measured by time domain reflectometry: A physical model, *Water Resources Research*, 35(2), 371–383, doi: [10.1029/1998WR900008](https://doi.org/10.1029/1998WR900008).
- Oskooi, A. F., C. Kottke, and S. G. Johnson (2009), Accurate finite-difference time-domain simulation of anisotropic media by subpixel smoothing, *Optics Letters*, 34(18), 2778–2780, doi: [10.1364/OL.34.002778](https://doi.org/10.1364/OL.34.002778).
- Oskooi, A. F., D. Roundy, M. Ibanescu, P. Bermel, J. D. Joannopoulos, and S. G. Johnson (2010), Meep: A flexible free-software package for electromagnetic simulations by the fdtd method, *Computer Physics Communications*, 181, 687–702, doi: [10.1016/j.cpc.2009.11.008](https://doi.org/10.1016/j.cpc.2009.11.008).
- Ott, H. (1942), Reflexion und Brechung von Kugelwellen; Effekte 2. Ordnung, *Annalen der Physik*, 433(6), 443–466, doi: [10.1002/andp.19424330605](https://doi.org/10.1002/andp.19424330605).
- Pan, X., J. Zhang, P. Huang, and K. Roth (2012), Estimating field-scale soil water dynamics at a heterogeneous site using multi-channel GPR, *Hydrology and Earth System Sciences Discussions*, 9(7), 8027–8062, doi: [10.5194/hessd-9-8027-2012](https://doi.org/10.5194/hessd-9-8027-2012).
- Peraldi, R., and A. Clement (1972), Digital processing of refraction data study of first arrivals, *Geophysical Prospecting*, 20(3), 529–548, doi: [10.1111/j.1365-2478.1972.tb00653.x](https://doi.org/10.1111/j.1365-2478.1972.tb00653.x).
- Piperno, S., M. Remaki, and L. Fezoui (2002), A nondiffusive finite volume scheme for the three-dimensional Maxwell’s equations on unstructured meshes, *SIAM Journal on Numerical Analysis*, 39(6), 2089–2108, doi: [10.1137/S0036142901387683](https://doi.org/10.1137/S0036142901387683).
- Postel, S. L., G. C. Daily, and P. R. Ehrlich (1996), Human appropriation of renewable fresh water, *Science*, 271(5250), 785–788, doi: [10.1126/science.271.5250.785](https://doi.org/10.1126/science.271.5250.785).
- Press, W. H., S. A. Teukolsky, W. T. Vetterling, and B. P. Flannery (Eds.) (1992), *Numerical recipes in C*, 2nd ed., Cambridge University Press, Cambridge.
- Rawlinson, N., and M. Sambridge (2004), Wave front evolution in strongly heterogeneous layered media using the fast marching method, *Geophysical Journal International*, 156(3), 631–647, doi: [10.1111/j.1365-246X.2004.02153.x](https://doi.org/10.1111/j.1365-246X.2004.02153.x).

- Robinson, D. A., S. B. Jones, J. M. Wraith, D. Or, and S. P. Friedman (2003), A review of advances in dielectric and electrical conductivity measurement in soils using time domain reflectometry, *Vadose Zone Journal*, 2(4), 444–475.
- Robinson, D. A., C. S. Campbell, J. W. Hopmans, B. K. Hornbuckle, S. B. Jones, R. Knight, F. Ogden, J. Selker, and O. Wendroth (2008a), Soil moisture measurement for ecological and hydrological watershed-scale observatories: A review, *Vadose Zone Journal*, 7(1), 358–389, doi: [10.2136/vzj2007.0143](https://doi.org/10.2136/vzj2007.0143).
- Robinson, D. A., A. Binley, N. Crook, F. D. Day-Lewis, T. P. A. Ferre, V. J. S. Grauch, R. Knight, M. Knoll, V. Lakshmi, R. Miller, J. Nyquist, L. Pellerin, K. Singha, and L. Slater (2008b), Advancing process-based watershed hydrological research using near-surface geophysics: a vision for, and review of, electrical and magnetic geophysical methods, *Hydrological Processes*, 22(18), 3604–3635, doi: [10.1002/hyp.6963](https://doi.org/10.1002/hyp.6963).
- Rodríguez-Iturbe, I., and A. Porporato (2004), *Ecohydrology of water-controlled ecosystems: soil moisture and plant dynamics*, Cambridge Univ Press.
- Roth, K. (2011), *Soil physics, lecture notes*, Institute of Environmental Physics, Heidelberg University, v.2.0.
- Roth, K., R. Schulin, H. Flühler, and W. Attinger (1990), Calibration of time domain reflectometry for water content measurement using a composite dielectric approach, *Water Resources Research*, 26(10), 2267–2273, doi: [10.1029/WR026i010p02267](https://doi.org/10.1029/WR026i010p02267).
- Roth, K., W. A. Jury, H. Flühler, and W. Attinger (1991), Transport of chloride through an unsaturated field soil, *Water Resources Research*, 27(10), 2533–2541, doi: [10.1029/91WR01771](https://doi.org/10.1029/91WR01771).
- Rubin, Y., and S. S. Hubbard (Eds.) (2005), *Hydrogeophysics*, Springer, Dordrecht.
- Schaub, G., and T. Turek (2011), *Energy flows, material cycles and global development*, 1st ed., Springer, Berlin, Heidelberg.
- Schellnhuber, H.-J., and V. Wenzel (Eds.) (1998), *Earth system analysis*, Springer, Berlin, Heidelberg.
- Schneider, S. (2007), GPR Mehrkanalmessungen zur Bestimmung der Dynamik des Bodenwassergehaltes, Staatsexamensarbeit, Heidelberg University.
- Sendur, K., and W. Challener (2003), Near-field radiation of bow-tie antennas and apertures at optical frequencies, *Journal of Microscopy*, 210(3), 279–283, doi: [10.1046/j.1365-2818.2003.01145.x](https://doi.org/10.1046/j.1365-2818.2003.01145.x).
- Sethian, J. A. (1996), A fast marching level set method for monotonically advancing fronts, *Proceedings of the National Academy of Sciences*, 93(4), 1591–1595.
- Slob, E., M. Sato, and G. Olhoeft (2010), Surface and borehole ground-penetrating-radar developments, *Geophysics*, 75(5), 75A103–75A120, doi: [10.1190/1.3480619](https://doi.org/10.1190/1.3480619).

- Sommerfeld, A. (1909), Über die Ausbreitung der Wellen in der drahtlosen Telegraphie, *Annalen der Physik*, 333(4), 665–736, doi: [10.1002/andp.19093330402](https://doi.org/10.1002/andp.19093330402).
- Streich, R., and J. van der Kruk (2007), Accurate imaging of multicomponent GPR data based on exact radiation patterns, *IEEE Transactions on Geoscience and Remote Sensing*, 45(1), 93–103, doi: [10.1109/TGRS.2006.883459](https://doi.org/10.1109/TGRS.2006.883459).
- Taflove, A., and S. C. Hagness (Eds.) (2000), *Computational electrodynamics: The finite-difference time-domain method*, 2nd ed., Artech House, Norwood, MA.
- Tarantola, A. (1984), Inversion of seismic reflection data in the acoustic approximation, *Geophysics*, 49(8), 1259–1266, doi: [10.1190/1.1441754](https://doi.org/10.1190/1.1441754).
- Tinga, W. R., W. A. G. Voss, and D. F. Blossey (1973), Generalized approach to multiphase dielectric mixture theory, *Journal of Applied Physics*, 44(9), 3897–3902, doi: [10.1063/1.1662868](https://doi.org/10.1063/1.1662868).
- Topp, G. C., J. L. Davis, and A. P. Annan (1980), Electromagnetic determination of soil water content: Measurements in coaxial transmission lines, *Water Resources Research*, 16(3), 574–582, doi: [10.1029/WR016i003p00574](https://doi.org/10.1029/WR016i003p00574).
- Tronicke, J., K. Holliger, W. Barrash, and M. D. Knoll (2004), Multivariate analysis of cross-hole georadar velocity and attenuation tomograms for aquifer zonation, *Water Resources Research*, 40(1), W01,519, doi: [10.1029/2003WR002031](https://doi.org/10.1029/2003WR002031).
- Turin, G. (1960), An introduction to matched filters, *IRE Transactions on Information Theory*, 6(3), 311–329, doi: [10.1109/TIT.1960.1057571](https://doi.org/10.1109/TIT.1960.1057571).
- van der Kruk, J., R. Streich, and A. G. Green (2006), Properties of surface waveguides derived from separate and joint inversion of dispersive TE and TM GPR data, *Geophysics*, 71(1), K19–K29, doi: [10.1190/1.2168011](https://doi.org/10.1190/1.2168011).
- van Genuchten, M. T. (1980), A closed form equation for predicting the hydraulic conductivity of unsaturated soils, *Soil Science Society of America Journal*, 44(5), 892–898, doi: [10.2136/sssaj1980.03615995004400050002x](https://doi.org/10.2136/sssaj1980.03615995004400050002x).
- Vereecken, H., J. A. Huisman, H. Boga, J. Vanderborght, J. A. Vrugt, and J. W. Hopmans (2008), On the value of soil moisture measurements in vadose zone hydrology: A review, *Water Resources Research*, 44(8), 1–21, doi: [10.1029/2008WR006829](https://doi.org/10.1029/2008WR006829).
- Vidale, J. (1988), Finite-difference calculation of travel times, *Bulletin of the Seismological Society of America*, 78(6), 2062–2076.
- Vinje, V., E. Iversen, and H. Gjøystdal (1993), Traveltime and amplitude estimation using wavefront construction, *Geophysics*, 58(8), 1157–1166, doi: [10.1190/1.1443499](https://doi.org/10.1190/1.1443499).
- Virieux, J., and S. Operto (2009), An overview of full-waveform inversion in exploration geophysics, *Geophysics*, 74(6), WCC1–WCC26, doi: [10.1190/1.3238367](https://doi.org/10.1190/1.3238367).

- Šimůnek, J., M. Šejna, H. Saito, M. Sakai, and M. T. van Genuchten (2009), *The HYDRUS-1D software package for simulating the one-dimensional movement of water, heat, and multiple solutes in variably-saturated media – version 4.08*, Department of Environmental Sciences, University of California Riverside.
- Warren, C., and A. Giannopoulos (2012), Investigation of the directivity of a commercial ground-penetrating radar antenna using a finite-difference time-domain antenna model, in *Proceedings fo the 4th International Conference on Ground Penetrating Radar, June 4-8, Shanghai, China*.
- Weast, R. C. (Ed.) (1973), *Handbook of chemistry and physics*, 54th ed., Chemical Rubber Co., Cleveland, Ohio.
- Weyl, H. (1919), Ausbreitung elektromagnetischer Wellen über einem ebenen Leiter, *Annalen der Physik*, 365(21), 481–500, doi: [10.1002/andp.19193652104](https://doi.org/10.1002/andp.19193652104).
- Wright, D. H. (1990), Human impacts on energy flow through natural ecosystems, and implications for species endangerment, *Ambio*, 19(4), 189–194.
- Yaghjian, A. (1986), An overview of near-field antenna measurements, *IEEE Transactions on Antennas and Propagation*, 34(1), 30–45, doi: [10.1109/TAP.1986.1143727](https://doi.org/10.1109/TAP.1986.1143727).
- Yee, K. S. (1966), Numerical solution of initial boundary value problems involving Maxwell’s equations in isotropic media, *IEEE Transactions on Antennas and Propagation*, 14(3), 302–307, doi: [10.1109/TAP.1966.1138693](https://doi.org/10.1109/TAP.1966.1138693).
- Yilmaz, O. (Ed.) (2001), *Seismic data analysis*, Society of Exploration Geophysicists, Tulsa, Oklahoma.
- Zhou, B., and P. K. Fullagar (2001), Delineation of sulphide ore-zones by borehole radar tomography at Hellyer Mine, Australia, *Journal of Applied Geophysics*, 47, 261–269, doi: [10.1016/S0926-9851\(01\)00070-2](https://doi.org/10.1016/S0926-9851(01)00070-2).

Danksagung

Herzlicher Dank sei an dieser Stelle erbracht an:

Meine liebste Rike für ihre mehr als selbstverständliche Unterstützung und unser gemeinsames Leben.

Emilia, die mein Leben soviel schöner macht.

Meine Familie, die mir Halt und Kraft gibt.

Alle meine Freunde dafür das sie es gibt.

Christian, reicher Quell an Inspiration, der sich leider entschied viel zu früh zu gehen.

Kurt für seine Kreativität und Ideen, das Vertrauen in mich, die gute Zusammenarbeit und die wunderbaren Diskussionen weit über den Tellerrand hinaus.

Ute für die Betreuung und die viele Zeit die Sie sich genommen hat.

Peter der sich bereit erklärt hat die Arbeit zu begutachten.

Felix, Ute, Patrick und Andreas für das Gegenlesen.

Pan, Alex, Benny, Stefan und Holger für die Messung der Daten welche in dieser Arbeit Verwendung gefunden haben.

Olaf für die Ausgangsversion des Levenberg-Marquardt.

Angelika, für ihre stetigen Einsatz und insbesondere für ihre brillante Idee ein Silo für die ASSESS-GPR Site zu verwenden.

Die vielen fleißigen Hände die beim Bau von ASSESS-GPR mitgewirkt haben und die Site in Stand halten.

Patrick und Steffen, für viele Jahre gute Gesellschaft im Büro.

Alle Mitglieder der AG Bodenphysik und des Instituts für Umweltphysik für die lebendige Atmosphäre.

Die Deutsche Forschungsgemeinschaft (DFG) für die finanzielle Unterstützung.

Die vielen Kollegen in aller Welt die sich der Sache der Wissenschaft verschrieben haben.

“Modeling, however, never aims at precision but rather at a description of the ‘relevant’ features, where relevance relates to different objectives whatever we believe is important to us.”

Hans-Peter Dürr in [Schellnhuber and Wenzel \[1998\]](#)

